

Surface Deformation Analysis of Dense GPS Networks Based on Intrinsic Geometry Deterministic and Stochastic Aspects

A thesis accepted by the Faculty of Aerospace Engineering and Geodesy of the Universität Stuttgart in partial fulfilment of the requirements for the degree of Doctor of Engineering Sciences (Dr.-Ing.)

by

Khosro Moghtasad-Azar

born in Zanjan, Iran

main referee: Prof. Dr.- Ing. habil. Dr. tech. h. c. mult. Dr.-Ing. E.h. mult. Erik W. Grafarend

co-referee: Prof. Dr.-Ing. Nico Sneeuw

co-referee: Prof. Dr.-Ing. Dr. h. c. Bernhard Heck

Date of defence : 5.11.2007

Institute of Geodesy
Universität Stuttgart

2007

Abstract

The first step in this study is to review the properties of surface which are inherent to the surface and can be described without referring to the embedding space. In other words, it is a method of differential geometry. The methods of moving frames which allows deformation of surface could be described by its own rights as a more reliable estimate of surface deformation measures. The method takes advantage of the simplicity of the 2D surface \mathbb{M}^2 versus the 3D Euclidean spaces \mathbb{E}^3 without losing or neglecting information about the third dimension in the results. Based on this method, deformation can be described by using tangent vectors and the unit normal basis vector (attached to the bodies before and after deformation). However, basis vectors of the deformed configuration will need to complete information of intrinsic properties of the deformed surface.

Through this method, regularized Earth's surface is considered as a graded 2D surface, namely a curved surface, embedded in a Euclidean space \mathbb{E}^3 . Thus, deformation of the surface can be completely specified by the change of the metric and curvature tensors, namely strain tensor and tensor of change of curvature (TCC). The curvature tensor, however, is responsible for the detection of vertical displacements on the surface.

The next step of this study is to concentrate the local basis vectors of the deformed surface which can be formulated in terms of the local basis vectors of undeformed surface and curvilinear components of displacement vector. This will provide a representation of the intrinsic geometry of the deformed surface with deriving information about the displacement field. The new formulation of base vectors (for the deformed body) produces meaningful numerical results for the TCC and its associated invariants (mean and Gaussian curvatures). They can propose a shape-classification of the deformed surface based upon signs of mean and Gaussian curvatures which are new tools for studying the Earth's deformation. To enhance our understanding of the capabilities of the proposed method in defining new basis vectors (for deformed body), we present two examples, one with a simulated data set and the other with a real data set. However, through a real data set we demonstrated a comparison between the proposed method with the plane strain model (2D classical method).

Dealing with eigenspace components e.g., principal components and principal directions of 2D symmetric random tensors of second order is of central importance in this study. In the third step of this research, we introduce an eigenspace analysis or a principal component analysis of strain tensor and TCC. However, due to the intricate relations between elements of tensors on one side and eigenspace components on other side, we will convert these relations to simple equations, by simultaneous diagonalization. This will provide simple synthesis equations of eigenspace components (e.g., applicable in stochastic aspects).

The last part of this research is devoted to stochastic aspects of deformation analysis. In the presence of errors in measuring a random displacement field (under the normal distribution assumption of displacement field), stochastic behaviors of eigenspace components of strain tensor and TCC are discussed. It is performed by a propagation of errors from the displacement vector into elements of deformation tensors (strain and TCC). However, due to the intricacy of the relations between tensor components (strain or TCC) and their eigenspace components, we proceeded via simultaneous diagonalization. This part is followed by a linearization of the nonlinear multivariate Gauss - Markov model, which links the elements of transformed tensors (obtained by simultaneous diagonalization)

with the eigenspace components. Then, we set up an observation model based on a linearized model under a sampling of eigenspace synthesis.

Furthermore, we establish linearized observation equations for n samples of independent random vectors from transformed tensor elements (under the normal distribution assumption), each with an individual covariance matrix. This will provide us with the second-order statistics of the eigenspace components. Then we estimate the covariance components between transformed tensor elements by Helmert estimator, based on prior variance information. To enhance conceptual understanding of stochastic aspects of deformation analysis, the method is applied to a real data set of dense GPS network of Cascadia Subduction Zone(CSZ). Comparing the results showed that, in general, after estimating the covariance matrix of observations (transformed tensors via simultaneous diagonalization), variances of eigenspace components become smaller. However, in some areas this did not occur, which can be related to an incorrect description of initial accuracies, either too optimistic or too pessimistic.

Zusammenfassung

Der erste Schritt dieser Studie besteht darin, einen Überblick über die inhärenten Eigenschaften einer Oberfläche zu geben, die ohne Betrachtung des umliegenden Raumes beschrieben werden können. In anderen Worten, es ist eine Methode der Differenzial-Geometrie. Die Methode der beweglichen Rahmen, welche die Deformation einer Oberfläche erlaubt, kann bedingt durch eigene Regeln als eine zuverlässigere Art der Schätzung von Deformationsmaßen einer Oberfläche angesehen werden. Die Methode nutzt die Vorteile der Einfachheit der 2D-Oberfläche M^2 gegenüber dem 3D-Euklidischen Raumes E^3 , ohne Information über die dritte Dimension in den Ergebnissen zu verlieren oder zu vernachlässigen. Auf dieser Methode basierend kann die Deformation mit Tangenten-Vektoren und Einheitsnormalenvektoren beschrieben werden, welche vor und nach der Deformation am Körper angebracht werden. Es werden allerdings für die Basis-Vektoren der deformierten Konfiguration die Erkenntnisse über die inneren Eigenschaften der deformierten Oberfläche benötigt.

Unter Verwendung dieser Methode wird die regularisierte Erdoberfläche als zwei - dimensionale, glatte Oberfläche, genauer gesagt als gekrümmte Oberfläche, betrachtet, welche im Euklidischen Raum E^3 liegt. Daher kann die Oberflächendeformation komplett durch die Veränderung der Metriktensoren und der Krümmungstensoren, speziell des Verzerrungstensors und des Tensors der Krümmungsänderung, beschrieben werden. Der Krümmungstensor ist jedoch verantwortlich für die Ermittlung von vertikalen Verschiebungen auf der Oberfläche.

Der nächste Schritt der Studie besteht darin, die lokalen Basisvektoren der deformierten Oberfläche auszurichten, welche unter Einbeziehung des lokalen Basisvektors der undeformierten Oberfläche und der krummlinigen Komponenten des Verschiebungsvektors formuliert werden können. Dies wird eine Vorstellung der inneren Geometrie der deformierten Oberfläche und zusätzliche Informationen über ihr Verschiebungsfeld geben.

Die neue Formulierung der Basisvektoren (des deformierten Körpers) führt zu signifikanten numerischen Ergebnissen für den Tensor der Krümmungsänderung und seine Invarianten (mittlere und Gauss'sche Krümmungen). Eine Klassifizierung der Form der deformierten Oberfläche ist beruhend auf den Vorzeichen der mittleren und Gauss'schen Krümmungen möglich, was somit ein neues Instrument für die Untersuchung der Erd-Deformation darstellt. Für die Vertiefung unserer Kenntnisse über die Möglichkeiten dieser Methode, neue Basisvektoren für einen deformierten Körper zu finden, geben wir zwei Beispiele an, eines mit simulierten Daten und das andere mit echten Daten. Durch das Beispiel mit echten Daten können wir zusätzlich unsere Methode mit dem ebenen Verzerrungsmodell (klassische 2D-Methode) vergleichen.

Die Behandlung von Eigenraum - Komponenten wie beispielsweise den Hauptkomponenten und -richtungen der symmetrischen 2D - Zufallstensoren zweiter Ordnung ist in dieser Studie von zentraler Bedeutung . Im dritten Teil dieser Studie führen wir eine Eigenraum - Analyse (oder : Analyse der Hauptkomponenten) des Verzerrungstensors und des Tensors der Krümmungsänderung ein. Aufgrund der komplexen Beziehungen zwischen den Elementen des Tensors auf der einen und den Eigenraum-Komponenten auf der anderen Seite, werden wir diese komplexen Verhältnisse mittels simultaner Diagonalisierung in einfachen Gleichungen darstellen. Dies liefert einfache Synthese - Gleichungen für die Eigenraum-Komponenten, welche beispielsweise für stochastische Aspekte verwendbar sind.

Der letzte Teil dieser Studie ist den stochastischen Aspekten der Deformations-Analyse gewidmet. In der Gegenwart von Messfehlern bei der Erfassung von zufälligen Verschiebungsfeldern (unter Annahme eines normalverteilten Verschiebungsfeldes) wird das stochastische Verhalten der Eigenraum - Komponenten des Verzerrungstensors und des Tensors der Krümmungsänderung diskutiert. Dies wird durch eine Fehlerfortpflanzung von dem Verschiebungsvektor zu den Elementen des Deformationstensors (Verzerrungstensor und Tensor der Krümmungsänderung) erreicht. Aufgrund der komplexen Verhältnisse zwischen Tensorkomponenten (Verzerrungstensor und Tensor der Krümmungsänderung) und ihren Eigenraum - Komponenten verwenden wir hierfür simultane Diagonalisierung. Diesem Teil folgt eine Linearisierung des nichtlinearen multivariaten Gauss - Markov Modells, welches die Elemente der durch simultane Diagonalisierung transformierten mit den Eigenraum - Komponenten verbindet. Anschliessend stellen wir ein Beobachtungsmodell auf, welches auf einem linearisierten Modell der Eigenraum-Synthese basiert.

Desweiteren erstellen wir linearisierte Beobachtungsgleichungen für n Stichproben von unabhängigen Zufallsvektoren aus den transformierten Tensorelementen (unter Annahme der Normalverteilung), von denen jeder eine eigene Varianzmatrix besitzt. Dadurch erhalten wir die Statistiken zweiter Ordnung der Eigenraum-Komponenten. Anschliessend bestimmen wir die Kovarianzkomponenten zwischen den transformierten Tensorelementen mittels eines Helmert - Schätzers basierend auf a-priori Varianzinformationen. Um die konzeptuelle Kenntnis der stochastischen Aspekte der Deformationsanalyse zu verbessern, wird die Methode für reale Daten eines engmaschigen GPS Netzes der Cascadia Subduktionszone (CSZ) angewandt. Ein Vergleich der Ergebnisse zeigt, dass im Allgemeinen nach der Schätzung der Kovarianzmatrix der Beobachtungen (mittels simultaner Diagonalisierung transformierte Tensoren) die Varianzen der Eigenraumkomponenten kleiner werden. In manchen Regionen trat dies jedoch nicht ein, was an einer inkorrekten Beschreibung der anfänglichen Genauigkeiten liegen kann, die entweder zu pessimistisch oder zu optimistisch waren.

Acknowledgements

I would like to express my sincere gratitude to my supervisor, Prof. Dr.-Ing. habil. Erik W. Grafarend, for introducing this fascinating topic to me and whose tireless efforts and patience as my supervisor greatly contributed towards the completion and success of this study at the Institute of Geodesy - Faculty of Aerospace Engineering and Geodesy, University of Stuttgart.

My hearty thanks also go to Prof. Dr.Ing. Sneeuw and Prof. Dr.-Ing. Heck for reviewing the work with great care and providing many helpful comments and suggestions that further improved this dissertation.

Special mention must also be made of my colleagues Dr. J. Engels and Dr. F.W. Krumm, whose scientific supports in continuum mechanics and theory of map projection provided me with the theoretical basis for further works described herein.

I am grateful to the members of the Department of Geodesy- Faculty of Aerospace Engineering and Geodesy, University of Stuttgart, for each of them contributed in one way or another towards the success of my research work.

I wish to acknowledge gratefully the financial support from the Ministry of Culture and Higher Education of Iran for sponsoring this Ph.D. study.

Last, but not least, I wish to acknowledge the patience of my wife Zhaleh Safarpour and my son Ataeollah Moghtasad-Azar for all their unsparing support and understanding.

Contents

Abstract	i
Zusammenfassung	iii
1 Introduction	1
1.1 Background	1
1.2 Objectives of Thesis	2
1.3 Outline of Thesis	2
2 Deformation	4
2.1 Concepts	5
2.2 Comparison of the First Fundamental Forms	6
2.3 Deformation Gradients	7
2.4 Strain Tensor: deformation tensor of first kind	9
2.4.1 An Analytical Example	11
2.4.2 Eigenspace Analysis, Strain Tensor	14
2.5 Comparison of Second Fundamental Forms	20
2.5.1 Mean and Gaussian Curvatures	22
2.6 Tensor of Changes of Curvature (TCC): deformation tensor of second kind	24
2.6.1 An Analytical Example	25
2.6.2 Basis Vectors on Deformed Surface in Terms of Lagrangian Coordinates	27
2.6.3 Eigenspace Analysis, TCC	27
2.7 Changes in Mean and Gaussian Curvatures	29
2.8 Numerical Examples	29
2.8.1 Application Using Simulated Data	30
2.8.2 Application Using Real Data	33
3 Stochastic Aspects	49
3.1 Error Propagations for Strain Components	49
3.2 Error Propagations for TCC Components	51
3.3 Error Propagations for Eigenspace Components	53
3.3.1 Setup of Linear Observation Model	55
3.4 Variance-Covariance Estimation of Helmert type	60
3.5 A Numerical Example	62
3.5.1 Tectonic Setting of the Cascadia Subduction Zone	62
3.5.2 GPS Arrays	64

3.5.3	Data Processing Strategy	65
3.5.4	Results	68
4	Concluding Remarks	77
4.1	Discussion	77
4.2	Outlook	78
	List of Abbreviations	84
	List of Symbols	86
	Appendices	89
A	Partial Derivatives of Local Basis Vectors	89
B	2D Finite Element Method	91
	CURRICULUM VITAE	92

List of Figures

2.1	Deformation of surface \mathbb{M}_l^2 into another surface \mathbb{M}_r^2	6
2.2	Schematic description of the polar decomposition of the deformation matrix $\mathbf{J} = \mathbf{R}\mathbf{U} = \mathbf{V}\mathbf{R}$	9
2.3	Displacement vector.	10
2.4	Geometrical representation of simultaneous diagonalization of matrices $\{\mathbf{E}_l, \mathbf{A}_l\}$	19
2.5	Illustrates the orientation of major eigenvector of left Euler-Lagrange strain tensor on surface \mathbb{M}_l^2 by Ψ , and on plane by Θ	19
2.6	Albers conical equal area on a reference ellipsoid with coastlines and Tissot ellipses of distortions.	20
2.7	Surface with normal planes in directions of principal curvatures.	22
2.8	Eight basic visible-invariant surface types.	23
2.9	Difference of unit normal vectors \mathbf{w} which is illustrated by dashed line.	25
2.10	Rates of simulated vertical displacement field in units of m.yr^{-1}	30
2.11	Optimal Delaunay triangulation, dilatation, change of mean curvature, change of Gaussian curvature over the test area.	32
2.12	Southern California Fault summarizes.	34
2.13	Southern California seismic events with $M_w \geq 3$	34
2.14	Sites of SOPAC network by individual solutions between 2001 and 2005.	35
2.15	Horizontal velocity field in units of mm.yr^{-1} across Southern California.	36
2.16	Vertical velocity field in units of mm.yr^{-1} across Southern California.	37
2.17	Delaunay triangulation of permanent GPS network across Southern California.	38
2.18	Maximum geodetic surface strain-rate and maximum shear strain-rate in units of yr^{-1} over Southern California	40
2.19	Surface dilation in units of yr^{-1} across Southern California.	41
2.20	Rotation and its absolute magnitude around the normal in units of rad.yr^{-1} over Southern California	42
2.21	Difference and sum of the eigenvalues of TCC in units of yr^{-1} over Southern California	44
2.22	Change of mean curvature in units of $\text{m}^{-1}.\text{yr}^{-1}$, change of Gaussian curvature in units of $\text{m}^{-2}.\text{yr}^{-1}$ and patterns of GPS height components (in ITRF2000) in units of mm.yr^{-1} over Southern California.	45
2.23	Principal quantities of strain tensor derived by 2D classical method : Maximum shear strain rate, dilatation and rotation over Southern California.	48
3.1	The α confidence intervals for the eigenvalues Λ_1, Λ_2 and the eigen-direction Θ	59
3.2	Tectonic map of the Cascadia Subduction Zone.	63
3.3	Pacific Northwest seismic events with $M_w \geq 3$ from the Northern California Earthquake Catalog Search (1969 to 2006) which are scaled by magnitude.	64

3.4	Pacific Northwest Geodetic Array (PANGA) which have nearly daily solutions through the period of 1996-2006.	65
3.5	GPS-determined horizontal velocity field by Pacific Northwest Geodetic Array (PANGA). . .	66
3.6	GPS-determined vertical velocity field by Pacific Northwest Geodetic Array (PANGA). . . .	67
3.7	Optimal Delaunay triangulations over the Pacific Northwest Geodetic Array (PANGA).	68
3.8	Pattern of eigenspace components of the surface strain-rate tensor and their 95% confidence intervals, in unit of 10^{-7} yr $^{-1}$	69
3.9	Pattern of eigenspace components of the TCC and their 95% confidence intervals, in unit of 10^{-7} m $^{-1}$.yr $^{-1}$	70
3.10	Pattern of eigenspace components of the surface strain-rate tensor and their 95% confidence intervals, in unit of 10^{-7} yr $^{-1}$ based on estimated covariance matrix of transformed strain tensor (via simultaneous diagonalization)	73
3.11	Pattern of eigenspace components of the TCC and their 95% confidence intervals, in unit of 10^{-7} yr $^{-1}$ based on estimated covariance matrix of transformed strain tensor (via simultaneous diagonalization)	75

List of Tables

2.1	Various measures for deformation (based on FFF).	14
2.2	Shape classification based on the signs of mean and Gaussian curvatures.	23
2.3	Various measures for deformation (based on SFF).	29
3.1	Estimated eigenvalues and eigendirections of the strain tensor in 95% confidence intervals based on a-priori variance component information.	71
3.2	Estimated eigenvalues and eigendirections of TCC in 95% confidence intervals based on a-priori variance component information.	72
3.3	Estimated eigenvalues and eigendirections of strain tensor in 95% confidence intervals based on estimated covariance matrix of transformed strain tensor (via simultaneous diagonalization).	74
3.4	Estimated eigenvalues and eigendirections of TCC in 95% confidence intervals based on estimated covariance matrix of transformed TCC (via simultaneous diagonalization).	76

Chapter 1

Introduction

1.1 Background

Following the classical separation of established geodetic techniques, namely triangulation and trilateration versus leveling, the deformation of the Earth's surface has been separated into horizontal and vertical components and has been treated individually. The main reason for this conventional separate procedure is due to the horizontal and vertical networks in classical geodesy.

Later space geodesy, such as GPS, VLBI, SLR, and DORIS has changed the rules of the game of positioning essentially. Positions of network points, containing both horizontal and vertical components, could be determined with high precision, enough to be used as an accurate and reliable source of information in Earth deformation studies. The great number of studies of this type using displacement fields derived from repeated observations of space geodetic networks indicates what an important role the space geodetic techniques play in present and future states of geodynamics.

In this concept, we make use of continuous measurements over periods of several years for crustal deformation studies. If we do not have continuous measurements over periods of several years, the crustal deformation studies should be carried out under separation of horizontal and vertical components. The main reason of the separation is claimed to be the non-sufficient accuracy of the height component of point positioning.

Crustal motions and deformations are embedded in Euclidean space \mathbb{E}^3 . Therefore, the modeling of the problems connected with deformations in Euclidean space \mathbb{E}^3 by computing separately the 2D planar deformations and vertical motions cannot portray the real state of crustal deformations. Then, there have been attempts to derive 3D deformation from surface data by forming tetrahedrons and using the 3D finite element method where homogenous deformation is assumed within each tetrahedron, which is an extension of the similar 2D approach where triangles are formed [Dermanis and Grafarend, 1993]. However, 3D methods of Earth deformation analysis lose the simplicity of computations in 2D spaces.

These facts indicate the need for reevaluation of the theoretical foundations of the Earth deformation analysis methods. Regarding these disadvantages and difficulties as well as the fact that we have only surface geodetic measurements in our hands, it seems that a surface approach in the Earth's surface deformation analysis based on 3D displacement fields is an appropriate solution.

Applications of mathematical methods of surface deformation analysis can be seen in map pro-

jection studies. Interesting works have been investigated for the study of deformations induced when original figures on a sphere or an ellipsoid, as 2D Riemann manifolds, \mathbb{M}^2 , are mapped on a plane, as a Euclidean space \mathbb{E}^2 (see e.g., Chovitz [1979]; Hojovec et al. [1981]; Dermanis and Livieratos [1983]). The development of all formulae for the computation of internal and external deformation measures with Cartesian and ellipsoidal coordinates has been performed by Altiner [1996, 1999]. Furthermore, he developed a method of analytical surface deformation analysis of the Earth's crustal movements. Later, Voosoghi [2000] presented an analytical formulation and implementation of a method of Earth's surface deformation analysis referring to the *real surface of the Earth*. The Earth's surface is considered as a curved surface, embedded in Euclidean space \mathbb{E}^3 . For description of deformation tensors, he used tangent and normal basis vectors (attached to the bodies before and after deformation). However, for the construction of basis vectors on the deformed configuration we will need to complete information of intrinsic properties of deformed surface.

1.2 Objectives of Thesis

The surface deformation analysis, as described by Voosoghi [2000], is the basis for this study. Improvements that are addressed in this study are related to the:

Basis Vectors. The local basis vectors of deformed surface are formulated in terms of the local basis vectors of undeformed surface and curvilinear components of the displacement vector. This will provide a representation to intrinsic geometry of the deformed surface with deriving information about the displacement field.

Shape Classifications. The new formulation of base vectors (for deformed body) produces meaningful numerical results for the tensor of change of curvature and its associated invariants (mean and Gaussian curvatures). They can propose a shape-classification of deformed surface based upon signs of mean and Gaussian curvatures which are new tools for studying the Earth's deformation.

A comparison with plane strain. Through a real data set we demonstrate a comparison between proposed method with the plane strain model (2D classical method).

Eigenspace analysis. We introduce eigenspace analysis or principal component analysis of strain tensor and tensor of change of curvature (TCC). However, due to the intricate relations between elements of tensors on one side and eigenspace components on the other side, we will convert these relations to simple equations, by simultaneous diagonalization. This will provide simple synthesis equations of eigenspace components (e.g., applicable in stochastic aspects).

Stochastic Aspects In the presence of errors in measuring the random displacement field (under the normal distribution assumption of the displacement field), the stochastic behavior of eigenspace components of strain tensor and TCC is discussed. We divided the context into two parts : In the first, we considered independent random vectors of repeated transformed tensor measurements. In the second step we considered correlations between repeated measurements (transformed tensors) and we estimated a covariance matrix of measurements.

1.3 Outline of Thesis

This thesis is organized as follows :

Chapter 2 deals with deterministic aspects of deformation analysis. First, we reviewed differential geometry to describe object deformation, including comparison of the first fundamental forms, deformation gradients, Cauchy-Green deformation tensors and briefly account about polar decomposition and strain tensor. An analytical example will be given on the real surface of the Earth. Then we will discuss in eigenspace analysis, a comparison of the second fundamental forms, mean and Gaussian curvatures and TCC. In the final section of this chapter, we will represent two numerical examples : one with a simulated deformation model and one with the crustal deformation field (through the continuous GPS data).

Chapter 3 describes the stochastic aspects of deformation analysis. In this chapter the process of error propagations, in the presence of errors in measuring a random displacement field (under the normal distribution assumption of a displacement field) to components of strain tensor and TCC are discussed. This chapter also covers statistical inference of eigenspace components of deformation tensors based on random vectors of tensor measurements. The last section of this chapter is devoted to presenting a numerical example with the crustal deformation field (through the continuous GPS data) in Cascadia Subduction Zone (CSZ).

Chapter 4 reports the general results and conclusions, and gives recommendations for future research. Proof of the first-partial derivatives of basis vectors is given in Appendix A, and Appendix B describes briefly the 2D finite element approach.

To preserve the briefness in the symbols used, we shall denote the space coordinates with X^K ($K = 1, 2, 3$) and coordinates on the surface with Θ^Λ ($\Lambda = 1, 2$). We shall also observe the rule that lowercase Latin indices may take values 1, 2, 3 and the Greek indices values of 1, 2. In order to simplify the notation, partial derivatives are often represented by a comma (e.g., $\mathbf{u}_{,\Lambda} = \frac{\partial \mathbf{u}}{\partial \Theta^\Lambda}$). Also, the quantities associated with the undeformed body will be denoted by capital letters and those associated with deformed body will be denoted by lowercase letters.

Chapter 2

Deformation

This chapter is concerned with an exposition of the geometry of deformation. It may be considered as a discussion of differential geometry appropriate to deformable bodies. The main purpose is to connect the elements of a deformable body to their original locations and measures. To describe the positions of material points, we introduce, in section 2.1, two sets of curvilinear coordinate systems, one for the undeformed and one for the deformed body. These coordinate systems are characterized through their relations to any rectangular frame of reference. In this section, basis vectors essential to the representation of vectors are introduced.

In section 2.2, the first fundamental form (FFF) for both deformed and undeformed bodies is obtained. In this section, we also give a brief account of tensor notations. The concepts of the deformation gradients and deformation tensors of Cauchy and of Green are given in 2.3. Furthermore, in this section, the polar decomposition of a deformation gradient tensor is discussed briefly.

The strain tensor, as a deformation tensor of first kind, and the displacement vector are introduced in the subsequent section, followed by a curvilinear component of displacement vector and one analytical example in section 2.4. In this section we also give a detailed discussion of eigenspace analysis and strain invariants. Due to the intricate relations between elements of strain tensor on one side and eigenspace components on the other side, we will present a discussion on how to transform these relations into simple equations, by simultaneous diagonalization of strain tensor with associated metric tensor.

Comparing a second fundamental form (SFF) of deformed and undeformed bodies, likewise concepts of mean and Gaussian curvatures are given in section 2.5. Tensor of changes of curvature (TCC), as the deformation tensor of second kind is explained in section 2.6. This section is followed by giving an example and eigenspace analysis of TCC. Section 2.7 is devoted to the changes in mean and Gaussian curvatures, due to the deformation. In the final section we will present two numerical examples : one with a simulated deformation model and one with the crustal deformation field (through continuous GPS measurements).

Using the simulated deformation model we will explain step-by-step how to create an algorithm based on the proposed method for the analysis of deformation. Meanwhile, through a real data set we demonstrate a comparison between proposed method with the plane strain model (2D classical method).

2.1 Concepts

We suppose that a surface \mathbb{M}_l^2 , at certain time e.g. $t = 0$, occupies a certain region of the physical space. The position of a particle $M \in \mathbb{M}_l^2$ at this time can be described by a curvilinear coordinate system $\{\Theta^1, \Theta^2\}$ attached to the surface or by position vector \mathbf{X} measured from an origin O of the orthogonal fixed frame $\{\mathbf{J}_1, \mathbf{J}_2, \mathbf{J}_3 \mid O\}$ to M . In the same manner, we assume that after deformation the position of a particle on the deformed surface $m \in \mathbb{M}_r^2$ at time t is denoted by a new set of curvilinear coordinates $\{\theta^1, \theta^2\}$ on a deformed surface or by position vector \mathbf{x} which extends from the origin o of the new orthogonal fixed frame $\{\mathbf{j}_1, \mathbf{j}_2, \mathbf{j}_3 \mid o\}$ to m .

Following the conventions of literature in deformation analysis, we shall call coordinates which refer to undeformed surface *material* or *Lagrangian* coordinates and coordinates which refer to deformed surface *spatial* or *Eulerian* coordinates. However, in map projection conventions, coordinates of surface before deformation are so-called *left* coordinates, and coordinates of surface after deformation are so-called *right* coordinates.

Hence, the quantities associated with the undeformed body will be denoted by capital letters and those associated with deformed body will be denoted by lowercase letters. The motion of the surface can carry various material points through various spatial points. This is expressed by

$$\theta^\phi = \theta^\phi(\Theta^\Phi, t) \quad \text{vs.} \quad \Theta^\Phi = \Theta^\Phi(\theta^\phi, t) \quad (2.1)$$

Thus each point m on \mathbb{M}_r^2 at time t comes from a point M in \mathbb{M}_l^2 at time $t = 0$. We assume that the mappings (2.1) are single-valued and have continuous partial derivatives with respect to their arguments. Furthermore each member of (2.1) is the unique inverse of the order in a neighborhood of the material point M . A unique inverse of the first part of (2.1) exists, at least in a δ neighborhood of m , if and only if the determinant of the *Jacobian* matrix is not equal to zero, e.g.,

$$\det\left[\frac{\partial\theta^\phi}{\partial\Theta^\Phi}\right] := \det\begin{bmatrix} \frac{\partial\theta^1}{\partial\Theta^1} & \frac{\partial\theta^1}{\partial\Theta^2} \\ \frac{\partial\theta^2}{\partial\Theta^1} & \frac{\partial\theta^2}{\partial\Theta^2} \end{bmatrix} \neq 0 \quad |\theta^\phi - \Theta^\phi| < \delta$$

Equation of motion (2.1) shifts every region into region, every surface into surface and every curve into curve. Furthermore, it implies the *indestructibility of matter* as well as *impenetrability of matter*. No region of positive, finite volume is deformed into one of zero or infinite volume. Also, one portion of a matter never penetrates into another.

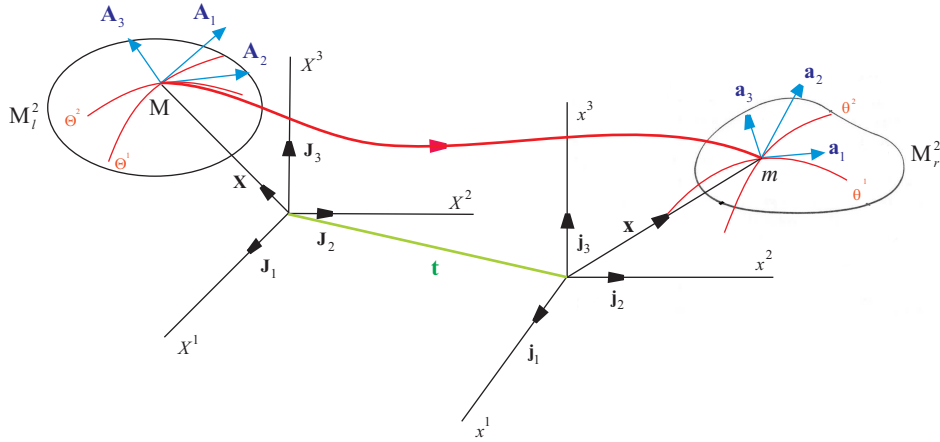
Following the Fig. 2.1, the position vector \mathbf{X} of a point M on surface \mathbb{M}_l^2 and position vector \mathbf{x} of a point m on deformed surface \mathbb{M}_r^2 , referred respectively to orthogonal fixed frames X^K and x^k , could be expressed by

$$\mathbf{X} = \mathbf{J}_K X^K(\Theta^1, \Theta^2) \quad \text{vs.} \quad \mathbf{x} = \mathbf{j}_k x^k(\theta^1, \theta^2)$$

where the summation convention over the repeated index K and k are applied. Here, the basis vectors of rectangular coordinate systems X^K and x^k are specified by \mathbf{J}^K and \mathbf{j}^k , respectively.

Tangent basis vectors $d\mathbf{X}$ in \mathbb{M}_l^2 and $d\mathbf{x}$ in \mathbb{M}_r^2 may be expressed as

$$d\mathbf{X} = \frac{\partial\mathbf{X}}{\partial\Theta^\Lambda} d\Theta^\Lambda = \mathbf{A}_\Lambda d\Theta^\Lambda \quad \text{vs.} \quad d\mathbf{x} = \frac{\partial\mathbf{x}}{\partial\theta^\lambda} d\theta^\lambda = \mathbf{a}_\lambda d\theta^\lambda \quad (2.2)$$

Figure 2.1: Deformation of surface \mathbb{M}_l^2 into another surface \mathbb{M}_r^2 .

where as

$$\mathbf{A}_\Lambda := \frac{\partial \mathbf{X}}{\partial \Theta^\Lambda} = \mathbf{J}_K \frac{\partial X^K}{\partial \Theta^\Lambda} \quad \text{vs.} \quad \mathbf{a}_\lambda := \frac{\partial \mathbf{x}}{\partial \theta^\lambda} = \mathbf{j}_k \frac{\partial x^k}{\partial \theta^\lambda} \quad (2.3)$$

are the tangent basis vectors to the coordinates $\{\Theta^1, \Theta^2\}$ and $\{\theta^1, \theta^2\}$ respectively.

The unit normal vectors, often simply called the normals, to \mathbb{M}_l^2 and \mathbb{M}_r^2 can be expressed with cross products of tangential basis vectors by

$$\mathbf{A}_3 = \frac{\mathbf{A}_1 \times \mathbf{A}_2}{\|\mathbf{A}_1 \times \mathbf{A}_2\|} \quad \text{vs.} \quad \mathbf{a}_3 = \frac{\mathbf{a}_1 \times \mathbf{a}_2}{\|\mathbf{a}_1 \times \mathbf{a}_2\|} \quad (2.4)$$

2.2 Comparison of the First Fundamental Forms

The first fundamental form (FFF), or squares of infinitesimal lengths, in \mathbb{M}_l^2 and \mathbb{M}_r^2 are respectively

$$I(\Theta^1, \Theta^2) := \langle d\mathbf{X}, d\mathbf{X} \rangle \quad \text{vs.} \quad I(\theta^1, \theta^2) := \langle d\mathbf{x}, d\mathbf{x} \rangle$$

where the use of (2.2) yields

$$I(\Theta^1, \Theta^2) = A_{\Lambda\Phi} d\Theta^\Lambda d\Theta^\Phi \quad \text{vs.} \quad I(\theta^1, \theta^2) = a_{\lambda\phi} d\theta^\lambda d\theta^\phi \quad (2.5)$$

which

$$A_{\Lambda\Phi} = \langle \mathbf{A}_\Lambda, \mathbf{A}_\Phi \rangle \quad \text{vs.} \quad a_{\lambda\phi} = \langle \mathbf{a}_\lambda, \mathbf{a}_\phi \rangle \quad (2.6)$$

in which $A_{\Lambda\Phi}$ and $a_{\lambda\phi}$ are the coordinates of the *covariant metric tensor* of the \mathbb{M}_l^2 and \mathbb{M}_r^2 respectively. The matrix representation of these tensors can be expressed by

$$\mathbf{A}_l := [A_{\Lambda\Phi}] = \begin{bmatrix} A_{11} & A_{12} \\ A_{21} & A_{22} \end{bmatrix} = \begin{bmatrix} E & F \\ F & G \end{bmatrix} \quad \text{vs.} \quad \mathbf{A}_r := [a_{\lambda\phi}] = \begin{bmatrix} a_{11} & a_{12} \\ a_{21} & a_{22} \end{bmatrix} = \begin{bmatrix} e & f \\ f & g \end{bmatrix} \quad (2.7)$$

where we set

$$\begin{aligned} E &= \langle \mathbf{A}_1, \mathbf{A}_1 \rangle & \text{vs.} & & e &= \langle \mathbf{a}_1, \mathbf{a}_1 \rangle \\ F &= \langle \mathbf{A}_1, \mathbf{A}_2 \rangle & \text{vs.} & & f &= \langle \mathbf{a}_1, \mathbf{a}_2 \rangle \\ G &= \langle \mathbf{A}_2, \mathbf{A}_2 \rangle & \text{vs.} & & g &= \langle \mathbf{a}_2, \mathbf{a}_2 \rangle \end{aligned}$$

The matrices $[A_{\Lambda\Phi}]$ and $[a_{\lambda\phi}]$ are *symmetric* and *positive-definite* [Visconti, 1992]. In general, curvilinear coordinates are not mutually orthogonal since

$$\langle \mathbf{A}_\Lambda, \mathbf{A}_\Phi \rangle = A_{\Lambda\Phi} \neq 0 \quad \text{vs.} \quad \langle \mathbf{a}_\lambda, \mathbf{a}_\phi \rangle = a_{\lambda\phi} \neq 0 \quad (2.8)$$

that means A_{12} and a_{12} are not zero. The reciprocal basis vectors \mathbf{A}^Λ and \mathbf{a}^λ are the solution of the systems

$$\langle \mathbf{A}^\Phi, \mathbf{A}_\Lambda \rangle = \delta_\Lambda^\Phi \quad \text{vs.} \quad \langle \mathbf{a}^\phi, \mathbf{a}_\lambda \rangle = \delta_\lambda^\phi \quad (2.9)$$

where the Kronecker symbols δ_Λ^Φ and δ_λ^ϕ take value 1 or 0 depending on whether the indices are identical or not. It can be verified that the unique solutions of (2.9) are

$$\mathbf{A}^\Phi = A^{\Phi\Lambda} \mathbf{A}_\Lambda \quad \text{vs.} \quad \mathbf{a}^\phi = a^{\phi\lambda} \mathbf{a}_\lambda \quad (2.10)$$

are the coordinates of *contravariant metric tensors* associated with coordinates of covariant metric tensors. In matrix form they can be represented by

$$[A^{\Phi\Lambda}] = [A_{\Phi\Lambda}]^{-1} \quad \text{vs.} \quad [a^{\phi\lambda}] = [a_{\phi\lambda}]^{-1}$$

From (2.10), by taking the scalar product, we find that

$$A^{\Phi\Lambda} = \langle \mathbf{A}^\Phi, \mathbf{A}^\Lambda \rangle \quad \text{vs.} \quad a^{\phi\lambda} = \langle \mathbf{a}^\phi, \mathbf{a}^\lambda \rangle$$

When curvilinear coordinates are orthogonal, then the directions of \mathbf{A}^Φ and \mathbf{A}_Φ and similarly directions of \mathbf{a}^ϕ and \mathbf{a}_ϕ will coincide. Hence, $A^{\Phi\Lambda} = A_{\Phi\Lambda} = 0$ as well $a^{\phi\lambda} = a_{\phi\lambda} = 0$.

In tensor analysis, so-called *mixed* tensors exist also, which are neither covariant nor contravariant. At least one of the indices of a mixed tensor will be a subscript (covariant) and at least one of the indices will be a superscript (contravariant). These tensors could differ from each other by the covariant or contravariant of their indices, e.g.

$$C_{\Psi}^{\Phi} = A^{\Phi\Lambda} C_{\Lambda\Psi} \quad \text{vs.} \quad C_{\Phi}^{\Psi} = A_{\Phi\Lambda} C^{\Lambda\Psi}$$

2.3 Deformation Gradients

Through the equation of motion (2.1) we have

$$d\theta^\phi = \theta_{,\Phi}^\phi d\Theta^\Phi \quad \text{vs.} \quad d\Theta^\Phi = \Theta_{,\phi}^\Phi d\theta^\phi \quad (2.11)$$

where

$$\theta_{,\Phi}^\phi := \frac{\partial \theta^\phi}{\partial \Theta^\Phi} \quad \text{vs.} \quad \Theta_{,\phi}^\Phi := \frac{\partial \Theta^\Phi}{\partial \theta^\phi}$$

are called *deformation gradients*. The set of deformation gradients can be described by the two *Jacobian* matrices \mathbf{J}_l and \mathbf{J}_r , which obey the matrix relations

$$\mathbf{J}_l := \left[\frac{\partial \theta^\phi}{\partial \Theta^\Phi} \right] = \mathbf{J}_r^{-1} \quad \text{vs.} \quad \mathbf{J}_r := \left[\frac{\partial \Theta^\Phi}{\partial \theta^\phi} \right] = \mathbf{J}_l^{-1}$$

If we substitute (2.11) into (2.5)

$$I(\Theta^1, \Theta^2) = A_{\Lambda\Phi} d\Theta^\Lambda d\Theta^\Phi = c_{\lambda\phi} d\theta^\lambda d\theta^\phi \quad \text{vs.} \quad I(\theta^1, \theta^2) = C_{\Lambda\Phi} d\Theta^\Lambda d\Theta^\Phi = a_{\lambda\phi} d\theta^\lambda d\theta^\phi \quad (2.12)$$

where

$$c_{\lambda\phi} = A_{\Lambda\Phi} \Theta_{,\lambda}^\Lambda \Theta_{,\phi}^\Phi \quad \text{vs.} \quad C_{\Lambda\Phi} = a_{\lambda\phi} \theta_{,\Lambda}^\lambda \theta_{,\Phi}^\phi$$

which are called respectively *Cauchy's deformation tensor* and *Green's deformation tensor*. Both of these tensors are *symmetric*, and both are *positive-definite*. Corresponding to the Cauchy and Green deformation tensors, new vectors \mathbf{c}_λ and \mathbf{C}_λ may be defined by

$$\mathbf{c}_\lambda := \frac{\partial \mathbf{X}}{\partial \theta^\lambda} = \frac{\partial \mathbf{X}}{\partial \Theta^\Lambda} \frac{\partial \Theta^\Lambda}{\partial \theta^\lambda} = \mathbf{A}_\Lambda \Theta_{,\lambda}^\Lambda \quad \text{vs.} \quad \mathbf{C}_\Lambda := \frac{\partial \mathbf{x}}{\partial \Theta^\Lambda} = \frac{\partial \mathbf{x}}{\partial \theta^\lambda} \frac{\partial \theta^\lambda}{\partial \Theta^\Lambda} = \mathbf{a}_\lambda \theta_{,\Lambda}^\lambda \quad (2.13)$$

from which it follows that

$$c_{\lambda\phi} = c_{\phi\lambda} = \langle \mathbf{c}_\lambda, \mathbf{c}_\phi \rangle \quad \text{vs.} \quad C_{\Lambda\Phi} = C_{\Phi\Lambda} = \langle \mathbf{C}_\Lambda, \mathbf{C}_\Phi \rangle \quad (2.14)$$

Hence, we have two different representations for the differential vectors $d\mathbf{X}$ and $d\mathbf{x}$, one in reference frame \mathbf{X}^K and the other in \mathbf{x}^k , i.e.,

$$d\mathbf{X} = \mathbf{A}_\Lambda d\Theta^\Lambda = \mathbf{c}_\lambda d\theta^\lambda \quad \text{vs.} \quad d\mathbf{x} = \mathbf{C}_\Lambda d\Theta^\Lambda = \mathbf{a}_\lambda d\theta^\lambda$$

Similarly for the FFF of surfaces we have

$$I(\Theta^1, \Theta^2) = A_{\Lambda\Phi} d\Theta^\Lambda d\Theta^\Phi = c_{\lambda\phi} d\theta^\lambda d\theta^\phi \quad \text{vs.} \quad I(\theta^1, \theta^2) = C_{\Lambda\Phi} d\Theta^\Lambda d\Theta^\Phi = a_{\lambda\phi} d\theta^\lambda d\theta^\phi$$

In map projection literature, Green's deformation tensor has been introduced as the *left Cauchy-Green deformation tensor* and Cauchy's deformation tensor as the *right Cauchy-Green deformation tensor*, which can be represented by matrix notations [Grafarend and Krumm, 2006]

$$\mathbf{C}_l := [C_{\Phi\Lambda}] \quad \text{vs.} \quad \mathbf{C}_r := [c_{\phi\lambda}] \quad (2.15)$$

By means of the left Cauchy-Green tensor, we have represented the right metric or the metric of the right surface \mathbb{M}_r^2 in the coordinates of the left surface \mathbb{M}_l^2 . By means of the right Cauchy-Green tensor, we have represented the left metric or the metric of the left surface \mathbb{M}_l^2 in the coordinates of the right surface \mathbb{M}_r^2 .

Theorem 2-1. (Polar Decomposition)

The deformation gradient matrix \mathbf{J} can be decomposed using the polar decomposition theorem into a product of two matrices

$$\mathbf{J} = \mathbf{R}\mathbf{U} = \mathbf{V}\mathbf{R} \quad (2.16)$$

The two matrices \mathbf{U} and \mathbf{V} in decomposition (2.16) are *symmetric* and *positive definite*

$$\mathbf{U}^T = \mathbf{U} \quad , \quad \mathbf{V}^T = \mathbf{V}$$

whereas \mathbf{R} is a proper *orthonormal* matrix

$$\mathbf{R}^T\mathbf{R} = \mathbf{R}\mathbf{R}^T = \mathbf{I}$$

The symmetric matrices \mathbf{U} and \mathbf{V} are called the *right* and *left stretch matrices*, and orthonormal matrix \mathbf{R} is called the *rotation matrix*. The stretch matrices are given in terms of \mathbf{J} by

$$\mathbf{U} = (\mathbf{J}\mathbf{J}^T)^{\frac{1}{2}} \quad , \quad \mathbf{V} = (\mathbf{J}^T\mathbf{J})^{\frac{1}{2}} \quad (2.17)$$

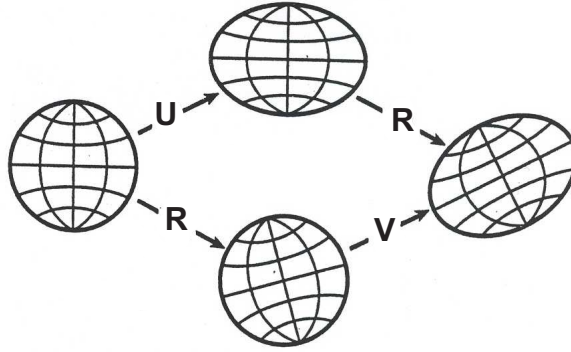


Figure 2.2: Schematic description of the polar decomposition of the deformation matrix $\mathbf{J} = \mathbf{R}\mathbf{U} = \mathbf{V}\mathbf{R}$.

Then by comparing (2.16) and (2.17) the rotation matrix \mathbf{R} can be derived by

$$\mathbf{R} = \mathbf{J}\mathbf{U}^{-1} = \mathbf{V}^{-1}\mathbf{J}$$

The physical interpretation of the polar decomposition (2.16) is : the deformation of an infinitesimal ball of material surrounding a particle can be viewed either as a symmetric stretch \mathbf{U} followed by a rigid rotation \mathbf{R} , or as a finite rotation \mathbf{R} followed by a symmetric stretched \mathbf{V} , which are illustrated by Fig. 2.2. The two stretch matrices are rotated versions of each other, e.g., they are related by an orthogonal transformation : $\mathbf{U} = \mathbf{R}^T\mathbf{V}\mathbf{R}$.

2.4 Strain Tensor: deformation tensor of first kind

The first measure of deformation is based upon differences between FFF of surfaces M_l^2 and M_r^2 , namely $I(\theta^1, \theta^2) - I(\Theta^1, \Theta^2)$, which implies a length change due to the deformation. Hence, according to (2.12) we have

$$I(\theta^1, \theta^2) - I(\Theta^1, \Theta^2) = 2E_{\Phi\Lambda} d\Theta^\Lambda d\Theta^\Phi = 2e_{\phi\lambda} d\theta^\lambda d\theta^\phi$$

where

$$E_{\Lambda\Phi} = E_{\Phi\Lambda} := \frac{1}{2}(C_{\Lambda\Phi} - A_{\Lambda\Phi}) \quad \text{vs.} \quad e_{\lambda\phi} = e_{\phi\lambda} := \frac{1}{2}(a_{\lambda\phi} - c_{\lambda\phi}) \quad (2.18)$$

are respectively called *Lagrangian* and *Eulerian strain tensors*. Following the map projection conventions, the Lagrangian strain tensor is called the *left Euler-Lagrange strain tensor* and the Eulerian strain tensor the *right Euler-Lagrange strain tensor*. The matrix representation of them are given by

$$\mathbf{E}_l := [E_{\Lambda\Phi}] \quad \text{vs.} \quad \mathbf{E}_r := [e_{\lambda\phi}]$$

Unlike the Cauchy-Green deformation tensors which are positive due to the positive-definite property of the deformation tensors, the eigenvalues of the Euler-Lagrange deformation tensors can be negative or positive.

The *displacement vector* \mathbf{u} is defined as the vector that extends from a material point in undeformed surface M_l^2 to the same material point in deformed surface M_r^2 . Thus

$$\mathbf{u} = \mathbf{x} - \mathbf{X} + \mathbf{t}$$

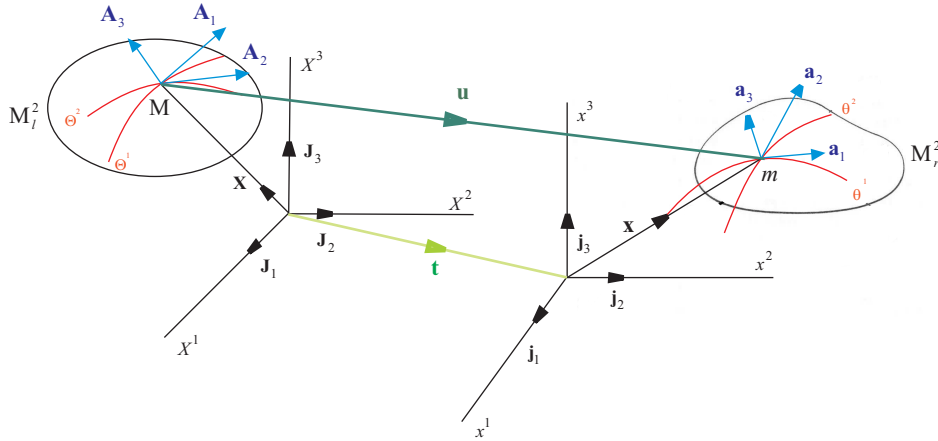


Figure 2.3: Displacement vector.

which is illustrated by Fig. 2.3. If we consider the translation vector \mathbf{t} in order of magnitude to be smaller than vectors \mathbf{x} and \mathbf{X} , namely $\mathbf{t} \ll \mathbf{X}$ and $\mathbf{t} \ll \mathbf{x}$, then deformation tensors are insensitive to it. The displacement vector will have components \tilde{U}^K referring to the curvilinear coordinate system $\{\Theta^1, \Theta^1\}$ and \tilde{u}^k referring to the $\{\theta^1, \theta^1\}$ such that

$$\mathbf{u} = \tilde{U}^K \mathbf{A}_K = \tilde{U}_K \mathbf{A}^K \quad \text{vs.} \quad \mathbf{u} = \tilde{u}^k \mathbf{a}_k = \tilde{u}_k \mathbf{a}^k \quad (2.19)$$

or by splitting curvilinear basis vectors into a set of surface basis vectors and unit normal vectors, we find

$$\mathbf{u} = \tilde{U}^\Phi \mathbf{A}_\Phi + \tilde{U}^3 \mathbf{A}_3 = \tilde{U}_\Phi \mathbf{A}^\Phi + \tilde{U}_3 \mathbf{A}^3 \quad \text{vs.} \quad \mathbf{u} = \tilde{u}^\phi \mathbf{a}_\phi + \tilde{u}^3 \mathbf{a}_3 = \tilde{u}_\phi \mathbf{a}^\phi + \tilde{u}_3 \mathbf{a}^3$$

Let us take the scalar product of (2.19) with \mathbf{A}^K and \mathbf{a}^k respectively

$$\tilde{U}^K = \langle \mathbf{u}, \mathbf{A}^K \rangle \quad \text{vs.} \quad \tilde{u}^k = \langle \mathbf{u}, \mathbf{a}^k \rangle \quad (2.20)$$

or by scalar multiplication of (2.19) with \mathbf{A}_K and \mathbf{a}_k we obtain

$$\tilde{U}_K = \langle \mathbf{u}, \mathbf{A}_K \rangle \quad \text{vs.} \quad \tilde{u}_k = \langle \mathbf{u}, \mathbf{a}_k \rangle \quad (2.21)$$

It is convenient for practical applications to express strain tensors (2.18) as a function of the displacement vector [Sansour et al., 1997; Voosoghi, 2000; Pietraszkiewicz and Szwabowicz, 2007]

$$E_{\Lambda\Phi} = \frac{1}{2}(\langle \mathbf{u}_{,\Lambda}, \mathbf{u}_{,\Phi} \rangle + \langle \mathbf{u}_{,\Lambda}, \mathbf{A}_\Phi \rangle + \langle \mathbf{A}_\Lambda, \mathbf{u}_{,\Phi} \rangle) \quad \text{vs.} \quad e_{\lambda\phi} = \frac{1}{2}(\langle \mathbf{u}_{,\lambda}, \mathbf{u}_{,\phi} \rangle + \langle \mathbf{u}_{,\lambda}, \mathbf{a}_\phi \rangle + \langle \mathbf{a}_\lambda, \mathbf{u}_{,\phi} \rangle) \quad (2.22)$$

where

$$\mathbf{u}_{,\Lambda} = \frac{\partial \mathbf{u}}{\partial \Theta^\Lambda} \quad \text{vs.} \quad \mathbf{u}_{,\lambda} = \frac{\partial \mathbf{u}}{\partial \theta^\lambda}$$

are first-order partial derivatives of the displacement vector with respect to the material and spatial curvilinear coordinates. A more detailed description of these derivatives and their relations is presented in Appendix A.

2.4.1 An Analytical Example

Since the Earth is in fact flattened slightly at the poles and bulges somewhat at the equator, the geometrical figure used in geodesy to most nearly approximate the shape of the Earth is an ellipsoid of revolution. It is used to represent the Earth's surface in geodetic calculations, because such calculations are simpler than those with more complicated mathematical models. It can be used also for deformation analysis, in order to describe crustal deformations.

Hence, the embedding of an ellipsoid-of-revolution with semi-major axis A_1 and A_2 as a semi-minor axis and $E^2 = \frac{A_1^2 - A_2^2}{A_1^2}$ as square of the first eccentricity, is governed by vector field [Grafarend and Engels, 1992]

$$\mathbf{X}(\Lambda, \Phi) = \mathbf{J}_1 X^1(\Lambda, \Phi) + \mathbf{J}_2 X^2(\Lambda, \Phi) + \mathbf{J}_3 X^3(\Lambda, \Phi) \quad (2.23)$$

$$\mathbf{X}(\Lambda, \Phi) = [\mathbf{J}_1 \quad \mathbf{J}_2 \quad \mathbf{J}_3] \begin{bmatrix} \left(\frac{A_1}{\sqrt{1-E^2 \sin^2 \Phi}} + H(\Lambda, \Phi) \right) \cos(\Lambda) \cos(\Phi) \\ \left(\frac{A_1}{\sqrt{1-E^2 \sin^2 \Phi}} + H(\Lambda, \Phi) \right) \sin(\Lambda) \cos(\Phi) \\ \left(\frac{A_1(1-E^2)}{\sqrt{1-E^2 \sin^2 \Phi}} + H(\Lambda, \Phi) \right) \sin(\Phi) \end{bmatrix} \quad (2.24)$$

and can be considered for the representation of Earth's surface before deformation, as a left surface \mathbb{M}_l^2 . In Eq.(2.24), the ellipsoidal height $H(\Lambda, \Phi)$ is described as a function of latitude and longitude.

We can get similar Eqs. (2.23) and (2.24) for the representation of Earth's surface after deformation, as a right surface \mathbb{M}_r^2 by

$$\mathbf{x}(\lambda, \phi) = \mathbf{j}_1 x^1(\lambda, \phi) + \mathbf{j}_2 x^2(\lambda, \phi) + \mathbf{j}_3 x^3(\lambda, \phi)$$

$$\mathbf{x}(\lambda, \phi) = [\mathbf{j}_1 \ \mathbf{j}_2 \ \mathbf{j}_3] \begin{bmatrix} \left(\frac{A_1}{\sqrt{1-E^2 \sin^2 \phi}} + h(\lambda, \phi) \right) \cos(\lambda) \cos(\phi) \\ \left(\frac{A_1}{\sqrt{1-E^2 \sin^2 \phi}} + h(\lambda, \phi) \right) \sin(\lambda) \cos(\phi) \\ \left(\frac{A_1(1-E^2)}{\sqrt{1-E^2 \sin^2 \phi}} + h(\lambda, \phi) \right) \sin(\phi) \end{bmatrix} \quad (2.25)$$

respectively. The coordinates (X^1, X^2, X^3) and (x^1, x^2, x^3) of the placement vectors $\mathbf{X}(\Lambda, \Phi)$ and $\mathbf{x}(\lambda, \phi)$ are expressed in the left and right orthogonal fixed frames $\{\mathbf{J}_1, \mathbf{J}_2, \mathbf{J}_3 \mid O\}$ and $\{\mathbf{j}_1, \mathbf{j}_2, \mathbf{j}_3 \mid o\}$ at their origins O and o .

Next, we are going to construct the tangent basis vectors in \mathbb{M}_r^2 and \mathbb{M}_r^2 . The vector field $\mathbf{X}(\Lambda, \Phi)$ is locally characterized by the field of tangent basis vectors $\{\frac{\partial \mathbf{X}}{\partial \Lambda}, \frac{\partial \mathbf{X}}{\partial \Phi}\}$, the *Jacobi map* with respect to the Λ and Φ . Namely according to Eq. (2.3) and (2.24) we have

$$\left\{ \frac{\partial \mathbf{X}}{\partial \Lambda}, \frac{\partial \mathbf{X}}{\partial \Phi} \right\} = [\mathbf{J}_1 \ \mathbf{J}_2 \ \mathbf{J}_3] \begin{bmatrix} X_{,\Lambda}^1 & X_{,\Phi}^1 \\ X_{,\Lambda}^2 & X_{,\Phi}^2 \\ X_{,\Lambda}^3 & X_{,\Phi}^3 \end{bmatrix}$$

$$\left\{ \frac{\partial \mathbf{X}}{\partial \Lambda}, \frac{\partial \mathbf{X}}{\partial \Phi} \right\} = [\mathbf{J}_1 \ \mathbf{J}_2 \ \mathbf{J}_3] \begin{bmatrix} \cos \Phi (H_{,\Lambda} \cos \Lambda - (N + H) \sin \Lambda) & \cos \Lambda (H_{,\Phi} \cos \Phi - (M + H) \sin \Phi) \\ \cos \Phi (H_{,\Lambda} \sin \Lambda + (N + H) \cos \Lambda) & \sin \Lambda (H_{,\Phi} \cos \Phi - (M + H) \sin \Phi) \\ \sin \Phi H_{,\Lambda} & H_{,\Phi} \sin \Phi + (M + H) \cos \Phi \end{bmatrix}$$

in addition, the vector field $\mathbf{x}(\lambda, \phi)$ is locally characterized by the field of tangent basis vectors $\{\frac{\partial \mathbf{x}}{\partial \lambda}, \frac{\partial \mathbf{x}}{\partial \phi}\}$, the *Jacobi map* with respect to the λ and ϕ , namely

$$\left\{ \frac{\partial \mathbf{x}}{\partial \lambda}, \frac{\partial \mathbf{x}}{\partial \phi} \right\} = [\mathbf{j}_1 \ \mathbf{j}_2 \ \mathbf{j}_3] \begin{bmatrix} x_{,\lambda}^1 & x_{,\phi}^1 \\ x_{,\lambda}^2 & x_{,\phi}^2 \\ x_{,\lambda}^3 & x_{,\phi}^3 \end{bmatrix}$$

$$\left\{ \frac{\partial \mathbf{x}}{\partial \lambda}, \frac{\partial \mathbf{x}}{\partial \phi} \right\} = [\mathbf{j}_1 \ \mathbf{j}_2 \ \mathbf{j}_3] \begin{bmatrix} \cos \phi (h_{,\lambda} \cos \lambda - (n + h) \sin \lambda) & \cos \lambda (h_{,\phi} \cos \phi - (m + h) \sin \phi) \\ \cos \phi (h_{,\lambda} \sin \lambda + (n + h) \cos \lambda) & \sin \lambda (h_{,\phi} \cos \phi - (m + h) \sin \phi) \\ \sin \phi h_{,\lambda} & h_{,\phi} \sin \phi + (m + h) \cos \phi \end{bmatrix}$$

where $H_{,\Lambda}$, $H_{,\Phi}$ and $h_{,\lambda}$, $h_{,\phi}$ denote first-order partial derivatives of the ellipsoidal height functions with respect to the surface coordinates (Λ, Φ) and (λ, ϕ) , respectively. The normal radiuses of curvatures N/n and meridional radiuses of curvatures M/m of the reference ellipsoid are given by

$$N = \frac{A_1}{(1 - E^2 \sin^2 \Phi)^{\frac{1}{2}}} \quad \text{vs.} \quad n = \frac{A_1}{(1 - E^2 \sin^2 \phi)^{\frac{1}{2}}}$$

$$M = \frac{A_1(1 - E^2)}{(1 - E^2 \sin^2 \Phi)^{\frac{3}{2}}} \quad \text{vs.} \quad m = \frac{A_1(1 - E^2)}{(1 - E^2 \sin^2 \phi)^{\frac{3}{2}}}$$

Next, we are going to identify the coordinates of the left metric tensor $A_{\Lambda\Phi}$ and the right metric tensor $a_{\lambda\phi}$, in particular through Eq. (2.6), from the inner products

$$\begin{aligned} \left\langle \frac{\partial \mathbf{X}}{\partial \Lambda}, \frac{\partial \mathbf{X}}{\partial \Lambda} \right\rangle &= H_{,\Lambda}^2 + (N + H)^2 \cos^2 \Phi := A_{11} & \text{vs.} & \quad \left\langle \frac{\partial \mathbf{x}}{\partial \lambda}, \frac{\partial \mathbf{x}}{\partial \lambda} \right\rangle = h_{,\lambda}^2 + (n + h)^2 \cos^2 \phi := a_{11} \\ & \left\langle \frac{\partial \mathbf{X}}{\partial \Lambda}, \frac{\partial \mathbf{X}}{\partial \Phi} \right\rangle = H_{,\Lambda} H_{,\Phi} := A_{12} & \text{vs.} & \quad \left\langle \frac{\partial \mathbf{x}}{\partial \lambda}, \frac{\partial \mathbf{x}}{\partial \phi} \right\rangle = h_{,\lambda} h_{,\phi} := a_{12} \\ & \left\langle \frac{\partial \mathbf{X}}{\partial \Phi}, \frac{\partial \mathbf{X}}{\partial \Phi} \right\rangle = H_{,\Phi}^2 + (M + H)^2 := A_{22} & \text{vs.} & \quad \left\langle \frac{\partial \mathbf{x}}{\partial \phi}, \frac{\partial \mathbf{x}}{\partial \phi} \right\rangle = h_{,\phi}^2 + (m + h)^2 := a_{22} \end{aligned}$$

and FFF of surfaces

$$I(\Theta^1, \Theta^2) = (H_{,\Lambda}^2 + (N + H)^2 \cos^2 \Phi) d\Lambda^2 + (H_{,\Lambda} H_{,\Phi}) d\Lambda d\Phi + (H_{,\Phi}^2 + (M + H)^2) d\Phi^2$$

versus

$$I(\theta^1, \theta^2) = h_{,\lambda}^2 + (n + h)^2 \cos^2 \phi) d\lambda^2 + (h_{,\lambda} h_{,\phi}) d\lambda d\phi + (h_{,\phi}^2 + (m + h)^2) d\phi^2$$

Resorting to this identification, we obtain the matrix form of the left metric tensor, i.e. \mathbf{A}_l , and the matrix form of the right metric tensor, i.e. \mathbf{A}_r , according to

$$\begin{aligned} \mathbf{A}_l := [A_{\Lambda\Phi}] &= & \text{vs.} & \quad \mathbf{A}_r := [a_{\lambda\phi}] = \\ = \begin{bmatrix} H_{,\Lambda}^2 + (N + H)^2 \cos^2 \Phi & H_{,\Lambda} H_{,\Phi} \\ H_{,\Lambda} H_{,\Phi} & H_{,\Phi}^2 + (M + H)^2 \end{bmatrix} & \text{vs.} & = \begin{bmatrix} h_{,\lambda}^2 + (n + h)^2 \cos^2 \phi & h_{,\lambda} h_{,\phi} \\ h_{,\lambda} h_{,\phi} & h_{,\phi}^2 + (m + h)^2 \end{bmatrix} \end{aligned}$$

Hence, through Eqs. (2.13), (2.14) and (2.15), Cauchy-Green deformation tensors can be derived by

$$\begin{aligned} C_{\Lambda\Phi} = \langle \mathbf{C}_\Lambda, \mathbf{C}_\Phi \rangle &= \left\langle \frac{\partial \mathbf{x}}{\partial \Theta^\Lambda}, \frac{\partial \mathbf{x}}{\partial \Theta^\Phi} \right\rangle & \text{vs.} & \quad c_{\lambda\phi} = \langle \mathbf{c}_\lambda, \mathbf{c}_\phi \rangle = \left\langle \frac{\partial \mathbf{X}}{\partial \theta^\lambda}, \frac{\partial \mathbf{X}}{\partial \theta^\phi} \right\rangle \\ &= \left\langle \frac{\partial(\mathbf{u} + \mathbf{X} - \mathbf{t})}{\partial \Theta^\Lambda}, \frac{\partial(\mathbf{u} + \mathbf{X} - \mathbf{t})}{\partial \Theta^\Phi} \right\rangle & \text{vs.} & \quad = \left\langle \frac{\partial(\mathbf{x} - \mathbf{u} + \mathbf{t})}{\partial \theta^\lambda}, \frac{\partial(\mathbf{x} - \mathbf{u} + \mathbf{t})}{\partial \theta^\phi} \right\rangle \\ &= \langle \mathbf{u}_{,\Lambda}, \mathbf{u}_{,\Phi} \rangle + \langle \mathbf{u}_{,\Lambda}, \mathbf{X}_{,\Phi} \rangle + & \text{vs.} & \quad = \langle \mathbf{u}_{,\lambda}, \mathbf{u}_{,\phi} \rangle + \langle \mathbf{u}_{,\lambda}, \mathbf{X}_{,\phi} \rangle - \\ & \quad \langle \mathbf{X}_{,\Lambda}, \mathbf{u}_{,\phi} \rangle + \langle \mathbf{X}_{,\Lambda}, \mathbf{X}_{,\Phi} \rangle & \text{vs.} & \quad \langle \mathbf{x}_{,\lambda}, \mathbf{u}_{,\phi} \rangle + \langle \mathbf{x}_{,\lambda}, \mathbf{x}_{,\phi} \rangle \end{aligned} \quad (2.26)$$

To complete this example we calculate Lagrangian and Eulerian strain tensors. Then according to Eqs. (2.18) and (2.26) we have

$$E_{\Lambda\Phi} = \frac{1}{2} (\langle \mathbf{u}_{,\Lambda}, \mathbf{u}_{,\Phi} \rangle + \langle \mathbf{u}_{,\Lambda}, \mathbf{A}_\Phi \rangle + \langle \mathbf{A}_\Lambda, \mathbf{u}_{,\Phi} \rangle) \quad \text{vs.} \quad e_{\lambda\phi} = \frac{1}{2} (\langle \mathbf{u}_{,\lambda}, \mathbf{u}_{,\phi} \rangle + \langle \mathbf{u}_{,\lambda}, \mathbf{a}_\phi \rangle + \langle \mathbf{a}_\lambda, \mathbf{u}_{,\phi} \rangle) \quad (2.27)$$

Hence through this analytical example we proved Eq. (2.22).

Remark 2.1 Apart from the Cauchy-Green and Euler-Lagrange deformation tensors used to describe the changes in the geometry of the deforming body induced by deformation, it is often convenient in deformation analysis to employ other equivalent deformation measures. Tab. (2.1) collects the most common deformation tensors of first kind and their definitions appearing in various applications in deformation analysis [Grafarend and Krumm, 2006, page 38]

Table 2.1: Various measures for deformation (based on FFF).

Name	Symbol	Definitions
Left Cauchy – Green strain tensor	\mathbf{E}_1	\mathbf{C}_l
Right Cauchy – Green strain tensor	\mathbf{E}_2	\mathbf{C}_r
Piola	\mathbf{E}_3	\mathbf{C}_l^{-1}
Finger	\mathbf{E}_4	\mathbf{C}_r^{-1}
Hencky	\mathbf{E}_5	$\frac{1}{2} \ln \mathbf{C}_l$
Hencky	\mathbf{E}_6	$\frac{1}{2} \ln \mathbf{C}_r$
Left Euler – Lagrange strain tensor	\mathbf{E}_7	$\frac{1}{2}(\mathbf{C}_l - \mathbf{A}_l)$
Right Euler – Lagrange strain tensor	\mathbf{E}_8	$\frac{1}{2}(\mathbf{A}_r - \mathbf{C}_r)$
Karni – Reiner	\mathbf{E}_9	$\frac{1}{2}(\mathbf{C}_l^{-1} - \mathbf{A}_l)$
Karni – Reiner	\mathbf{E}_{10}	$\frac{1}{2}(\mathbf{A}_r - \mathbf{C}_r^{-1})$

2.4.2 Eigenspace Analysis, Strain Tensor

Let us consider the matrix forms of left Euler-Lagrange strain tensor and left metric tensor are given by

$$\mathbf{E}_l = \begin{bmatrix} E_{11} & E_{12} \\ E_{12} & E_{22} \end{bmatrix} \quad \mathbf{A}_l = \begin{bmatrix} A_{11} & A_{12} \\ A_{12} & A_{22} \end{bmatrix}$$

where both matrices are symmetric. Finding the eigenspectra elements of matrices $\{\mathbf{E}_l, \mathbf{A}_l\}$ leads us to obtaining a *general eigenvector-eigenvalue problem* of type

$$\mathbf{E}_l \mathbf{F}_l = \mathbf{D}_\Lambda \mathbf{A}_l \mathbf{F}_l \quad (2.28)$$

where $\mathbf{F}_l = [\mathbf{F}_1, \mathbf{F}_2] \in \mathbb{R}^{2 \times 2}$ is the matrix of eigenvectors and \mathbf{D}_Λ is the diagonal matrix of eigenvalues, namely $\mathbf{D}_\Lambda = \text{diag}[\Lambda_1, \Lambda_2]$. Through (2.28), eigenvalues and eigenvectors can be obtained by

$$\mathbf{E}_l \mathbf{F}_l - \mathbf{D}_\Lambda \mathbf{A}_l \mathbf{F}_l = 0 \implies \det(\mathbf{E}_l - \mathbf{D}_\Lambda \mathbf{A}_l) = 0 \quad (2.29)$$

Solving (2.29) for eigenvalues of the matrices $\{\mathbf{E}_l, \mathbf{A}_l\}$ yields [Grafarend, 1995]

$$\Lambda_{1,2} = \frac{1}{2} \{ \text{tr}(\mathbf{E}_l \mathbf{A}_l^{-1}) \pm \sqrt{(\text{tr}(\mathbf{E}_l \mathbf{A}_l^{-1}))^2 - 4 \det(\mathbf{E}_l \mathbf{A}_l^{-1})} \}, \quad \Lambda_1, \Lambda_2 \in \mathbb{R} \quad (2.30)$$

whereas here Λ_1 and Λ_2 are the *principal stretches*. A deformation portrait when $\text{sign} \Lambda_1 = \text{sign} \Lambda_2$ will be the *strain ellipse* and as *strain hyperbola* if $\text{sign} \Lambda_1 \neq \text{sign} \Lambda_2$.

In the first case, the axes of the strain ellipse are directed along the eigenvectors of the strain ellipse; the semi-major axis of strain ellipse is identified with the *maximum principal strain*, the semi-minor axis with the *minimum principal strain*, constrained by $\text{sign}\Lambda_1 = \text{sign}\Lambda_2$. If $\text{sign}\Lambda_1 = \text{sign}\Lambda_2 = +1$, we speak about *extension* if $\text{sign}\Lambda_1 = \text{sign}\Lambda_2 = -1$, we will speak of *contraction*. Alternatively, in the second case, the axis of *strain hyperbola* are directed along the eigenvectors of deformation tensors, indicated by the "real axis" showing Λ_1 and 'imaginary axis' with $|\Lambda_2|$, for instance [Grafarend and Krumm, 2006].

Inserting eigenvalues (2.30) into (2.28), we can get eigenvectors by

$$\mathbf{F}_1 = ((E_{22} - \Lambda_1 A_{22})^2 A_{11} - 2(E_{12} - \Lambda_1 A_{12})(E_{22} - \Lambda_1 A_{22})A_{12} + (E_{12} - \Lambda_1 A_{12})^2 A_{22})^{-1/2} \begin{bmatrix} E_{22} - \Lambda_1 A_{22} \\ -(E_{12} - \Lambda_1 A_{12}) \end{bmatrix}$$

$$\mathbf{F}_2 = ((E_{11} - \Lambda_2 A_{11})^2 A_{22} - 2(E_{12} - \Lambda_2 A_{12})(E_{11} - \Lambda_2 A_{11})A_{12} + (E_{12} - \Lambda_2 A_{12})^2 A_{11})^{-1/2} \begin{bmatrix} -(E_{12} - \Lambda_2 A_{12}) \\ E_{11} - \Lambda_2 A_{11} \end{bmatrix}$$

In general, on the surface \mathbb{M}_l^2 , we have *non-orthogonal conjugate axis* of quadratic forms $\langle \mathbf{F}_1, \mathbf{F}_2 \rangle \neq 0$, contrary to the "plane" which has *orthogonal conjugate of axis* $\langle \mathbf{F}_1, \mathbf{F}_2 \rangle = 0$. Since in \mathbb{E}^2 or plane, metric is unit $\mathbf{A} = \text{diag}(1, 1)$, while 2D Riemannian Manifold \mathbb{M}^2 or 2D surface, equipped with natural metric which is not unit (see Eq. (2.8)) .

The orientation of semi-major axis of quadratic forms on the surface \mathbb{M}_l^2 is represented by Ψ through Eqs. (2.31) and (2.32). Its illustration in left Euclidean space \mathbb{E}_l^2 with basis $\{\mathbf{E}_1, \mathbf{E}_2\}$ is anti-clockwise with respect to the 1-axis, namely east direction [Eisele and Mason, 1970]

$$\Psi = \arccos\left(\frac{\langle \mathbf{F}_1, \mathbf{E}_l \rangle}{\|\mathbf{F}_1\|}\right) = \arccos\left(\frac{F_1^1}{\|\mathbf{F}_1\|}\right) \quad \text{subject to} \quad \|\mathbf{F}_1\|^2 = \max\{\|\mathbf{F}_1\|, \|\mathbf{F}_2\|\}, \quad \forall \Psi \in \left[-\frac{\pi}{2}, \frac{\pi}{2}\right] \quad (2.31)$$

or

$$\Psi = \arccos\left(\frac{\langle \mathbf{F}_2, \mathbf{E}_l \rangle}{\|\mathbf{F}_2\|}\right) = \arccos\left(\frac{F_2^1}{\|\mathbf{F}_2\|}\right) \quad \text{subject to} \quad \|\mathbf{F}_2\|^2 = \max\{\|\mathbf{F}_1\|, \|\mathbf{F}_2\|\}, \quad \forall \Psi \in \left[-\frac{\pi}{2}, \frac{\pi}{2}\right] \quad (2.32)$$

Then according to (2.30) and (2.31) or (2.32), for a symmetric strain matrix \mathbf{E}_l with associated metric \mathbf{A}_l , the eigenspace components will consist of : eigenvalues Λ_1 and Λ_2 , as well the as orientation parameter Ψ

$$\mathbf{Y} = \begin{bmatrix} \Lambda_1 \\ \Lambda_2 \\ \Psi \end{bmatrix} = \frac{1}{2} \begin{bmatrix} \text{tr}(\mathbf{E}_l \mathbf{A}_l^{-1}) + \sqrt{(\text{tr}(\mathbf{E}_l \mathbf{A}_l^{-1}))^2 - 4\det(\mathbf{E}_l \mathbf{A}_l^{-1})} \\ \text{tr}(\mathbf{E}_l \mathbf{A}_l^{-1}) - \sqrt{(\text{tr}(\mathbf{E}_l \mathbf{A}_l^{-1}))^2 - 4\det(\mathbf{E}_l \mathbf{A}_l^{-1})} \\ \arccos\left(\frac{\langle \mathbf{F}_i, \mathbf{E}_i \rangle}{\|\mathbf{F}_i\|}\right) \end{bmatrix} \quad (2.33)$$

The similar procedure can be performed for the right-pair of matrices $\{\mathbf{E}_r, \mathbf{A}_r\}$. Then right eigenspace components will consist of

$$\mathbf{y} = \begin{bmatrix} \lambda_1 \\ \lambda_2 \\ \psi \end{bmatrix} = \frac{1}{2} \begin{bmatrix} \text{tr}(\mathbf{E}_r \mathbf{A}_r^{-1}) + \sqrt{(\text{tr}(\mathbf{E}_r \mathbf{A}_r^{-1}))^2 - 4\det(\mathbf{E}_r \mathbf{A}_r^{-1})} \\ \text{tr}(\mathbf{E}_r \mathbf{A}_r^{-1}) - \sqrt{(\text{tr}(\mathbf{E}_r \mathbf{A}_r^{-1}))^2 - 4\det(\mathbf{E}_r \mathbf{A}_r^{-1})} \\ \arccos\left(\frac{\langle \mathbf{f}_i, \mathbf{e}_i \rangle}{\|\mathbf{f}_i\|}\right) \end{bmatrix} \quad (2.34)$$

where $\{\mathbf{e}_1, \mathbf{e}_2\}$ are basis in right Euclidean space \mathbb{E}_r^2 .

Invariants of Strain Tensor

In mathematics and theoretical physics, an invariant is that which remains unchanged under some transformation. The invariants do not change with rotation of the coordinate system (they are objective). Obviously, any function of the invariants only is also objective. Examples of invariants in deformation analysis include the eigenspace components of the strain tensor. The first properties of invariants are the sum of the eigenvalues of the strain tensor; their sum defines the rate of surface *dilatation* as a surface invariant by

$$\Delta = \Lambda_1 + \Lambda_2 = \text{tr}(\mathbf{E}_r \mathbf{A}_r^{-1}) \quad \text{vs.} \quad \delta = \lambda_1 + \lambda_2 = \text{tr}(\mathbf{E}_l \mathbf{A}_l^{-1}) \quad (2.35)$$

The surface dilatation is the relative change of area. The surface dilatation of zero corresponds to no change of area, surface dilatation of positive values relates to expansion of the area and negative dilatations correspond to a reduction of the area.

The second properties of invariants are the differences between a pair of eigenvalues, which is a so-called surface *maximum shear strain*

$$\Upsilon = \Lambda_1 - \Lambda_2 = \sqrt{(\text{tr}(\mathbf{E}_l \mathbf{A}_l^{-1}))^2 - 4\det(\mathbf{E}_l \mathbf{A}_l^{-1})} \quad \text{vs.} \quad v = \lambda_1 - \lambda_2 = \sqrt{(\text{tr}(\mathbf{E}_r \mathbf{A}_r^{-1}))^2 - 4\det(\mathbf{E}_r \mathbf{A}_r^{-1})} \quad (2.36)$$

where Υ and v are the shear across the directions of their maximum values.

The third property of invariants is the *rotation around the normal* which is introduced in deformation analysis [Pietraszkiewicz, 1977; Stein, 1980; Ernst, 1981; Voosoghi, 2000; Grafarend and Voosoghi, 2003]

$$\Gamma = \frac{1}{2} G^{\Lambda\Phi} R_{\Lambda\Phi} \quad \text{vs.} \quad \gamma = \frac{1}{2} g^{\lambda\phi} r_{\lambda\phi} \quad (2.37)$$

where

$$[G^{\Lambda\Phi}] = \begin{bmatrix} 0 & \frac{1}{\sqrt{\det \mathbf{A}_l}} \\ -\frac{1}{\sqrt{\det \mathbf{A}_l}} & 0 \end{bmatrix} \quad \text{vs.} \quad [g^{\lambda\phi}] = \begin{bmatrix} 0 & \frac{1}{\sqrt{\det \mathbf{A}_r}} \\ -\frac{1}{\sqrt{\det \mathbf{A}_r}} & 0 \end{bmatrix}$$

which matrix notation for rotation tensors $R_{\Lambda\Phi}$ and $r_{\lambda\phi}$ can be obtained via

$$\mathbf{R}_l := [R_{\Lambda\Phi}] = \frac{1}{2} \begin{bmatrix} 0 & \frac{\partial \tilde{U}_1}{\partial \Theta_2} - \frac{\partial \tilde{U}_2}{\partial \Theta_1} \\ \frac{\partial \tilde{U}_2}{\partial \Theta_1} - \frac{\partial \tilde{U}_1}{\partial \Theta_2} & 0 \end{bmatrix} \quad \text{vs.} \quad \mathbf{R}_r := [r_{\lambda\phi}] = \frac{1}{2} \begin{bmatrix} 0 & \frac{\partial \tilde{u}_1}{\partial \theta_2} - \frac{\partial \tilde{u}_2}{\partial \theta_1} \\ \frac{\partial \tilde{u}_2}{\partial \theta_1} - \frac{\partial \tilde{u}_1}{\partial \theta_2} & 0 \end{bmatrix} \quad (2.38)$$

Simultaneous Diagonalization

Due to the intricate relations between elements of strain tensor on one side and eigenspace components on the other side, which are established by Eqs. (2.33) and (2.34), we convert these relations to simple equations. Hence, in conformity with standard lemma of matrix algebra both pair matrices $\{\mathbf{E}_l, \mathbf{A}_l\}$ and $\{\mathbf{E}_r, \mathbf{A}_r\}$ can be *simultaneously diagonalized*, separately, one matrix form of associated metrics being the unit matrix. We briefly outline the simultaneous diagonalization of the left symmetric matrix \mathbf{E}_l relative to the left symmetric positive-definite metric \mathbf{A}_l , then drawing the same conclusion about the right pair matrices.

Two matrices are said to be *simultaneously diagonalizable* if they are diagonalized by a same invertible matrix. In other words, if \mathbf{E}_l and \mathbf{A}_l commute $\mathbf{E}_l\mathbf{A}_l = \mathbf{A}_l\mathbf{E}_l$ then \mathbf{E}_l and \mathbf{A}_l can be simultaneously diagonalized. In mathematical terms, we want to find a matrix \mathbf{F} that simultaneously diagonalizes both \mathbf{A}_l and \mathbf{E}_l

$$\mathbf{F}^T \mathbf{A}_l \mathbf{F} = \begin{bmatrix} 1 & 0 \\ 0 & 1 \end{bmatrix} \quad \mathbf{F}^T \mathbf{E}_l \mathbf{F} = \begin{bmatrix} \Lambda_1 & 0 \\ 0 & \Lambda_2 \end{bmatrix}$$

We express the construction of simultaneous diagonalization through the sequence of three steps which are illustrated by Fig. 2.4.

Step 1. Let us consider two quadratic forms relative to strain and metric matrices, e.g., Q_1 and Q_2 respectively. A Geometrical representation of Q_1 can be performed using an ellipse, in the left top side Fig. 2.4 (a), based on the fact that the associated matrix form is positive definite. In Fig. 2.4 (b), we represented Q_2 related to symmetric matrix \mathbf{E}_l , which can be illustrated by an ellipse or hyperbola.

Note that, illustrated Figs. 2.4 (a) and 2.4 (b) neither have oriented axes with respect to each other nor are they aligned with coordinate axes, corresponding to the fact that neither \mathbf{E}_l nor \mathbf{A}_l are diagonal matrices.

Continuing the first step by finding the eigenvalue-eigenvector of matrix \mathbf{A}_l , on domain of left Euclidean space \mathbb{E}_l^2

$$\mathbf{A}_l \mathbf{V}_l = \Lambda_A \mathbf{V}_l$$

where columns of matrix \mathbf{V}_l are eigenvectors

$$\mathbf{V}_l = [\mathbf{V}_1 \quad \mathbf{V}_2] \quad \text{where} \quad \mathbf{V}_1 \perp \mathbf{V}_2$$

Since \mathbf{V}_l is an *orthonormal* matrix, it can be represented by

$$\mathbf{V}_l = \begin{bmatrix} \cos \varphi & -\sin \varphi \\ \sin \varphi & \cos \varphi \end{bmatrix}, \quad \forall \varphi \in \left[-\frac{\pi}{2}, \frac{\pi}{2}\right]$$

which, indeed is a rotation matrix by a counterclockwise angle φ in a fixed coordinate system.

Step2. Diagonalization of matrix \mathbf{A}_l , under the rotation matrix (orthonormal) \mathbf{V}_l . Hence, under this diagonalization, strain and its associated metric will convert to

$$\mathbf{A}'_l = \mathbf{V}_l^T \mathbf{A}_l \mathbf{V}_l \quad \mathbf{E}'_l = \mathbf{V}_l^T \mathbf{E}_l \mathbf{V}_l$$

which are illustrated by Figs. 2.4 (c) and 2.4 (d).

Step3. Transform \mathbf{A}'_l to become a unit circle, namely converting \mathbf{A}'_l to unit matrix. Hence, \mathbf{E}'_l will change correspondingly by

$$\mathbf{A}''_l = \mathbf{M}\mathbf{A}'_l\mathbf{M} = (\mathbf{V}_l\mathbf{M})^T\mathbf{A}_l(\mathbf{V}_l\mathbf{M}) = \mathbf{I} \quad \mathbf{E}''_l = \mathbf{M}\mathbf{E}'_l\mathbf{M} = (\mathbf{V}_l\mathbf{M})^T\mathbf{E}_l(\mathbf{V}_l\mathbf{M}) \quad (2.39)$$

or in matrix notations

$$\mathbf{A}''_l = \begin{bmatrix} 1 & 0 \\ 0 & 1 \end{bmatrix} \quad \mathbf{E}''_l = \begin{bmatrix} E''_{11} & E''_{12} \\ E''_{12} & E''_{22} \end{bmatrix}$$

where in (2.39) matrix \mathbf{M} is obtainable by

$$\mathbf{M} = \text{diag}\left(\frac{1}{\sqrt{A'_{11}}}, \frac{1}{\sqrt{A'_{22}}}\right)$$

which are illustrated by Figs. 2.4 (e) and 2.4 (f). The effect of this transformation is to expand or contract length along the coordinate axes so that the metric ellipse is deformed into a unit circle.

Among three components of eigenspace, eigenvalues of matrix \mathbf{E}''_l with unit metric $\mathbf{A}''_l = \mathbf{I}$, are equal to the eigenvalues of \mathbf{E}_l with associated metric \mathbf{A}_l in (2.33), respectively [Aravind, 1988]. However, orientation parameters in two cases are different. There is relation between two orientation parameters by

$$\tan \Theta = \frac{\sqrt{\det \mathbf{A}_l}}{A_{11} + A_{12} \tan \Psi} \tan \Psi \quad (2.40)$$

where the orientation parameter of the maximum principal axis of the strain matrix \mathbf{E}_l with corresponding metric \mathbf{A}_l is considered by Ψ , while the orientation parameter of the matrix \mathbf{E}''_l with corresponding unit metric is considered by Θ (see Fig. 2.5).

Hence, without loss of generality, by means of Eqs. (2.39) and (2.40), we are able to have mapping from eigenspectra components of $\{\mathbf{E}_l, \mathbf{A}_l\}$, Eq. (2.33), onto eigenspectra components of $\{\mathbf{E}''_l, \mathbf{I}\}$. Namely

$$\begin{bmatrix} \Lambda_1 \\ \Lambda_2 \\ \Theta \end{bmatrix} = \frac{1}{2} \begin{bmatrix} E''_{11} + E''_{22} + \sqrt{(E''_{11} - E''_{22})^2 + 4E''_{12}{}^2} \\ E''_{11} + E''_{22} - \sqrt{(E''_{11} - E''_{22})^2 + 4E''_{12}{}^2} \\ \arctan \frac{2E''_{12}}{E''_{11} - E''_{22}} \end{bmatrix} = \frac{1}{2} \begin{bmatrix} \text{tr}(\mathbf{E}_l\mathbf{A}_l^{-1}) + \sqrt{(\text{tr}(\mathbf{E}_l\mathbf{A}_l^{-1}))^2 - 4\det(\mathbf{E}_l\mathbf{A}_l^{-1})} \\ \text{tr}(\mathbf{E}_l\mathbf{A}_l^{-1}) - \sqrt{(\text{tr}(\mathbf{E}_l\mathbf{A}_l^{-1}))^2 - 4\det(\mathbf{E}_l\mathbf{A}_l^{-1})} \\ \arctan\left(\frac{\sqrt{\det \mathbf{A}_l}}{A_{11} + A_{12} \tan \Psi} \tan \Psi\right) \end{bmatrix} \quad (2.41)$$

Similar type of procedures can be carried out as simultaneous diagonalization of the right pair of matrices $\{\mathbf{E}_r, \mathbf{A}_r\}$, in order to convert metric matrix into unit matrix.

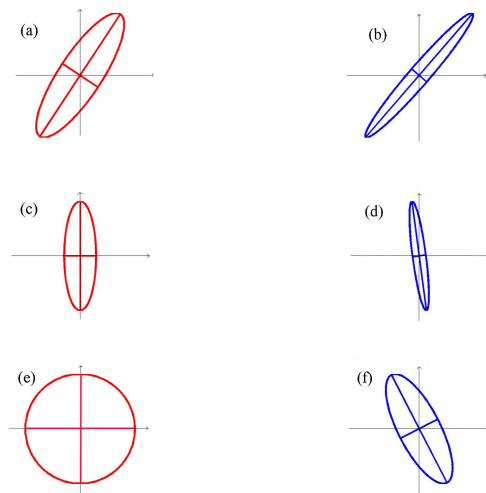


Figure 2.4: Geometrical representation of simultaneous diagonalization of matrices $\{\mathbf{E}_l, \mathbf{A}_l\}$. The left side is related to the geometrical representation of left metric, which is symmetric and positive definite. Then it can be presented by an ellipse. The right side is related to matrix form of left Euler-Lagrange strain tensor, which is symmetric. Illustration of it can be an ellipse or hyperbola, however we chose to present it as an ellipse.

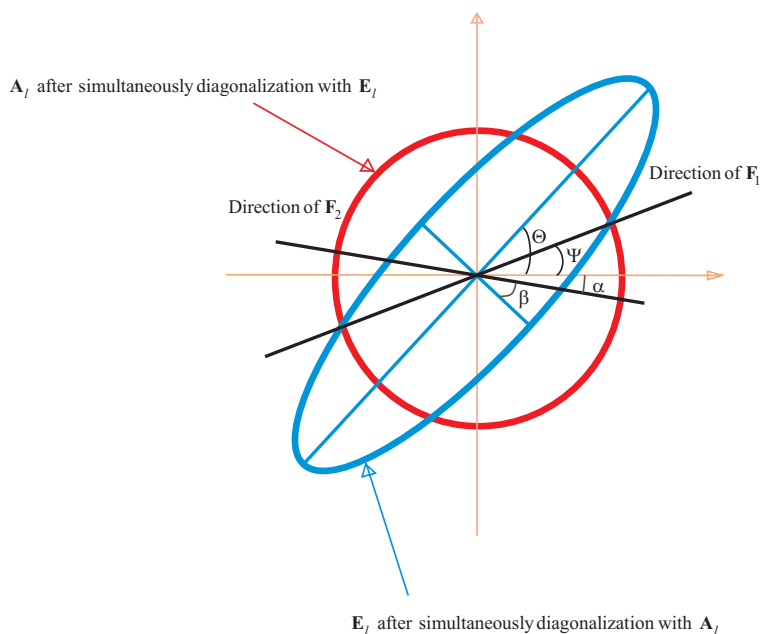


Figure 2.5: Illustrates the orientation of major eigenvector of left Euler-Lagrange strain tensor on surface M_l^2 by Ψ , and on plane by Θ .

Remark 2.2 This problem arises in the study of map projections, when one intends to learn about the distortion of mapping from one surface onto another surface. In particular, Tissot [1881] published an analysis of the distortion that occurs on map projections. He devised *Tissot's Indicatrix*, or the distortion circle, which when plotted on a map will appear as an ellipse whose elongation depends on the amount of distortion by the map at that point. The angle and extent of the elongation represents the amount of angular distortion of the map. The size of the ellipse indicates the amount that the area is distorted.

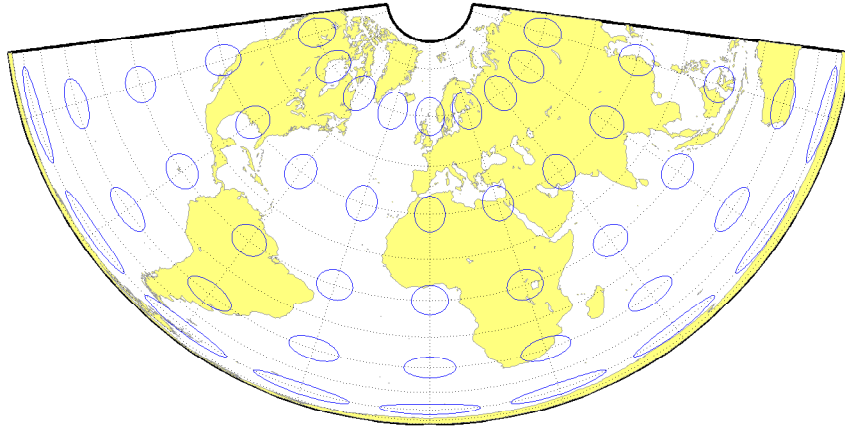


Figure 2.6: Albers conical equal area on a reference ellipsoid with coastlines and Tissot ellipses of distortions. The projection is free of distortion along the standard parallels. Distortion is constant along any other parallel. This projection is neither conformal nor equidistant.

When the Tissot's indicatrix reduces to a circle it means that, at that particular point, the scale is independent of direction. In conformal projections, where angles are preserved around every location, the Tissot's indicatrix are all circles, with varying sizes. In equal-area projections, where area proportions between objects are conserved, the Tissot's indicatrix have all unit area, although their shapes and orientations vary with location.

2.5 Comparison of Second Fundamental Forms

In deformation analysis the second fundamental form (SFF) is a symmetric bilinear form defined on the differentiable surfaces \mathbb{M}_l^2 and \mathbb{M}_r^2 , which in some sense measure the curvatures of \mathbb{M}_l^2 and \mathbb{M}_r^2 in embedding spaces, respectively. Meanwhile, the construction of the SFF of surfaces, requires a small digression. Afterwards we will discuss how they relate to the curvatures of \mathbb{M}_l^2 and \mathbb{M}_r^2 .

We suppose that surfaces \mathbb{M}_l^2 and \mathbb{M}_r^2 which are governed by $\mathbf{X} = \mathbf{X}(\Theta^1, \Theta^2)$ and $\mathbf{x} = \mathbf{x}(\theta^1, \theta^2)$, are surfaces of class $C^m (m \geq 2)$. Then for each surface point exist associated unit normal vectors \mathbf{A}_3

and \mathbf{a}_3 , with differentials $d\mathbf{A}_3 = \mathbf{A}_{3,1}d\Theta^1 + \mathbf{A}_{3,2}d\Theta^2$ and $d\mathbf{a}_3 = \mathbf{a}_{3,1}d\theta^1 + \mathbf{a}_{3,2}d\theta^2$, separately. Here, vectors $\mathbf{A}_{3,1}$, $\mathbf{A}_{3,2}$ and $\mathbf{a}_{3,1}$, $\mathbf{a}_{3,2}$ denote to first-order partial derivatives of unit normal vectors with respect to curvilinear coordinates $\{\Theta^1, \Theta^2\}$ and $\{\theta^1, \theta^2\}$ respectively.

Differential forms of unit normal vectors $d\mathbf{A}_3$ and $d\mathbf{a}_3$ are separately orthogonal over the unit normal vectors \mathbf{A}_3 and \mathbf{a}_3 , likewise they are parallel to tangent plane of the surfaces \mathbb{M}_7^2 and \mathbb{M}_7^2 . Now, we consider the quantities

$$\Pi(\Theta^1, \Theta^2) =: - \langle d\mathbf{X}, d\mathbf{A}_3 \rangle \quad \text{vs.} \quad \Pi(\theta^1, \theta^2) =: - \langle d\mathbf{x}, d\mathbf{a}_3 \rangle$$

By using Eq. (2.3), we obtain

$$\begin{aligned} \Pi(\Theta^1, \Theta^2) &= - \langle \mathbf{A}_1 d\Theta^1 + \mathbf{A}_2 d\Theta^2, \mathbf{A}_{3,1} d\Theta^1 + \mathbf{A}_{3,2} d\Theta^2 \rangle \\ &\quad \text{vs.} \\ \Pi(\theta^1, \theta^2) &= - \langle \mathbf{a}_1 d\theta^1 + \mathbf{a}_2 d\theta^2, \mathbf{a}_{3,1} d\theta^1 + \mathbf{a}_{3,2} d\theta^2 \rangle \end{aligned}$$

According to this definitions, the SFF captures second derivative information. It can be computed easily from Eq. (2.42) that

$$\Pi(\Theta^1, \Theta^2) = L(d\Theta^1)^2 + 2M(d\Theta^1)(d\Theta^2) + N(d\Theta^2)^2 \quad \text{vs.} \quad \Pi(\theta^1, \theta^2) = l(d\theta^1)^2 + 2m(d\theta^1)(d\theta^2) + n(d\theta^2)^2 \quad (2.42)$$

where

$$\begin{aligned} L &= - \langle \mathbf{A}_1, \mathbf{A}_{3,1} \rangle \quad \text{vs.} \quad l = - \langle \mathbf{a}_1, \mathbf{a}_{3,1} \rangle \\ M &= -\frac{1}{2}(\langle \mathbf{A}_1, \mathbf{A}_{3,2} \rangle + \langle \mathbf{A}_2, \mathbf{A}_{3,1} \rangle) \quad \text{vs.} \quad m = -\frac{1}{2}(\langle \mathbf{a}_1, \mathbf{a}_{3,2} \rangle + \langle \mathbf{a}_2, \mathbf{a}_{3,1} \rangle) \\ N &= - \langle \mathbf{A}_2, \mathbf{A}_{3,2} \rangle \quad \text{vs.} \quad n = - \langle \mathbf{a}_2, \mathbf{a}_{3,2} \rangle \end{aligned} \quad (2.43)$$

Left and right hand sides of the Eq. (2.43) are called SFF of corresponding surfaces \mathbb{M}_7^2 and \mathbb{M}_7^2 at coordinates $\{\Theta^1, \Theta^2\}$ and $\{\theta^1, \theta^2\}$, respectively. Since $\langle \mathbf{A}_1, \mathbf{A}_3 \rangle = 0$ and $\langle \mathbf{A}_2, \mathbf{A}_3 \rangle = 0$, as well as $\langle \mathbf{a}_1, \mathbf{a}_3 \rangle = 0$ and $\langle \mathbf{a}_2, \mathbf{a}_3 \rangle = 0$, it can be shown that [Prakash, 1981]

$$\langle \mathbf{A}_3, \mathbf{A}_{\Phi, \Lambda} \rangle = - \langle \mathbf{A}_{3, \Phi}, \mathbf{A}_\Lambda \rangle \quad \text{vs.} \quad \langle \mathbf{a}_3, \mathbf{a}_{\phi, \lambda} \rangle = - \langle \mathbf{a}_{3, \phi}, \mathbf{a}_\lambda \rangle$$

These give alternative expressions for L , M , N and l , m , n . Namely from (2.43)

$$\begin{aligned} L &= \langle \mathbf{A}_{1,1}, \mathbf{A}_3 \rangle \quad \text{vs.} \quad l = \langle \mathbf{a}_{1,1}, \mathbf{a}_3 \rangle \\ M &= \langle \mathbf{A}_{1,2}, \mathbf{A}_3 \rangle \quad \text{vs.} \quad m = \langle \mathbf{a}_{1,2}, \mathbf{a}_3 \rangle \\ N &= \langle \mathbf{A}_{2,2}, \mathbf{A}_3 \rangle \quad \text{vs.} \quad n = \langle \mathbf{a}_{2,2}, \mathbf{a}_3 \rangle \end{aligned}$$

Compare with the tensor notation

$$\Pi(\Theta^1, \Theta^2) = B_{\Lambda\Phi} d\Theta^\Lambda d\Theta^\Phi \quad \text{vs.} \quad \Pi(\theta^1, \theta^2) = b_{\lambda\phi} d\theta^\lambda d\theta^\phi \quad (2.44)$$

where coefficients $B_{\Lambda\Phi}$ and $b_{\lambda\phi}$ are coordinates of the surface symmetric tensor and given by

$$\mathbf{B}_l := [B_{\Lambda\Phi}] = \begin{bmatrix} B_{11} & B_{12} \\ B_{21} & B_{22} \end{bmatrix} = \begin{bmatrix} L & M \\ M & N \end{bmatrix} \quad \text{vs.} \quad \mathbf{B}_r := [b_{\lambda\phi}] = \begin{bmatrix} b_{11} & b_{12} \\ b_{21} & b_{22} \end{bmatrix} = \begin{bmatrix} l & m \\ m & n \end{bmatrix}$$

which is comparable to Eq. (2.7). The SFF is *invariant* under a coordinate transformation in the same sense that the FFF is invariant. It should be noted that the SFF remains invariant as long as the coordinate transformation preserves the direction of unit normal vector, otherwise the SFF changes its sign.

2.5.1 Mean and Gaussian Curvatures

For a M_l^2 surface embedded in \mathbb{E}^3 , we consider the intersection of the surface with a plane containing the normal vector and one of the tangent vectors at a particular point. This intersection is a plane curve and has a curvature. This is the normal curvature, and it varies with the choice of the tangent vector, which is illustrated by Fig. (2.7). The maximum and minimum values of the normal curvature at a point are called the *principal curvatures*, κ_2 and κ_1 . The directions of the corresponding tangent vectors are always perpendicular, and are therefore called *principal directions*.

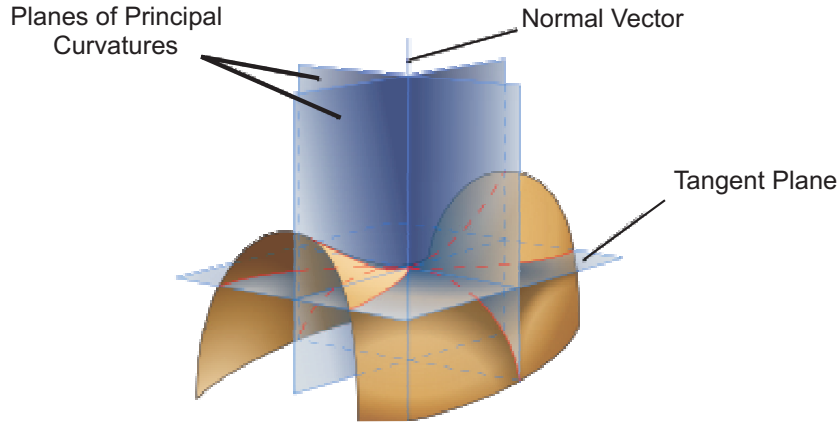


Figure 2.7: Surface with normal planes in directions of principal curvatures.

The principal curvatures measure the maximum and minimum bending of a surface at each point. The *Gaussian curvature* K and *mean curvature* H are related to κ_1 and κ_2 by [Gray, 1997, pages:363-367]

$$K = \kappa_1\kappa_2 = \frac{LN - M^2}{EG - F^2} = \frac{\det[\mathbf{B}_l]}{\det[\mathbf{A}_l]} := \frac{\det[B_{\Lambda\Phi}]}{\det[A_{\Lambda\Phi}]} \quad (2.45)$$

$$H = \frac{1}{2}(\kappa_1 + \kappa_2) = \frac{EN - 2FM + GL}{2(EG - F^2)} = \frac{1}{2}(B_{\Lambda\Phi} A^{\Lambda\Phi}) \quad (2.46)$$

This can be written as a quadratic equation

$$\kappa^2 - 2H\kappa + K = 0 \quad (2.47)$$

which has solutions

$$\kappa_1 = H + \sqrt{H^2 - K}$$

$$\kappa_2 = H - \sqrt{H^2 - K}$$

The metric tensor is positive-definite $EG - F^2 > 0$, then in Eq. (2.45) the sign of K agrees with the sign of $LN - M^2$. In the same manner, in Eq. (2.46) sign of H agrees with the sign of $EN - 2FM + GL$. Here we adopt the convention that a curvature is taken to be positive if the curve turns in the same direction as the surface's chosen normal, otherwise negative. Furthermore, surface points can be labeled as belonging to a viewpoint independent surface shape class type based on the combination of the signs from the Gaussian and mean curvatures [Koenderink and Lisowski, 1992], as shown in Tab. (2.2) and Fig. 2.8.

These curvatures are independent of the parametrization used, and are important tools for analyzing the surface. A wide range of their applications can be found in engineering subjects (e.g. in shell theory, image processing, computer vision, etc). A very nice application of mean and Gaussian curvature in studying the structure of Earth's mantle and crust is given by Bursa and Pec [1993].

Table 2.2: Shape classification based on the signs of mean and Gaussian curvatures.

	$K < 0$	$K = 0$	$K > 0$
$H < 0$	Saddle Valley	Concave(Cylinder)	Concave(Ellipsoid)
$H = 0$	Minimal	Plane	Impossible
$H > 0$	Saddle Ridge	Convex(Cylinder)	Convex(Ellipsoid)

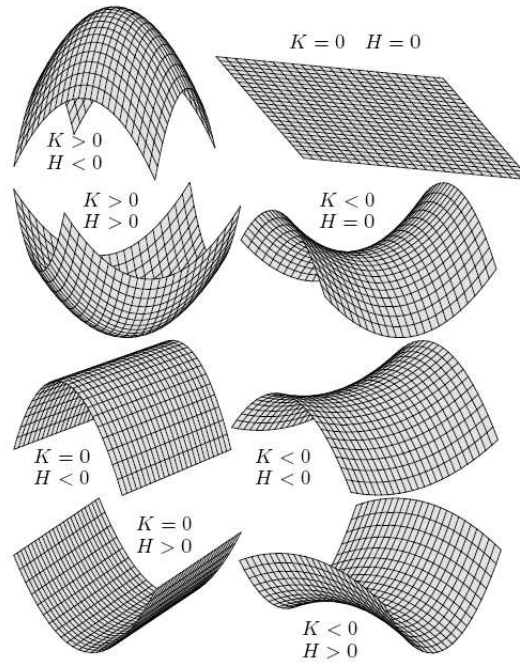


Figure 2.8: Eight basic visible-invariant surface types. The surfaces are oriented by their upward normals.

Finally, comparing the left and right mean and Gaussian curvatures, yields

$$K = \frac{LN - M^2}{EG - F^2} = \frac{\det[\mathbf{B}_l]}{\det[\mathbf{A}_l]} := \frac{\det[B_{\Lambda\Phi}]}{\det[A_{\Lambda\Phi}]} \quad \text{vs.} \quad k = \frac{ln - m^2}{eg - f^2} = \frac{\det[\mathbf{B}_r]}{\det[\mathbf{A}_r]} := \frac{\det[b_{\lambda\phi}]}{\det[a_{\lambda\phi}]} \quad (2.48)$$

$$H = \frac{EN - 2FM + GL}{2(EG - F^2)} = \frac{1}{2}(B_{\Lambda\Phi}A^{\Lambda\Phi}) \quad \text{vs.} \quad h = \frac{en - 2fm + gl}{2(eg - f^2)} = \frac{1}{2}(b_{\lambda\phi}a^{\lambda\phi})$$

2.6 Tensor of Changes of Curvature (TCC): deformation tensor of second kind

Establishing a comparison between left- and right hand sides of the Eq. (2.42), measures the deformation based upon differences between SFF of surfaces \mathbb{M}_l^2 and \mathbb{M}_r^2 , namely $\Pi(\theta^1, \theta^2) - \Pi(\Theta^1, \Theta^2)$, which implies a curvature change due to the deformation. Hence, according to (2.44) we have

$$\Pi(\theta^1, \theta^2) - \Pi(\Theta^1, \Theta^2) = K_{\Phi\Lambda}d\Theta^\Lambda d\Theta^\Phi = k_{\phi\lambda}d\theta^\lambda d\theta^\phi \quad (2.49)$$

where

$$K_{\Lambda\Phi} = K_{\Phi\Lambda} := b_{\lambda\phi} \frac{\partial\theta^\lambda}{\partial\Theta^\Lambda} \frac{\partial\theta^\phi}{\partial\Theta^\Phi} - B_{\Lambda\Phi} \quad \text{vs.} \quad k_{\lambda\phi} = k_{\phi\lambda} := b_{\lambda\phi} - B_{\Lambda\Phi} \frac{\partial\Theta^\Lambda}{\partial\theta^\lambda} \frac{\partial\Theta^\Phi}{\partial\theta^\phi} \quad (2.50)$$

are respectively called *Lagrangian and Eulerian portrait of tensor of changes of curvatures* (TCC). Following the map projection conventions, they are called *left Euler-Lagrange deformation of second kind* and *right Euler-Lagrange deformation of second kind*, respectively. The matrix representation of them are given by

$$\mathbf{K}_l := [K_{\Lambda\Phi}] \quad \text{vs.} \quad \mathbf{K}_r := [k_{\lambda\phi}]$$

Correspondent to Eq. (2.22), it is more adequate to express TCC as set a of functions of the displacement vector. Similar relations could be formulated for the TCC, but they are more complicated [Ernst, 1981]. We can overcome this problem by using a *difference vector of unit normal vectors* \mathbf{w} in addition to the displacement vector [Stein, 1980]. The vector \mathbf{w} is defined as the difference of a unit normal vector on a material point (located at the undeformed surface) \mathbb{M}_l^2 and a unit normal vector on the same material point (located at the deformed surface) \mathbb{M}_r^2 . Thus

$$\mathbf{w} = \mathbf{a}_3 - \mathbf{A}_3 \quad (2.51)$$

which is illustrated by Fig. 2.9. Similar to the displacement vector, difference vector of unit normal vectors \mathbf{w} will have surface components \tilde{W}^K referred to the curvilinear coordinate system $\{\Theta^1, \Theta^1\}$ and \tilde{w}^k referred to the $\{\theta^1, \theta^1\}$ given by

$$\mathbf{w} = \tilde{W}^K \mathbf{A}_K = \tilde{W}_K \mathbf{A}^K \quad \text{vs.} \quad \mathbf{w} = \tilde{w}^k \mathbf{a}_k = \tilde{w}_k \mathbf{a}^k \quad (2.52)$$

or

$$\mathbf{w} = \tilde{W}^\Phi \mathbf{A}_\Phi + \tilde{W}^3 \mathbf{A}_3 = \tilde{W}_\Phi \mathbf{A}^\Phi + \tilde{W}_3 \mathbf{A}^3 \quad \text{vs.} \quad \mathbf{w} = \tilde{w}^\phi \mathbf{a}_\phi + \tilde{w}^3 \mathbf{a}_3 = \tilde{w}_\phi \mathbf{a}^\phi + \tilde{w}_3 \mathbf{a}^3$$

Hence, performing scalar products of (2.52) with \mathbf{A}^K and \mathbf{a}^k , respectively, define

$$\tilde{W}^K = \langle \mathbf{w}, \mathbf{A}^K \rangle \quad \text{vs.} \quad \tilde{w}^k = \langle \mathbf{w}, \mathbf{a}^k \rangle$$

or under scalar multiplication of (2.52) by \mathbf{A}_K and \mathbf{a}_k , separately, we obtain

$$\tilde{W}_K = \langle \mathbf{w}, \mathbf{A}_K \rangle \quad \text{vs.} \quad \tilde{w}_k = \langle \mathbf{w}, \mathbf{a}_k \rangle$$

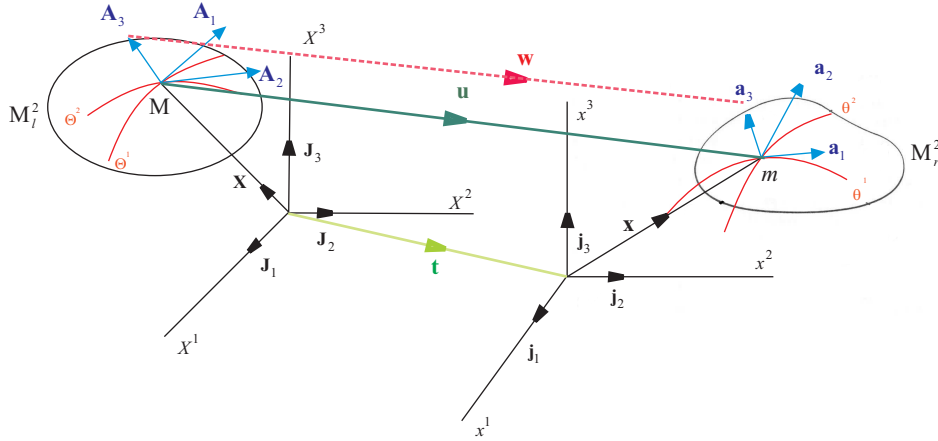


Figure 2.9: Difference of unit normal vectors \mathbf{w} which is illustrated by dashed line.

Similar to Eq. (2.22), the expression of Eq. (2.49) as a function of displacement vector can be described by [Sansour et al., 1997; Voosoghi, 2000]

$$K_{\Lambda\Phi} = - \langle \mathbf{w}_{,\Lambda}, \mathbf{A}_\Phi \rangle - \langle \mathbf{w}_{,\Lambda}, \mathbf{u}_{,\Phi} \rangle - \langle \mathbf{u}_{,\Phi}, \mathbf{A}_{3,\Lambda} \rangle \quad \text{vs.} \quad k_{\lambda\phi} = - \langle \mathbf{w}_{,\lambda}, \mathbf{a}_\phi \rangle - \langle \mathbf{w}_{,\lambda}, \mathbf{u}_{,\phi} \rangle - \langle \mathbf{u}_{,\phi}, \mathbf{a}_{3,\lambda} \rangle \quad (2.53)$$

where

$$\mathbf{w}_{,\Lambda} = \frac{\partial \mathbf{w}}{\partial \Theta^\Lambda} \quad \text{vs.} \quad \mathbf{w}_{,\lambda} = \frac{\partial \mathbf{w}}{\partial \theta^\lambda}$$

are first-order partial derivatives of \mathbf{w} with respect to the material and spatial curvilinear coordinates (see Appendix A).

2.6.1 An Analytical Example

In reference to example (2.4.1), which deals with the determination of the TCC, from the embedding of an ellipsoid-of-revolution as a representation of the Earth's surface before deformation, namely by Eq. (2.24), and considers the representation of the Earth's surface after deformation by Eq. (2.25). In example (2.4.1) the tangent basis vectors, $\{\mathbf{A}_1, \mathbf{A}_2\}$ and $\{\mathbf{a}_1, \mathbf{a}_2\}$, through Eqs. (2.3) were determined. Using Eq. (2.4) we can demonstrate unit normal vectors \mathbf{A}_3 and \mathbf{a}_3 , namely

$$\mathbf{A}_1 = \begin{bmatrix} \cos \Phi (H_{,\Lambda} \cos \Lambda - (N + H) \sin \Lambda) \\ \cos \Phi (H_{,\Lambda} \sin \Lambda + (N + H) \cos \Lambda) \\ \sin \Phi H_{,\Lambda} \end{bmatrix} \quad \text{vs.} \quad \mathbf{a}_1 = \begin{bmatrix} \cos \phi (h_{,\lambda} \cos \lambda - (n + h) \sin \lambda) \\ \cos \phi (h_{,\lambda} \sin \lambda + (n + h) \cos \lambda) \\ \sin \phi h_{,\lambda} \end{bmatrix} \quad (2.54)$$

$$\mathbf{A}_2 = \begin{bmatrix} \cos \Lambda(H_{,\Phi} \cos \Phi - (M + H) \sin \Phi) \\ \sin \Lambda(H_{,\Phi} \cos \Phi - (M + H) \sin \Phi) \\ H_{,\Phi} \sin \Phi + (M + H) \cos \Phi \end{bmatrix} \quad \text{vs.} \quad \mathbf{a}_2 = \begin{bmatrix} \cos \lambda(h_{,\phi} \cos \phi - (m + h) \sin \phi) \\ \sin \lambda(h_{,\phi} \cos \phi - (m + h) \sin \phi) \\ h_{,\phi} \sin \phi + (m + h) \cos \phi \end{bmatrix} \quad (2.55)$$

Then unit normal vectors can be obtained by

$$\mathbf{A}_3 = \frac{\mathbf{A}_1 \times \mathbf{A}_2}{\|\mathbf{A}_1 \times \mathbf{A}_2\|} \quad \text{vs.} \quad \mathbf{a}_3 = \frac{\mathbf{a}_1 \times \mathbf{a}_2}{\|\mathbf{a}_1 \times \mathbf{a}_2\|}$$

The Cartesian coordinates of \mathbf{A}_3 and \mathbf{a}_3 can be determined in terms of geodetic longitudes and latitudes of the points, at the left and right surfaces, respectively [Voosoghi, 2000; Grafarend and Voosoghi, 2003]

$$\mathbf{A}_3 = \frac{1}{\sqrt{\det(\mathbf{A}_l)}} \begin{bmatrix} (\sin \Lambda(M + H)H_{,\Lambda} + \cos \Phi \cos \Lambda(N + H)(\sin \Phi H_{,\Phi} + \cos \Phi(M + H))) \\ \cos \Phi \sin \Lambda(N + H)(\sin \Phi H_{,\Phi} + \cos \Phi(M + H)) - \cos \Lambda(M + H)H_{,\Lambda} \\ \cos \Phi(N + H)(\sin \Phi(M + H) - H_{,\Phi} \cos \Phi) \end{bmatrix} \quad (2.56)$$

versus

$$\mathbf{a}_3 = \frac{1}{\sqrt{\det(\mathbf{A}_r)}} \begin{bmatrix} (\sin \lambda(m + h)h_{,\lambda} + \cos \phi \cos \lambda(n + h)(\sin \phi h_{,\phi} + \cos \phi(m + h))) \\ \cos \phi \sin \lambda(n + h)(\sin \phi h_{,\phi} + \cos \phi(m + h)) - \cos \Lambda(m + h)h_{,\lambda} \\ \cos \phi(n + h)(\sin \phi(m + h) - h_{,\phi} \cos \phi) \end{bmatrix} \quad (2.57)$$

Using (2.51), we can compute the difference vector of unit normal vectors \mathbf{w} . Hence, by having \mathbf{w} and using Eq. (2.50) we compute the left and right TCC [Sansour et al., 1997; Voosoghi, 2000; Pietraszkiewicz and Szwabowicz, 2007], namely

$$K_{\Lambda\Phi} = b_{\lambda\phi} \frac{\partial\theta^\lambda}{\partial\Theta^\Lambda} \frac{\partial\theta^\phi}{\partial\Theta^\Phi} - B_{\Lambda\Phi} \quad \text{vs.} \quad k_{\lambda\phi} = b_{\lambda\phi} - B_{\Lambda\Phi} \frac{\partial\Theta^\Lambda}{\partial\theta^\lambda} \frac{\partial\Theta^\Phi}{\partial\theta^\phi} \quad (2.58)$$

where

$$B_{\Lambda\Phi} = - \left\langle \frac{\partial\mathbf{A}_3}{\partial\Theta^\Lambda}, \mathbf{A}_\Phi \right\rangle \quad \text{vs.} \quad b_{\lambda\phi} = - \left\langle \frac{\partial\mathbf{a}_3}{\partial\theta^\lambda}, \mathbf{a}_\phi \right\rangle \quad (2.59)$$

Eq. (2.59) is the so-called *Weingarten* equation, for which analytical proof is given in Appendix A. Therefore, by inserting Eq. (2.59) into Eq. (2.58) we have

$$\begin{aligned} K_{\Lambda\Phi} &= - \frac{\partial\theta^\lambda}{\partial\Theta^\Lambda} \frac{\partial\theta^\phi}{\partial\Theta^\Phi} \left\langle \frac{\partial\mathbf{a}_3}{\partial\theta^\lambda}, \mathbf{a}_\phi \right\rangle - B_{\Lambda\Phi} \quad \text{vs.} \quad k_{\lambda\phi} = b_{\lambda\phi} + \frac{\partial\Theta^\Lambda}{\partial\theta^\lambda} \frac{\partial\Theta^\Phi}{\partial\theta^\phi} \left\langle \frac{\partial\mathbf{A}_3}{\partial\Theta^\Lambda}, \mathbf{A}_\Phi \right\rangle \\ K_{\Lambda\Phi} &= - \left\langle \frac{\partial(\mathbf{w} + \mathbf{A}_3)}{\partial\Theta^\Lambda}, \frac{\partial(\mathbf{X} + \mathbf{u})}{\partial\Theta^\Phi} \right\rangle - B_{\Lambda\Phi} \quad \text{vs.} \quad k_{\lambda\phi} = b_{\lambda\phi} - \left\langle \frac{\partial(\mathbf{w} - \mathbf{a}_3)}{\partial\Theta^\Lambda}, \frac{\partial(\mathbf{x} - \mathbf{u})}{\partial\theta^\phi} \right\rangle \end{aligned} \quad (2.60)$$

After some simple computations on Eq. (2.60) we can get

$$K_{\Lambda\Phi} = - \langle \mathbf{w}_{,\Lambda}, \mathbf{A}_\Phi \rangle - \langle \mathbf{w}_{,\Lambda}, \mathbf{u}_{,\Phi} \rangle - \langle \mathbf{u}_{,\Phi}, \mathbf{A}_{3,\Lambda} \rangle \quad \text{vs.} \quad k_{\lambda\phi} = - \langle \mathbf{w}_{,\lambda}, \mathbf{a}_\phi \rangle - \langle \mathbf{w}_{,\lambda}, \mathbf{u}_{,\phi} \rangle - \langle \mathbf{u}_{,\phi}, \mathbf{a}_{3,\lambda} \rangle \quad (2.61)$$

Hence, according to this example proof of Eq. (2.53) is completed.

2.6.2 Basis Vectors on Deformed Surface in Terms of Lagrangian Coordinates

Eqs. (2.56) and (2.57) are fundamental equations for the computations of TCC, which represent the unit normal vectors as functions of latitudes and longitudes in the left and right surfaces, respectively. The important restriction about Eq. (2.57) is that computations need the first-order partial derivatives of ellipsoidal height(after deformation), $h(\phi, \lambda)$ with respect to (ϕ, λ) , namely $h_{,\phi}$ and $h_{,\lambda}$. Hence, we shall need to have continuous function of ellipsoidal height in deformed surface \mathbb{M}_l^2 , which we have not. Ernst [1981] proposed equations based on which, we can compute the surface basis vectors on deformed surface $\{\mathbf{a}_1, \mathbf{a}_2, \mathbf{a}_3\}$ based upon basis vectors of undeformed surface $\{\mathbf{A}_1, \mathbf{A}_2, \mathbf{A}_3\}$ directly. Namely

$$\mathbf{a}_\lambda = \ell_{,\lambda}^\alpha \mathbf{A}_\alpha + \zeta_\lambda \mathbf{A}_3 \quad (2.62)$$

where the components of the surface tensors $\ell_{,\lambda}^\alpha$ and ζ_λ can be given in terms of contravariant components of displacement vector $\{\tilde{U}^1, \tilde{U}^2, \tilde{U}^3\}$ by

$$\zeta_\lambda = \tilde{U}_{,\lambda}^3 + B_{\lambda\vartheta} \tilde{U}^\vartheta = \tilde{U}_{,\lambda}^3 + B_\lambda^\vartheta \tilde{U}_\vartheta \quad (2.63)$$

$$\ell_{,\lambda}^\alpha = \delta_\lambda^\alpha + \tilde{U}_{,\lambda}^\alpha + \left\{ \begin{matrix} \alpha \\ \lambda\gamma \end{matrix} \right\} \tilde{U}^\gamma - B_\lambda^\alpha \tilde{U}^3 \quad (2.64)$$

Hence, unit normal vector \mathbf{a}_3 can be obtained by cross production of tangent basis vectors $\{\mathbf{a}_1, \mathbf{a}_2\}$

$$\mathbf{a}_3 = \frac{\mathbf{a}_1 \times \mathbf{a}_2}{\|\mathbf{a}_1 \times \mathbf{a}_2\|} = \frac{(\ell_{,\lambda}^\alpha \mathbf{A}_\alpha + \zeta_\lambda \mathbf{A}_3) \times (\ell_{,\lambda}^\beta \mathbf{A}_\beta + \zeta_\lambda \mathbf{A}_3)}{\|(\ell_{,\lambda}^\alpha \mathbf{A}_\alpha + \zeta_\lambda \mathbf{A}_3) \times (\ell_{,\lambda}^\beta \mathbf{A}_\beta + \zeta_\lambda \mathbf{A}_3)\|} \quad (2.65)$$

where the coefficient $\left\{ \begin{matrix} \alpha \\ \lambda\gamma \end{matrix} \right\}$ are so-called *Christoffel* symbols of the second kind. They are also known as *affine connections* [Weinberg, 1972, page 71] or *connection coefficients* [Minster et al., 1973, page 210]. A general descriptions of Christoffel symbols are presented in Appendix A, but more detailed information about application requirements can be find in Voosoghi [2000, chap. 4].

2.6.3 Eigenspace Analysis, TCC

In comparison to eigenspace analysis in strain tensor, which is mentioned in subsection 2.4.2, the general eigenvector-eigenvalue problem can also be applied to the pair of symmetric matrices $\{\mathbf{K}_l, \mathbf{A}_l\}$ or $\{\mathbf{K}_r, \mathbf{A}_r\}$, in order to obtain the eigenspace components of TCC. Let us consider the matrix forms of left TCC and its associated metric tensor, which are given by

$$\mathbf{K}_l = \begin{bmatrix} K_{11} & K_{12} \\ K_{12} & K_{22} \end{bmatrix} \quad \mathbf{A}_l = \begin{bmatrix} A_{11} & A_{12} \\ A_{12} & A_{22} \end{bmatrix}$$

where both matrices are symmetric. Finding the eigenspectra elements of matrices $\{\mathbf{K}_l, \mathbf{A}_l\}$ leads us to obtaining a general eigenvector-eigenvalue problem of the type

$$\mathbf{K}_l \mathbf{F}'_l = \mathbf{D}_{\Lambda'} \mathbf{A}_l \mathbf{F}'_l \quad (2.66)$$

where $\mathbf{F}_l = [\mathbf{F}'_1, \mathbf{F}'_2] \in \mathbb{R}^{2 \times 2}$ is the matrix of eigenvectors and $\mathbf{D}_{\Lambda'}$ is the diagonal matrix of eigenvalues, namely $\mathbf{D}_{\Lambda'} = \text{diag}[\Lambda'_1, \Lambda'_2]$. Using (2.66), eigenvalues and eigenvectors can be obtained by

$$\mathbf{K}_l \mathbf{F}'_l - \mathbf{D}_{\Lambda'} \mathbf{A}_l \mathbf{F}'_l = 0 \implies \det(\mathbf{K}_l - \mathbf{D}_{\Lambda'} \mathbf{A}_l) = 0 \quad (2.67)$$

Finding eigenvalues of the matrices $\{\mathbf{K}_l, \mathbf{A}_l\}$, by (2.67), through

$$\Lambda'_{1,2} = \frac{1}{2} \left\{ \text{tr}(\mathbf{K}_l \mathbf{A}_l^{-1}) \pm \sqrt{(\text{tr}(\mathbf{K}_l \mathbf{A}_l^{-1}))^2 - 4 \det(\mathbf{K}_l \mathbf{A}_l^{-1})} \right\}, \quad \Lambda'_1, \Lambda'_2 \in \mathbb{R} \quad (2.68)$$

where Λ'_1 and Λ'_2 are *change of the principal curvatures* [Hontani and Deguchi, 1997]. A deformation portrait when $\text{sign} \Lambda'_1 = \text{sign} \Lambda'_2$ will be an *ellipse* and will be a *hyperbola* if $\text{sign} \Lambda'_1 \neq \text{sign} \Lambda'_2$.

Inserting eigenvalues (2.68) into (2.66), we can obtain eigenvectors

$$\mathbf{F}'_1 = ((K_{22} - \Lambda'_1 A_{22})^2 A_{11} - 2(K_{12} - \Lambda'_1 A_{12})(K_{22} - \Lambda'_1 A_{22}) A_{12} + (K_{12} - \Lambda'_1 A_{12})^2 A_{22})^{-1/2} \begin{bmatrix} K_{22} - \Lambda'_1 A_{22} \\ -(K_{12} - \Lambda'_1 A_{12}) \end{bmatrix}$$

$$\mathbf{F}'_2 = ((K_{11} - \Lambda'_2 A_{11})^2 A_{22} - 2(K_{12} - \Lambda'_2 A_{12})(K_{11} - \Lambda'_2 A_{11}) A_{12} + (K_{12} - \Lambda'_2 A_{12})^2 A_{11})^{-1/2} \begin{bmatrix} -(K_{12} - \Lambda'_2 A_{12}) \\ K_{11} - \Lambda'_2 A_{11} \end{bmatrix}$$

where they can prescribe the *principal directions of curvature*. The orientation parameter can be obtained by

$$\Psi' = \arccos\left(\frac{\langle \mathbf{F}'_1, \mathbf{K}_l \rangle}{\|\mathbf{F}'_1\|}\right) = \arccos\left(\frac{F'_1}{\|\mathbf{F}'_1\|}\right) \quad \text{subject to} \quad \|\mathbf{F}'_1\|^2 = \max\{\|\mathbf{F}'_1\|, \|\mathbf{F}'_2\|\}, \quad \forall \Psi' \in \left[-\frac{\pi}{2}, \frac{\pi}{2}\right]$$

or

$$\Psi' = \arccos\left(\frac{\langle \mathbf{F}'_2, \mathbf{K}_l \rangle}{\|\mathbf{F}'_2\|}\right) = \arccos\left(\frac{F'_2}{\|\mathbf{F}'_2\|}\right) \quad \text{subject to} \quad \|\mathbf{F}'_2\|^2 = \max\{\|\mathbf{F}'_1\|, \|\mathbf{F}'_2\|\}, \quad \forall \Psi' \in \left[-\frac{\pi}{2}, \frac{\pi}{2}\right]$$

Hence, eigenspace components consists of

$$\mathbf{Y}' = \begin{bmatrix} \Lambda'_1 \\ \Lambda'_2 \\ \Psi' \end{bmatrix} = \frac{1}{2} \begin{bmatrix} \text{tr}(\mathbf{K}_l \mathbf{A}_l^{-1}) + \sqrt{(\text{tr}(\mathbf{K}_l \mathbf{A}_l^{-1}))^2 - 4 \det(\mathbf{K}_l \mathbf{A}_l^{-1})} \\ \text{tr}(\mathbf{K}_l \mathbf{A}_l^{-1}) - \sqrt{(\text{tr}(\mathbf{K}_l \mathbf{A}_l^{-1}))^2 - 4 \det(\mathbf{K}_l \mathbf{A}_l^{-1})} \\ 2 \arccos\left(\frac{\langle \mathbf{F}'_i, \mathbf{E}_i \rangle}{\|\mathbf{F}'_i\|}\right) \end{bmatrix}$$

A similar procedure can be performed for the right-pair of matrices $\{\mathbf{K}_r, \mathbf{A}_r\}$. Therefore, the right eigenspace components can be written as

$$\mathbf{y}' = \begin{bmatrix} \lambda'_1 \\ \lambda'_2 \\ \psi' \end{bmatrix} = \frac{1}{2} \begin{bmatrix} \text{tr}(\mathbf{K}_r \mathbf{A}_r^{-1}) + \sqrt{(\text{tr}(\mathbf{K}_r \mathbf{A}_r^{-1}))^2 - 4\det(\mathbf{K}_r \mathbf{A}_r^{-1})} \\ \text{tr}(\mathbf{K}_r \mathbf{A}_r^{-1}) - \sqrt{(\text{tr}(\mathbf{K}_r \mathbf{A}_r^{-1}))^2 - 4\det(\mathbf{K}_r \mathbf{A}_r^{-1})} \\ 2 \arccos\left(\frac{\langle \mathbf{f}'_i, \mathbf{e}_i \rangle}{\|\mathbf{f}'_i\|} \right) \end{bmatrix}$$

A mapping process from eigenspace components of $\{\mathbf{K}_l, \mathbf{A}_l\}$ and $\{\mathbf{K}_r, \mathbf{A}_r\}$ to eigenspace components in Euclidean space \mathbb{E}_l^2 and \mathbb{E}_r^2 , respectively, can be carried out, as described in Eq. (2.41). So we do not intend to repeat the procedure here.

2.7 Changes in Mean and Gaussian Curvatures

We calculated TCC, namely $K_{\Lambda\Phi}$ and $k_{\lambda\phi}$ in section 2.6. Hence, we can calculate the curvature tensor after deformation based on Eq. (2.50), and finally computing the changes of mean and Gaussian curvatures, which are introduced by Eq. (2.48), due to the deformation [Altiner, 1999; Voosoghi, 2000; Grafarend and Voosoghi, 2003] by

$$k - K = \frac{\det[b_{\lambda\phi}]}{\det[a_{\lambda\phi}]} - \frac{\det[B_{\Lambda\Phi}]}{\det[A_{\Lambda\Phi}]} = \frac{\det[B_{\Lambda\Phi} + K_{\Lambda\Phi}]}{\det[A_{\Lambda\Phi} + 2E_{\Lambda\Phi}]} - \frac{\det[B_{\Lambda\Phi}]}{\det[A_{\Lambda\Phi}]} \quad (2.69)$$

$$h - H = \frac{1}{2}(b_{\lambda\phi}a^{\lambda\phi}) - \frac{1}{2}(B_{\Lambda\Phi}A^{\Lambda\Phi}) = \frac{1}{2}((B_{\Lambda\Phi} + K_{\Lambda\Phi})(A_{\Lambda\Phi} + 2E_{\Lambda\Phi}) - \frac{1}{2}(B_{\Lambda\Phi}A^{\Lambda\Phi})) \quad (2.70)$$

Remark 2.3 In addition to the Euler-Lagrange deformation of second kind or TCC which is used to describe the changes in the curvature of the deforming body induced by the deformation, Tab. (2.3) collects the most common measures for deformation (based on SFF) and their definitions which appear in various applications in deformation analysis [Stein, 1980, page 511]

Table 2.3: Various measures for deformation (based on SFF).

Name	Symbol	Definitions
Left Euler – Lagrange strain tensor of second kind	\mathbf{K}_1	\mathbf{K}_l
Right Euler – Lagrange strain tensor of second kind	\mathbf{K}_2	\mathbf{K}_r
Difference vector of the unit normal vectors	\mathbf{K}_3	$\mathbf{a}_3 - \mathbf{A}_3$
Difference of mean curvatures	\mathbf{K}_4	$h - H$
Difference of Gaussian curvatures	\mathbf{K}_5	$k - K$
Difference of determinants of curvature tensors	\mathbf{K}_6	$\det(\mathbf{B}_r) - \det(\mathbf{B}_l)$

2.8 Numerical Examples

Here, to enhance our understanding of the capabilities of the proposed method which is presented in this chapter, we present two examples, one with a simulated data set and the other with a real data set.

2.8.1 Application Using Simulated Data

As mentioned in this chapter, we suppose that surfaces (before and after deformation) are both embedded in a 3D Euclidean space \mathbb{E}^3 . Here we *do not* consider 3D deformation field, and we define the simulated vertical displacement field *without horizontal displacements*, in particular, for the following two reasons

- i. To gain a closer understanding of the displacement field. Moreover, it allows an easy visualization and evaluation of how our method can detect deformation patterns.
- ii. Simplicity in comparing the 2D classical method, as due to the lack of horizontal components of the displacement field, the results of 2D classical methods are zero.

The simulated deformation field which is embedded in 3D Euclidean space \mathbb{E}^3 is illustrated in Fig. 2.10.

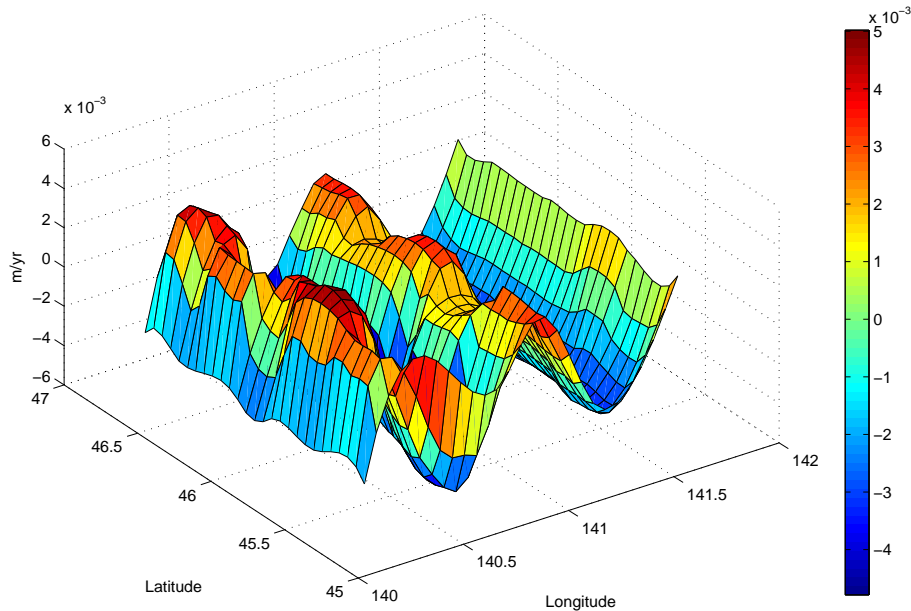


Figure 2.10: Rates of simulated vertical displacement field in units of $\text{m}\cdot\text{yr}^{-1}$. Note that, the values of simulated vertical deformation are not realistic to the selected geographical areas, we used these particular latitudes and longitudes just for governing a deformation field.

In this example, an area from $\text{N}45^\circ$ to $\text{N}47^\circ$ (latitude), and from $\text{E}140^\circ$ to $\text{E}142^\circ$ (longitude) is chosen as the test area just for generating a deformation field. We suppose that observation points are distributed in a regular grid over the selected latitude and longitude in resolution of, i.e., $17'$ regular grid points over the area. Hence, we follow the procedure of intrinsic approach in deformation analysis, using the main eleven steps:

step 1. Computing surface basis vectors $\{\mathbf{A}_1, \mathbf{A}_2, \mathbf{A}_3\}$ through Eqs. (2.54) and (2.55).

step 2. Conversion of the displacement vector \mathbf{u} to curvilinear components \tilde{U}^K and \tilde{U}_K , by Eqs. (2.20) and (2.21).

- step 3.** Use of two-dimensional finite element method (2D-FEM) in order to find approximate solutions of first-order partial derivatives of covariant and contravariant elements of displacement vector, namely \tilde{U}^K and \tilde{U}_K , with respect to ellipsoidal latitude and longitude (Φ, Λ) . The optimal finite element meshes can be generated by the *Delaunay* triangulation over the test area (see Fig. 2.11 (a)). Appendix B provides a quick reference to the 2D-FEM.
- step 4.** Obtaining curvature tensor, for left surface M_t^2 , through left side of Eq. (2.59) for every triangle.
- step 5.** Obtaining Lagrangian strain tensor, through left side of Eq. (2.27).
- step 6.** Getting the eigenvalues of Lagrangian strain tensor by Eq. (2.30), and computing the dilatation rates, through Eq. (2.35), which is illustrated by Fig. 2.11 (b).
- step 7.** Computing the difference vector of unit normal vectors \mathbf{w} , based on Eq. (2.65) and (2.51).
- step 8.** Conversion of the spatial difference vector of unit normal vectors \mathbf{w} with respect to curvilinear components \tilde{W}^K and \tilde{W}_K , by Eqs. (2.20) and (2.21).
- step 9.** Use of the 2D-FEM for finding approximate solutions of first-order partial derivatives of covariant and contravariant elements of \mathbf{w} , with respect to ellipsoidal latitude and longitude, namely $\tilde{W}_{,\Lambda}^K$ and $\tilde{W}_{K,\Lambda}$. Hence, similar to step 1, the optimal finite element meshes can be produced by the Delaunay triangulation over the test area.
- step 10.** Obtaining Lagrangian TCC, through left side of Eq. (2.61).
- step 11.** Computing changes in Gaussian and mean curvatures, through Eqs. (2.69) and (2.70) and finally illustration of them by Figs. 2.11 (c) and 2.11 (d).

Discussion of Results :

- i. The pattern of the dilatation rate is illustrated by Fig. 2.11(b). Positive dilatation corresponds to an increase in the occupied area (expansion), while negative dilatation corresponds to a decrease in the occupied area (compression). A comparison of this pattern with Fig. 2.10 shows the ability of the invariants of the surface strain tensor to uncover deformation features.
- ii. Fig. 2.11(c) shows the pattern of a change of mean curvature, due to deformation, in units of $10^{-7} \text{ m}^{-1}.\text{yr}^{-1}$. In this figure, positive values are associated to rising regions whereas negative values occur for sinking regions.
- iii. The pattern of change of Gaussian curvature is illustrated by Fig. 2.11(d), in units of $10^{-9} \text{ m}^{-2}.\text{yr}^{-1}$. A comparison of these results with Fig. 2.11(c) shows that, according to Tab. 2.2, we can have a shape-classification based upon a sign of mean and Gaussian curvatures. However, the difference in patterns of Gaussian and mean curvatures, reflects that the pattern of Gaussian curvature is so sensitive to height variations rather than mean curvature.

Through this example we could compare the exact pattern of the deformation field, which we have created, with various resulting strain tensor invariants, and patterns of changes in mean and Gaussian curvatures. Results show the ability of the patterns to uncover the upward and downward motions of the deformed surface. It seems to be that only one of the deformation measures, namely invariants of strain tensor or TCC, can not portray the deformation signals and must be considered together in order to perform a deformation analysis.

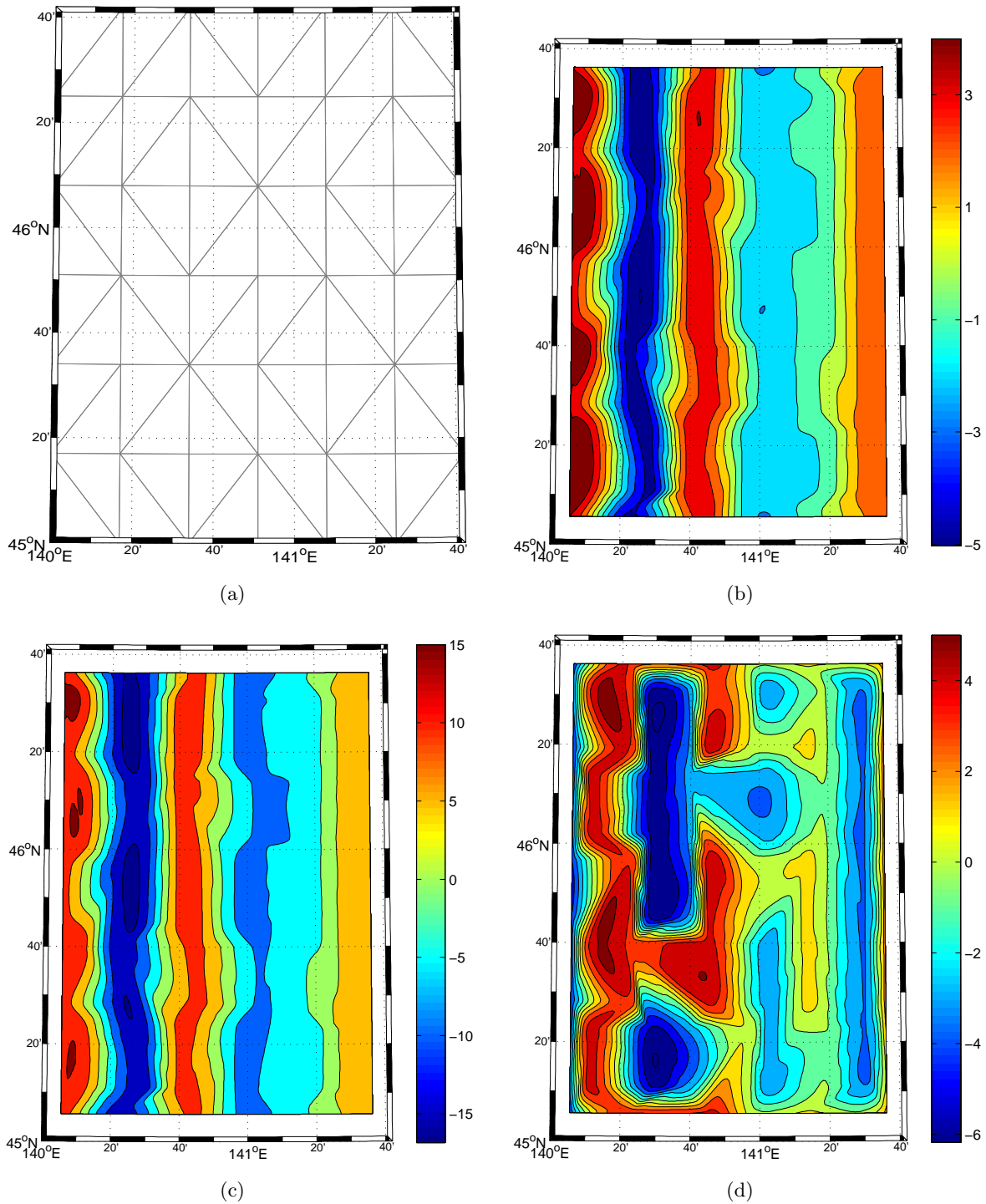


Figure 2.11: (a) Optimal Delaunay triangulation, (b) dilatation in units of yr^{-1} , (c) change of mean curvature in units of $10^{-7} \text{ m}^{-1} \cdot \text{yr}^{-1}$, (d) change of Gaussian curvature in units of $10^{-9} \text{ m}^{-2} \cdot \text{yr}^{-1}$ over the test area. Figures are illustrated in the Albers equal-area conic projection.

2.8.2 Application Using Real Data

This part has been dedicated to the application of the proposed model for deformation analysis, by a real data set. The study area chosen for this research is Southern California, an area with high seismic activities. Moreover, there exist also dense networks of GPS stations in order to monitor real-time crustal deformations.

Plate-tectonic setting of Southern California

Southern California is a region of high seismicity and widely distributed active faulting. The relative plate motion between the Pacific and North American cause a highly complex system of sub-parallel transform faults to accommodate the right lateral motion of 50 mm.yr^{-1} (see Fig. 2.12). A model of global plate motions ranges from 48 mm.yr^{-1} in terms of right lateral shear in Central California, namely parallel to the Central San Andreas Fault [Demets et al., 1987] to only 38 mm.yr^{-1} on or near San Andreas Fault. Another result of about 8 mm.yr^{-1} (15% of the relative plate motion) is documented by the 50-100 km wide Eastern California Shear Zone (ECSZ) which extends N35W from the eastern end of the Big Bend to the Owens Valley along a small circle about the Pacific-North American pole of rotation [Savage et al., 1990].

The Southern part of the ECSZ is the site of largest seismic events, which in recent years has hit Southern California strongest. The largest recent earthquakes occurred in the ECSZ of strength M_w 7.3 (Landers 1992), and M_w 7.1 (Hector Mine 1999). Both of them were right lateral strike-slip events in the direction of NNW, trending subvertical faults, close in space and time, especially in a region where earthquakes recur every thousand years. The Landers and Hector Mine earthquakes have indeed provided important data on post-seismic deformation. Viscoelastic models have been proposed to explain the post-seismic relaxations following the Landers [Pollitz et al., 2000] and Hector Mine [Politz et al., 2001] earthquakes. However, any extrapolation of the available post-seismic earthquake data does not suggest that the velocities in the Landers array will return to their pre-Landers values soon [Savage et al., 2003].

On January 17th in 1994, Northridge M_w 6.7 earthquake produced the largest ground motions in the Los Angeles region. The E-W striking sedimentary basin lies just south of the Western Transverse Ranges, a region influenced by the Big Bend in the north and characterized by E-W striking thrust faults, N-S shortening, and substantial uplift [Namson and Davis, 1998]. Unlike the most strike-slip earthquakes along the Northwest trending faults in ECSZ, the Northridge earthquake was a deep thrust-type event with a strike of 122° and a substantial up-dip component of slip [Wald et al., 1996]. However, Stein et al. [1994] investigated possible stress triggering of the Northridge event by previous earthquakes. Imperial Valley extends from the southern end of the San Andreas Fault (SAF) to the United States-Mexico border. It is one of the most seismically active portions of the Pacific -North American plate boundary.

On October 15th in 1979, a M_w 6.9 earthquake occurred in this region. A relatively fast moving fault of estimated average slip rate along the Imperial Fault ranges from $15\text{-}20 \text{ mm.yr}^{-1}$ based on shoreline deposits [Thomas and Rockwell, 1996] to $35\text{-}43 \text{ mm.yr}^{-1}$ based on conventional geodetic surveys [Bennett et al., 1996; Wdowinski et al., 2001] was documented. Geodetic investigations indicate that a rate of imperial Fault accommodates nearly 80% of the total plate motion between the North American and Pacific Plates. InSAR has also been used to land subsidence associated with geothermal fields in Imperial Valley [Massonnet et al., 1997]. Fig. 2.13 illustrates the seismicity map of Southern

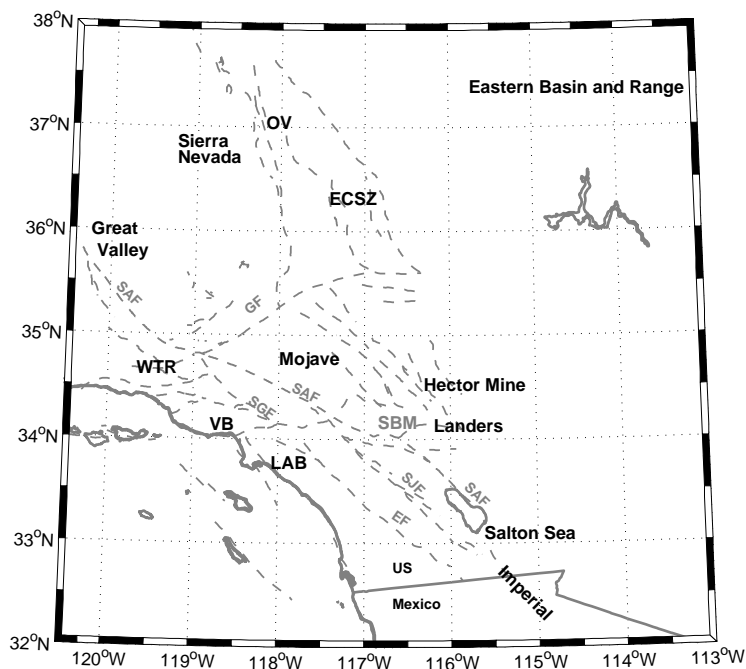


Figure 2.12: Southern California Fault summarizes: San Andreas Fault (SAF), the Garlock fault (GF), the San Jacinto fault, the San Gabriel fault (SGF), the Elsinore fault (EF). The mountain range extend from San Bernardino Mtns. Regions referenced in the text are the Eastern California Shear Zone (ECSZ), the Owens Valley (OV), the Western Transverse Ranges (WTR), the Ventura Basin (VB), the Los Angeles Basin (LAB). The figure is illustrated in Albers equal-area conic projection.

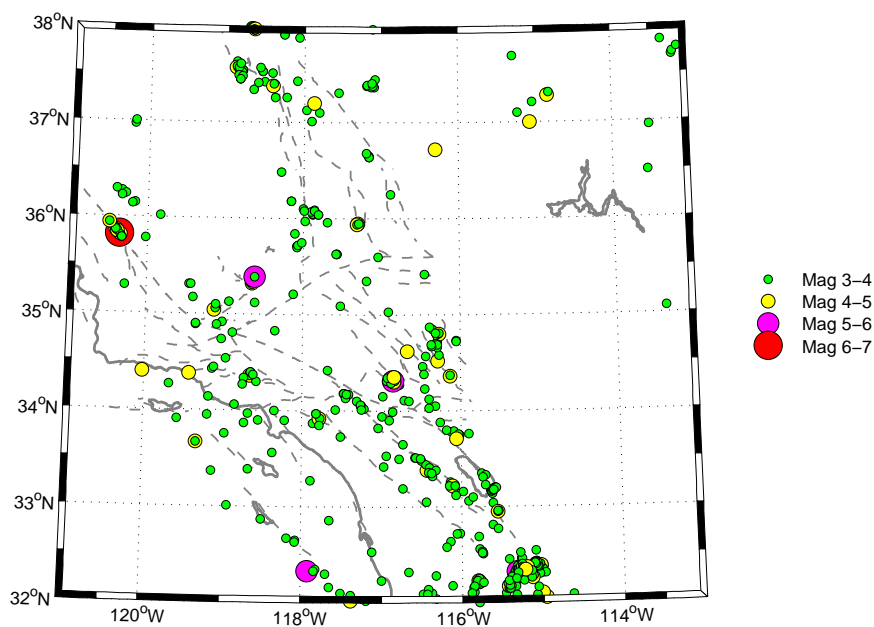


Figure 2.13: Southern California seismic events with $M_w \geq 3$ extracted from the *Southern California Earthquake Center* (January 2001 and January 2005) which are scaled by magnitude. The figure is illustrated in Albers equal-area conic projection.

California during the range of four years between January 2001 and January 2005, which can be obtained from the *Southern California Earthquake Center* (SCEC) (<http://www.scec.org>). This figure shows earthquakes with magnitude bigger than three.

GPS Arrays

GPS data are collected from *Scripps Orbit and Permanent Array Center* (SOPAC), which include archive high-precision GPS data particularly for the monitoring of earthquake hazards, tectonic plate motion, crustal deformation (<http://sopac.ucsd.edu/>).

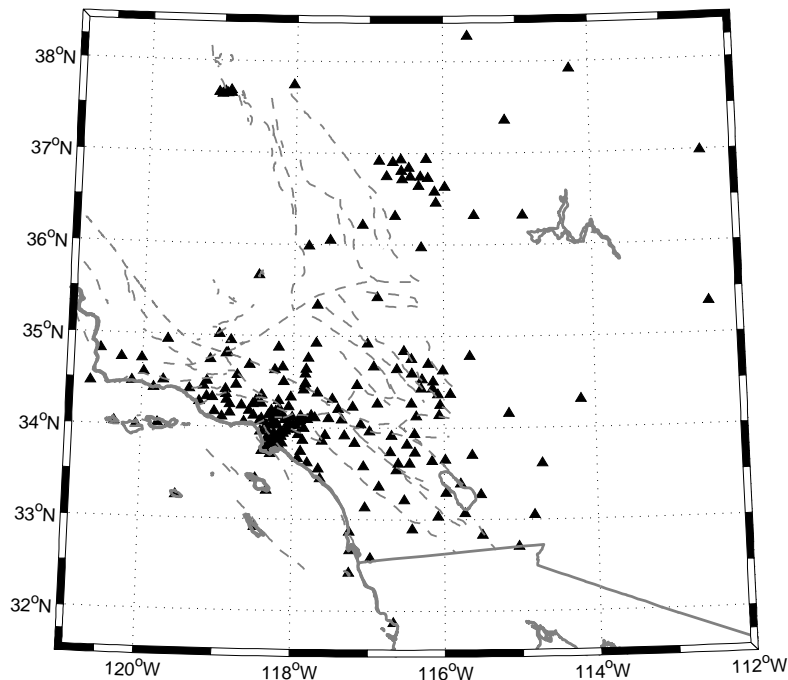


Figure 2.14: Sites of SOPAC network by individual solutions between 2001 and 2005. The figure is illustrated in Albers equal-area conic projection.

Given positions by SOPAC are provided in ITRF2000 and WGS84, and include both horizontal and vertical velocities and their accuracies. All the chosen stations have individual and continuous solutions up to 4 years, between January 2001 and January 2005 and take into account the linear velocity between those epochs. Fig. 2.14 illustrates the sites of SOPAC across Southern California. We have chosen a dense network of stations to get various surface deformation patterns of Southern California, which include 218 permanent GPS stations. The two factors are considered in the selection of the GPS points on the network :

- i. Average distance between the GPS points (distance between neighbor stations vary from 3 to 340 km), while the whole region should be covered by points of the network.
- ii. A sufficient period of time for modeling and removing offsets and seasonal effects from the GPS time series (specially in height component) and finally the detection of a deformation signal from

the measurements [Nikolaidis, 2002, page 16]. In the current network we have used four years GPS measurements (between January 2001 and January 2005).

Fig. 2.15 illustrates horizontal velocity rates across Southern California. The horizontal velocity field reaches a value of approximately $48 \text{ mm}\cdot\text{yr}^{-1}$ in terms of right lateral shear in the central and western part of California, roughly parallel to the central San Andreas Fault [Demets et al., 1987].

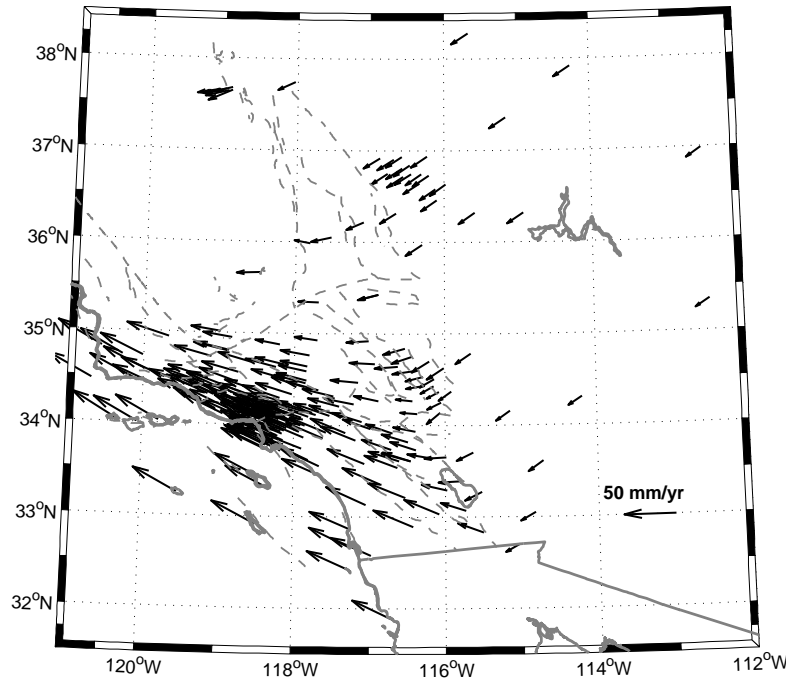


Figure 2.15: Horizontal velocity field in units of $\text{mm}\cdot\text{yr}^{-1}$ across Southern California. The figure is illustrated in Albers equal-area conic projection.

Horizontal velocity field are well documented in the Coast Ranges, namely larger than in the central parts. We have made an alternative, interpreting the Earth's discrete surface by adopting Fig. 2.16, which illustrates the rates of vertical crustal motion in Southern California. A maximum magnitude of the subsidence of the order $-10 \text{ mm}\cdot\text{yr}^{-1}$ is shown for the Los Angeles Basin area. Another land subsidence has been observed in Western Transverse Ranges, rather across the Coso Range and the North West of Salton Sea, (namely) due to the geothermal activity in those regions. Notable upward motions can be seen in the Landers and Hector Mine, probably due to post-seismic effects.

Results

Steps in computations in this subsection are similar to the steps we followed in subsection 2.8.1, except that the deformation field is inferred from the GPS observations. Assuming that a sufficient number of the discrete data (appropriately distributed) is available, we apply 2D-FEM for finding approximate solutions of partial derivatives of curvilinear elements (either covariant or contravariant) of \mathbf{u} and \mathbf{w} , with respect to (Φ, Λ) (for more details refer to subsection 2.8.1). Hence, optimal finite element meshes can be generated by the Delaunay triangulation across the current GPS network of Southern California (see Fig. 2.17).

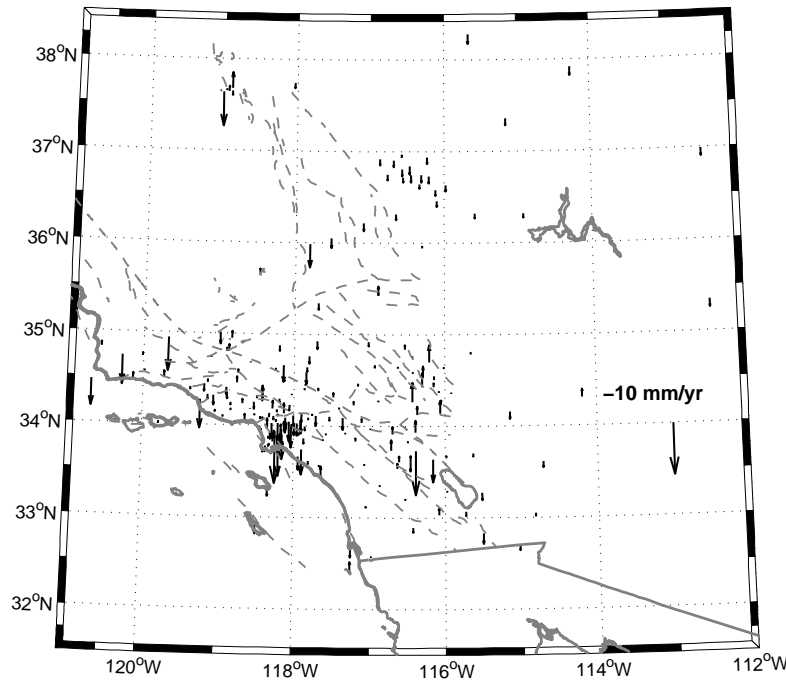


Figure 2.16: Vertical velocity field in units of $\text{mm}\cdot\text{yr}^{-1}$ across Southern California. The figure is illustrated in Albers equal-area conic projection.

As we mentioned in this chapter, for the proposed method of deformation analysis, to obtain first-order partial derivatives of GPS height ($H(\Lambda, \Phi)$), we need to attempt to find a continuous function of GPS height (see subsections 2.4.1 and 2.6.1). The ellipsoidal height (GPS height) is the sum of the geoid height $N(\Lambda, \Phi)$ and an orthometric height $\tilde{H}(\Lambda, \Phi)$, namely $H(\Lambda, \Phi) = \tilde{H}(\Lambda, \Phi) + N(\Lambda, \Phi)$. Hence, using a geoidal height model and orthometric height model, we can compute ellipsoidal height. Namely

- i. Obtaining orthometric height, through the National Elevation Dataset (NED) across Southern California, which can be freely downloaded (<http://seamless.usgs.gov/website/seamless/>). As a higher-resolution product, we made use of NED 1/9 arc second, which has a resolution of approximately 10 meters.
- ii. Obtaining geoidal height $N(\Lambda, \Phi)$, through geoid model for United States (GEOID03), which is freely available (<http://www.ngs.noaa.gov/GEOID/GEOID03/>). The GEOID03 model is known as a hybrid geoid model, combining gravimetric information with GPS ellipsoidal heights on leveled benchmarks. It includes combining gravimetric information with GPS ellipsoidal heights on leveled benchmarks.

Hence, in every triangle, around the computational point we set up a grid of points of ellipsoidal heights $H(\Lambda, \Phi)$. Then, the fitting surface of lowest possible degree (linear surface fitting), yields continuous ellipsoidal height as a function of longitude and latitude.

Remark 2.4 Gridding and contouring of the data for mapping applications, is performed by MATLAB. The gridding methods in MATLAB allow us to produce a reliable contour and surface from the

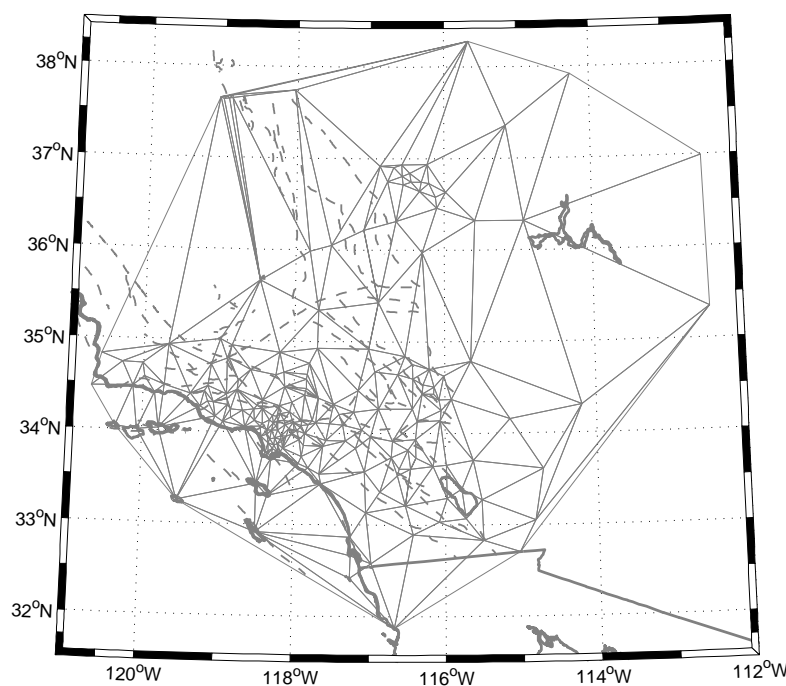


Figure 2.17: Delaunay triangulation of permanent GPS network across Southern California. The figure is illustrated in Albers equal-area conic projection.

data. The data can be randomly dispersed over the map area, and MATLAB's script for gridding, namely "Griddata", will interpolate data onto a grid. $ZI = \text{griddata}(x, y, z, XI, YI)$ fits a surface of the form $z = f(x, y)$ to the data in the (usually) non-uniformly spaced vectors (x, y, z) . Griddata interpolates this surface at the points specified by (XI, YI) to produce ZI . The surface always passes through the data points. XI and YI usually form a uniform grid (as produced by `meshgrid`). XI can be a row vector, in which case it specifies a matrix with constant columns. Similarly, YI can be a column vector, and it specifies a matrix with constant rows. $[XI, YI, ZI] = \text{griddata}(x, y, z, XI, YI)$ returns the interpolated matrix ZI as above, and also returns the matrices XI and YI formed from row vector XI and column vector yi . These latter are the same as the matrices returned by `meshgrid`. It uses the specified interpolation method:

- i. Linear : Triangle-based linear interpolation
- ii. Cubic : Triangle-based cubic interpolation
- iii. Nearest : Nearest neighbor interpolation

The method defines the type of surface fit to the data. The 'cubic' methods produce smooth surfaces while 'linear' and 'nearest' have discontinuities in the first and zero'th derivatives, respectively. All the methods are based on a Delaunay triangulation of the data. However it fails when there are replicates or when the data has many collinear points. "Gridfit" solves all of these problems, although it is not an interpolant. It builds a surface, by 2D splines, over a complete lattice, extrapolating smoothly into the corners. This script is freely available at Matlab's "Central File Exchange" (<http://www.mathworks.com/matlabcentral/fileexchange/loadCategory.do>).

Fig. 2.18 (a) represents the maximum geodetic strain-rate Λ_{\max} , in units of yr^{-1} as obtained from (2.30). The maximum geodetic strain-rate

$$\Lambda_{\max} = \max(|\Lambda_1|, |\Lambda_2|)$$

has the largest eigenvalue (Λ_1 or Λ_2 in absolute value) of the strain-rate tensor. In general, $\Lambda_1 + \Lambda_2 \neq 0$, so $\Lambda_{\max} \geq \left| \frac{\Lambda_1 - \Lambda_2}{2} \right|$, the maximum horizontal shear strain-rate Λ_{\max} offers a good representation of total deformation where only horizontal motions are available (or accurate)[Ward, 1998a,b].

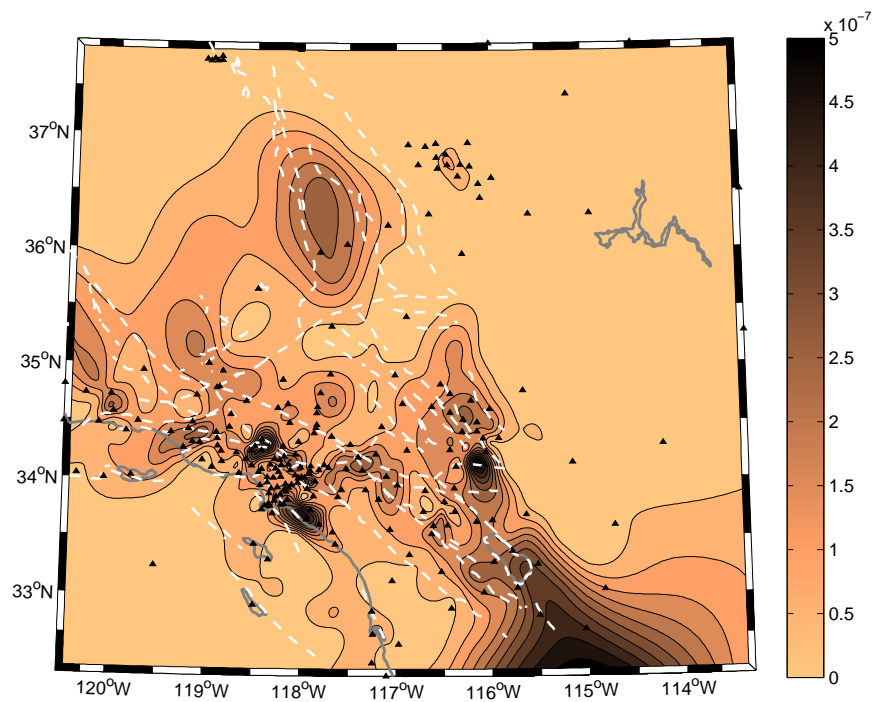
The strongest maximum of geodetic strain-rates is related to Landers area at rates of $4.7 \times 10^{-7} \text{ yr}^{-1}$, Southern part of SGF at rates of $4 \times 10^{-7} \text{ yr}^{-1}$, Salton Sea and Imperial Valley at rates of $3.8 \times 10^{-7} \text{ yr}^{-1}$. Most of the peaks are appearing near the SAF. However, Los Angeles and east-central Ventura Basin also exhibit a high maximum geodetic strain-rate of the order $4.2 \times 10^{-7} \text{ yr}^{-1}$.

The pattern of surface maximum shear strain-rate in units of yr^{-1} is illustrated in Fig. 2.18 (b). The surface maximum shear strain represents the anisotropic part of the strain tensor (see Eq. (2.36)), which is considered as a measure in crustal deformation. Its rate, in general, is similar to maximum geodetic strain-rates. The surface maximum shear strain-rates have greater values than the maximum geodetic strain-rates, due to their mathematical formulations.

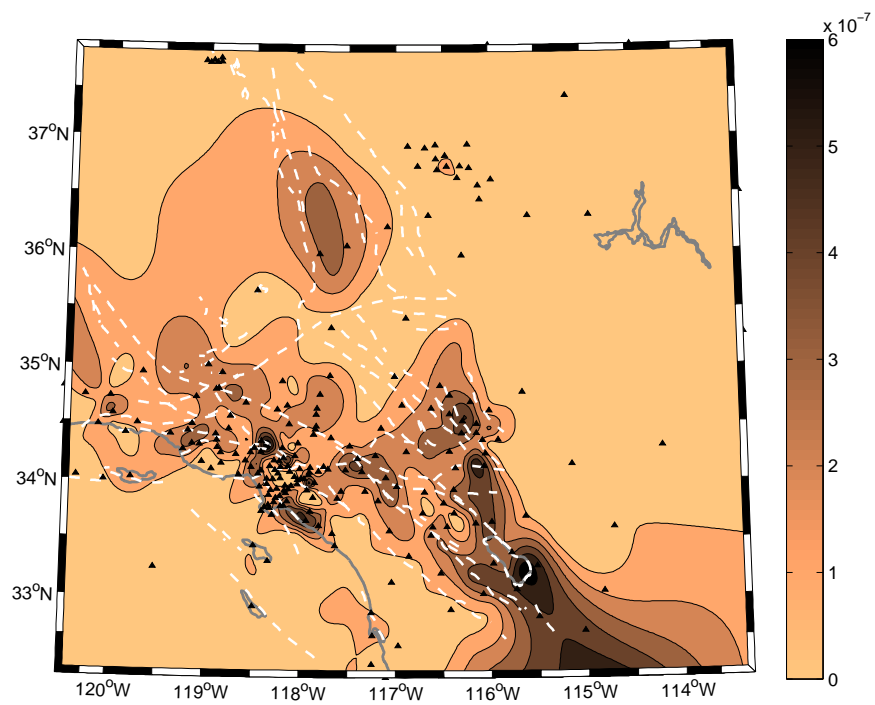
The highest surface maximum shear strain-rate lies in the area containing the creeping segments of SAF and Salton Sea area at rates of $6 \times 10^{-7} \text{ yr}^{-1}$. High surface maximum shear strain-rates are also observed at the Southern SGF, Hector Mine, Landers, Los Angeles Basin, Ventura Basin and Owens Valley. The regions of highest surface maximum shear strain-rate are not on the major faults as would be expected, but rather in the regions surrounding previous earthquakes. Earthquakes in 1999 (Hector Mine, M_w 7.1), 1994 (Northridge, M_w 6.7), 1992 (Landers, M_w 7.3), 1992 (Big Bear, M_w 6.4), 1979 (Imperial Valley, M_w 6.4), 1971 (San Fernando, M_w 6.6), 1952 (Kern County, M_w 7.7), 1942 (Salton Sea aftershock, M_w 6.4), 1933 (Los Angeles Basin, M_w 6.4) and 1872 (Owens Valley, M_w 7.6) have apparently caused the largest strain reactions. The monitoring of this pattern at regions with high seismic activity confirms the key role of the surface maximum shear strain-rate in earthquake studies.

Fig. 2.19 illustrates the surface dilatation rates, in units of yr^{-1} . The positive value denotes to extension and negative value represents compression. Surface dilatation represents the isotropic part of the deformation tensor. In the surface dilatation field, notable areas of compression are documented in the Los Angeles area about $-3.2 \times 10^{-7} \text{ yr}^{-1}$ and for Ventura Basin about $-4.2 \times 10^{-7} \text{ yr}^{-1}$. This contraction extends into the Santa Barbara channel, where its rate is $-2 \times 10^{-7} \text{ yr}^{-1}$. Another series of compressions appear in Southern Owens Valley at rates of $-2 \times 10^{-7} \text{ yr}^{-1}$. Negligible compression can be seen in the southern part of SAF Indio at rate of $-1 \times 10^{-7} \text{ yr}^{-1}$, possibly associated with after-effects of the 1940 Imperial Valley earthquake. Notable extensions appear in Landers with the rate of $4.3 \times 10^{-7} \text{ yr}^{-1}$, across Southern San Gabriel Fault with the rate $2 \times 10^{-7} \text{ yr}^{-1}$, and the last one is distributed between the Southern Elsinore, San Jacinto faults and northern Imperial Valley fault with rate $3.5 \times 10^{-7} \text{ yr}^{-1}$.

Moreover, the pattern of surface dilatation over Southern California is generally consistent with previous studies [Johnson et al., 1994; Snay et al., 1996; Shen et al., 1996; Shen-Tu et al., 1999]. Many local peaks (or valleys) in the dilatation rate field occur in vicinities of recent earthquakes, which implies that much of the rapid spatial variation in strain rate field is probably caused by transient deformation associated with recent earthquakes [Shen et al., 1996].



(a)



(b)

Figure 2.18: (a) Maximum geodetic surface strain-rate (b) Maximum shear strain-rate in units of yr^{-1} over Southern California. Faults are represented by white dashed lines, coastlines are represented by bold solid lines and triangles denote the permanent GPS stations. Figures are illustrated in Albers equal-area conic projection.

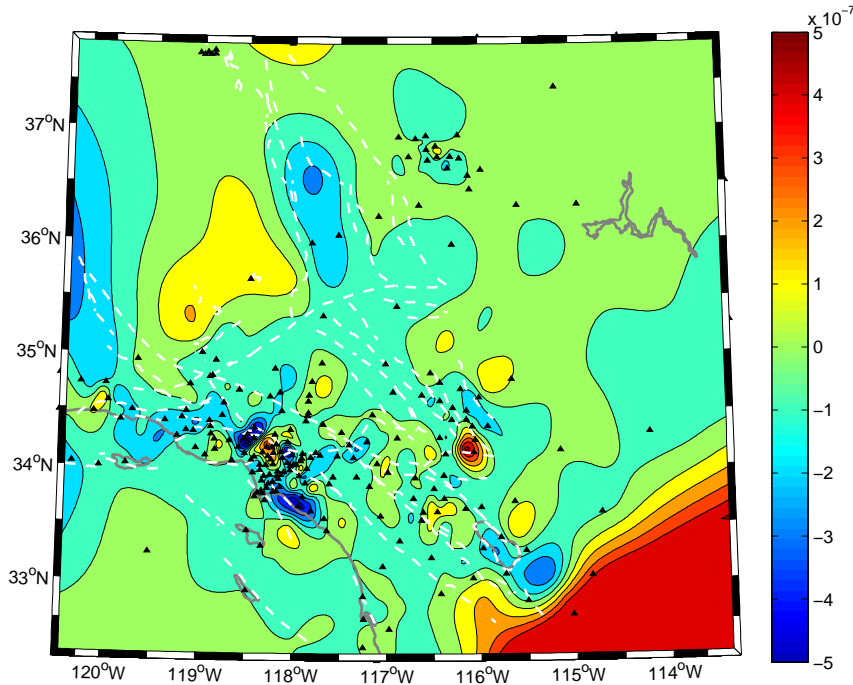
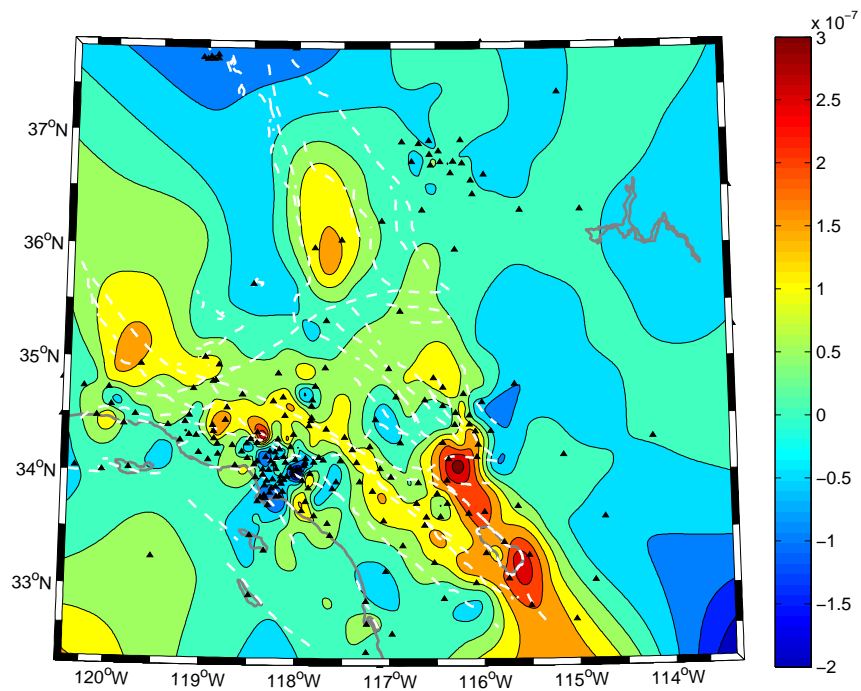


Figure 2.19: Surface dilation in units of yr^{-1} across Southern California. Faults are represented by white dashed lines, coastlines are represented by bold solid lines and triangles denote the permanent GPS stations. The figure is illustrated in Albers equal-area conic projection.

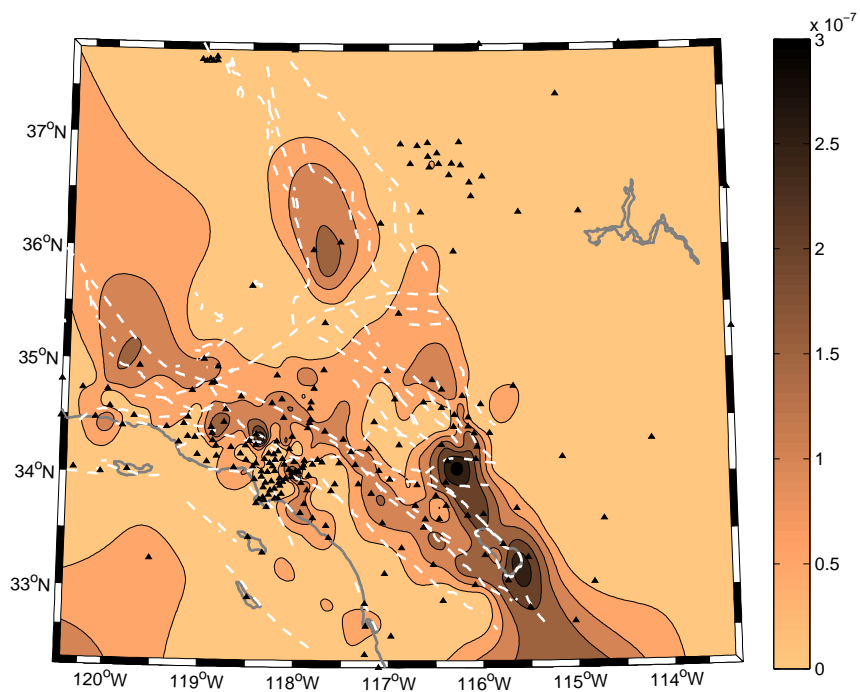
The pattern of the rotation around the normal (see Eq. (2.37)) in unit of $\text{rad}\cdot\text{yr}^{-1}$ is illustrated by Fig. 2.20 (a). The positive values indicate clockwise rotation around the normal (to the surface) and the negative values indicate counter clockwise rotation. The pattern can detect signals of current kinematics of the area. Large rotation rates are found along the SAF and the SJF, as expected from active wrenching dislocations along the two faults. The highest positive rotation signals are detected over the Landers at rates of $2.7 \times 10^{-7} \text{ rad}\cdot\text{yr}^{-1}$ and Imperial Valley at rates of $2.3 \times 10^{-7} \text{ rad}\cdot\text{yr}^{-1}$.

The highest rotation rates in the Landers and Imperial Valley rupture areas are consistent with post-seismic motions with the same sense as the main rupture. In the Ventura Basin region, it is monitored that the clockwise rotation are in the range between 0.1×10^{-7} and $1.5 \times 10^{-7} \text{ rad}\cdot\text{yr}^{-1}$. Other studies support this idea e.g., [Donnellan et al., 1993]. The eastern segment of Garlock fault rotates clockwise at rates $1.5 \times 10^{-7} \text{ rad}\cdot\text{yr}^{-1}$. A very limited area in Sierra-Nevada shows a negligible counter clockwise rotation at rates of $0.1 \times 10^{-7} \text{ rad}\cdot\text{yr}^{-1}$. Rather in the remote eastern part of Mojave Desert and the Southern Mojave region, counter clockwise rotation is documented at rates of $-0.5 \times 10^{-7} \text{ rad}\cdot\text{yr}^{-1}$. Fig. 2.20 (b) illustrates rates of absolute rotation around the normal. Comparison between this figure and the seismicity map of the area (see Fig. 2.13) proves that the rotation around the normal as a deformation tool can play a desirable role in earthquake investigations.

The pattern of difference between eigenvalues of TCC over Southern California is illustrated by Fig. 2.21 (a). Referring to its definition, Eq. (2.68), the difference is almost positively like the surface maximum shear strain rates. In general, this pattern is similar to the pattern of surface maximum shear strain rates and can detect areas with high surface deformations. Along ECSZ in Landers and



(a)



(b)

Figure 2.20: (a) Rotation around the normal (b) absolute rotation around the normal in units of rad.yr^{-1} over Southern California. Faults are represented by white dashed lines, coastlines are represented by bold solid lines and triangles denote the permanent GPS stations. Figures are illustrated in Albers equal-area conic projection.

Hector Mine at rates of $1 \times 10^{-7} \text{ yr}^{-1}$ is documented. The Salton Sea area and Imperial Valley areas are covered by peaks with the rate $1.2 \times 10^{-7} \text{ yr}^{-1}$. Other notable patterns are observed in Los Angeles areas, eastern of San Gabriel fault and Owens Valley. Interesting features are the peak of values around the southeastern part of Basin and Range, which could not be detected by the surface maximum shear strain rates. Moreover, a pattern of the sum of the eigenvalues of TCC is illustrated by Fig. 2.21 (b), where the pattern could be made either positive or negative.

Fig. 2.22 (a) and 2.22 (b) illustrate changes of mean and Gaussian curvatures in units of $\text{m}^{-1}.\text{yr}^{-1}$ and $\text{m}^{-2}.\text{yr}^{-1}$, respectively. Positive and negative values of mean curvature are related to upward and downward motions of the Earth's surface. Based on Fig. 2.22 (a) lands are undergoing subsidence in many areas (e.g., southern part of Owens Valley, southwestern part of Sierra-Nevada, southeastern part of Great Valley and Los Angeles). Notable rising features appear in ECSZ and the north-eastern part of the Mojave Desert.

Fig. 2.22 (c) illustrate patterns of GPS height components (in ITRF2000) over Southern California in units of $\text{mm}.\text{yr}^{-1}$. These patterns are obtained via the Delaunay triangulation of GPS network over Southern California (see Fig. 2.17). Positive values are connected to upward motions of the Earth's surface whereas negative values are related to downward motions of the Earth's surface. The significant subsidences are apparent in the north-western part of Salton Sea and Los Angeles Basin with rates $-2.4 \text{ mm}.\text{yr}^{-1}$ and the southern part of Owens Valley with rates of $-1.5 \text{ mm}.\text{yr}^{-1}$. The strongest rising peaks appear in the ECSZ and in the north part of Mojave Desert with rates of $1 \text{ mm}.\text{yr}^{-1}$.

Comparisons of Figs. 2.22 (a), 2.22(b) and 2.22(c) indicate the ability which changes of mean and Gaussian curvatures for describing the motion of the Earth's surface. They can represent a more reliable portraits of the deformed areas due to the following reasons:

- i. As mentioned in subsection 2.5.1, as well in section 2.7, through Gaussian curvature and mean curvature we can have a shape-classification based upon signs of mean and Gaussian curvatures. For instance, in Southern California, consistency in sign of mean and Gaussian curvatures when both are negative means the deformed shape is convex (ellipsoid) and consistency in sign of mean and Gaussian curvatures when both are positive means the deformed shape is Saddle Valley (see Fig. 2.8 and Tab. 2.2). This description of shape properties of the crust might provide new ways of studying the structure of the Earth's crust and its deformation.
- ii. Mean and Gaussian curvatures are invariants, they do not change under a set of transformations. In other words they reflect the inherent properties of the surface, and have geometrical meaning. However the pattern of GPS height components (see Fig. 2.22 (c)) is variant, and will change under set of transformations.

A Comparison with Horizontal Strain

The objective of this part is devoted to the comparison between the classical computation (plane strain analysis) and our proposed method. The classical method of deformation analysis (2D) is based upon extrinsic geometry which deals with the study of geometry relative to embedding spaces. We assumed that in 2D classical method, undeformed surface and deformed surface are planes. Hence, briefly, we describe the geometry of deformation (in plane)

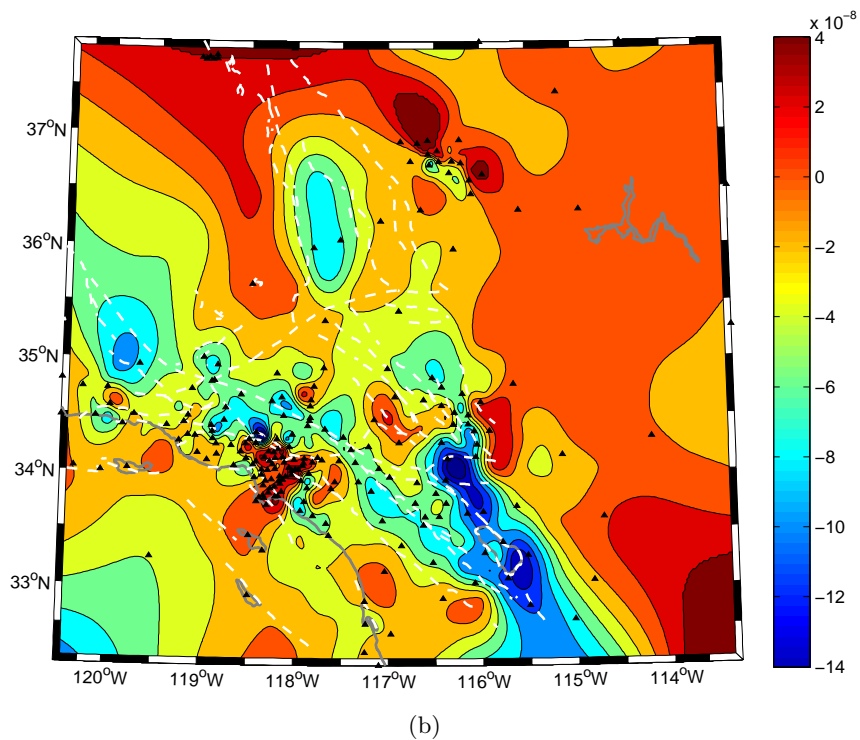
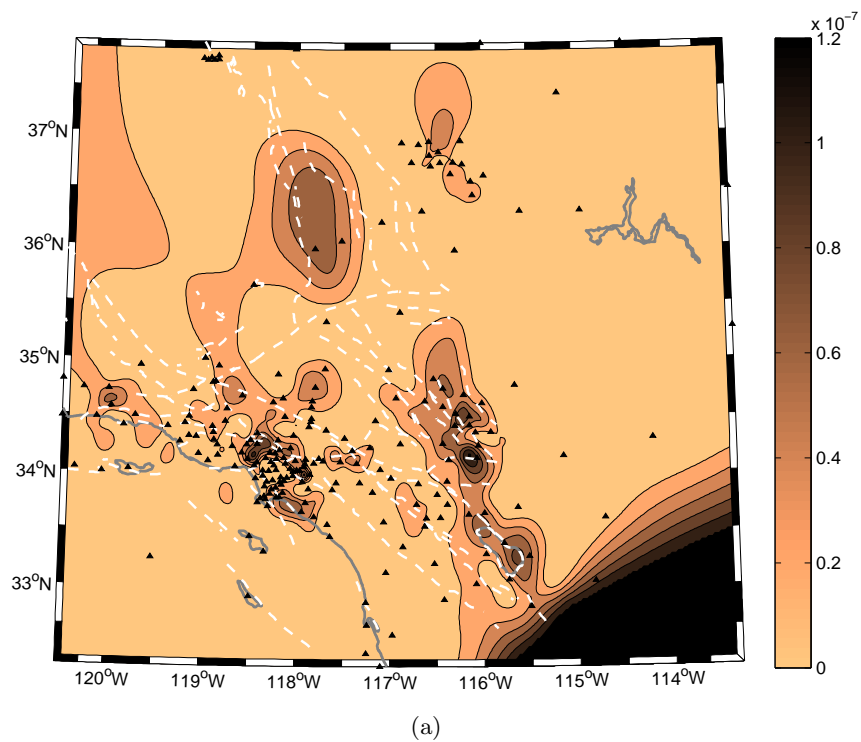


Figure 2.21: (a) Difference between eigenvalues of TCC in units of yr^{-1} (b) Sum of the eigenvalues of TCC in units of yr^{-1} over Southern California. Faults are represented by white dashed lines, coastlines are represented by bold solid lines and triangles denote the permanent GPS stations. Figures are illustrated in Albers equal-area conic projection.

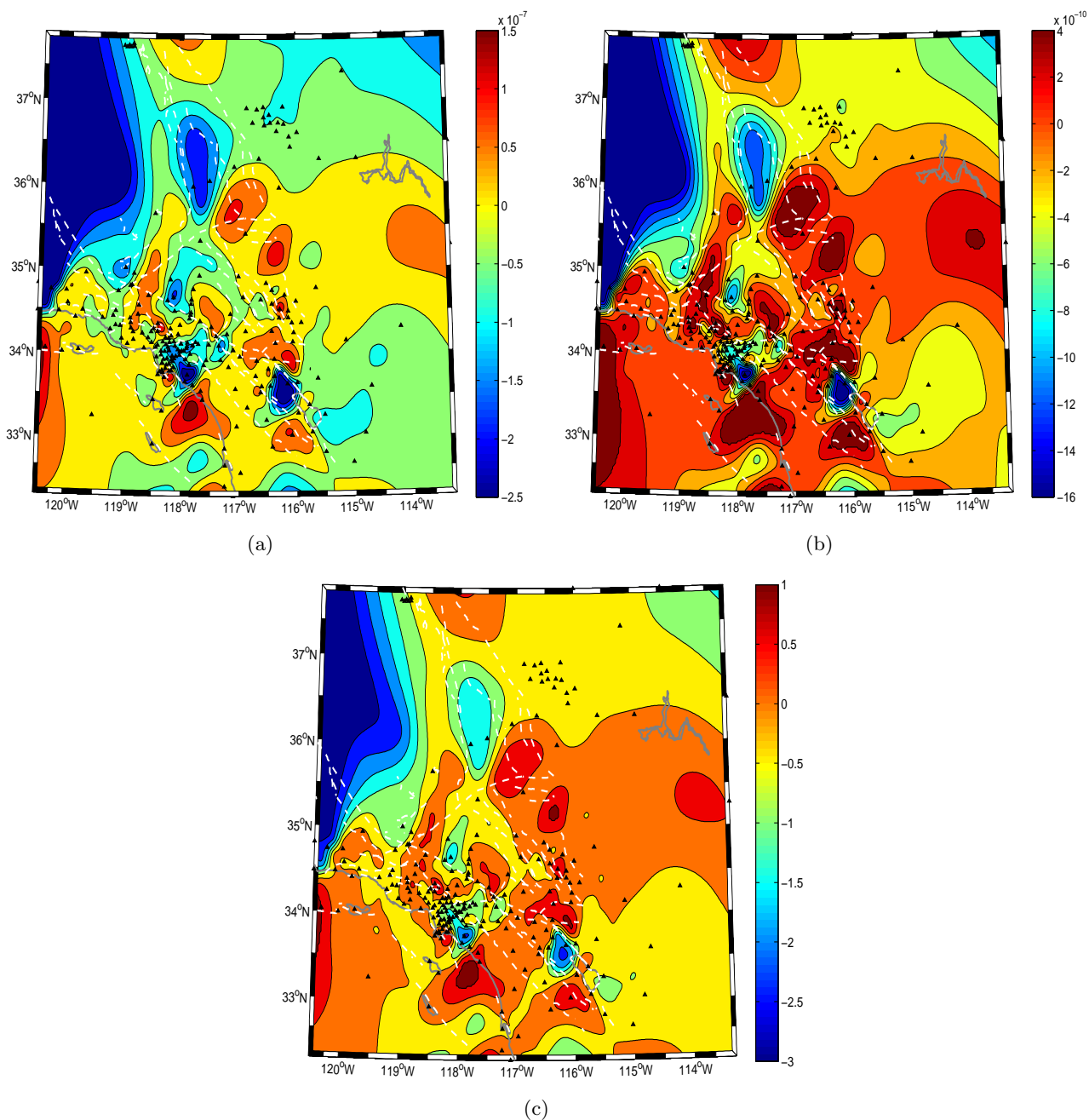


Figure 2.22: (a) Change of mean curvature in units of $\text{m}^{-1} \cdot \text{yr}^{-1}$, (b) change of Gaussian curvature in units of $\text{m}^{-2} \cdot \text{yr}^{-1}$, (c) patterns of GPS height components (in ITRF2000) in units of $\text{mm} \cdot \text{yr}^{-1}$ over Southern California. Faults are represented by white dashed lines, coastlines are represented by bold solid lines and triangles denote the permanent GPS stations. Figures are illustrated in Albers equal-area conic projection.

- i. Base vectors of undeformed surface $\{\mathbf{J}_1, \mathbf{J}_2\}$ are mutually orthogonal, as well as basis vectors of deformed surface $\{\mathbf{j}_1, \mathbf{j}_2\}$ (contrary to basis vectors in proposed method which are not orthogonal). Therefore, every vector can be described through material coordinates $\mathbf{u} = U^1 \mathbf{J}_1 + U^2 \mathbf{J}_2$ or by spatial coordinates $\mathbf{u} = u^1 \mathbf{j}_1 + u^2 \mathbf{j}_2$.
- ii. Metric tensors before deformation and after deformation are the same and matrix forms of them are equal to the identity matrix or unit matrix (contrary to the metric tensor in the proposed method which is not diagonal).
- iii. Local coordinates of an undeformed body can be illustrated by $\{X^1, X^2\}$, while the coordinates system of a deformed body can be illustrated by $\{x^1, x^2\}$.

Based upon these assumptions, and referring to definitions of Cauchy-Green deformation tensors (Eq. 2.15) we have

$$\mathbf{C}_l = \begin{bmatrix} \left\langle \frac{\partial \mathbf{x}}{\partial X^1}, \frac{\partial \mathbf{x}}{\partial X^1} \right\rangle & \left\langle \frac{\partial \mathbf{x}}{\partial X^1}, \frac{\partial \mathbf{x}}{\partial X^2} \right\rangle \\ \left\langle \frac{\partial \mathbf{x}}{\partial X^2}, \frac{\partial \mathbf{x}}{\partial X^1} \right\rangle & \left\langle \frac{\partial \mathbf{x}}{\partial X^2}, \frac{\partial \mathbf{x}}{\partial X^2} \right\rangle \end{bmatrix} \quad \text{vs.} \quad \mathbf{C}_r = \begin{bmatrix} \left\langle \frac{\partial \mathbf{X}}{\partial x^1}, \frac{\partial \mathbf{X}}{\partial x^1} \right\rangle & \left\langle \frac{\partial \mathbf{X}}{\partial x^1}, \frac{\partial \mathbf{X}}{\partial x^2} \right\rangle \\ \left\langle \frac{\partial \mathbf{X}}{\partial x^2}, \frac{\partial \mathbf{X}}{\partial x^1} \right\rangle & \left\langle \frac{\partial \mathbf{X}}{\partial x^2}, \frac{\partial \mathbf{X}}{\partial x^2} \right\rangle \end{bmatrix}$$

Using $\mathbf{u} = \mathbf{x} - \mathbf{X}$ and recalling the basis vectors $\frac{\partial \mathbf{X}}{\partial X^\Phi} = \mathbf{J}_\Phi$ and $\frac{\partial \mathbf{x}}{\partial x^\phi} = \mathbf{j}_\phi$ in which $\Phi, \phi \in \{1, 2\}$, we have

$$\begin{aligned} \mathbf{C}_l &= \begin{bmatrix} \left\langle \frac{\partial(\mathbf{X}+\mathbf{u})}{\partial X^1}, \frac{\partial(\mathbf{X}+\mathbf{u})}{\partial X^1} \right\rangle & \left\langle \frac{\partial(\mathbf{X}+\mathbf{u})}{\partial X^1}, \frac{\partial(\mathbf{X}+\mathbf{u})}{\partial X^2} \right\rangle \\ \left\langle \frac{\partial(\mathbf{X}+\mathbf{u})}{\partial X^2}, \frac{\partial(\mathbf{X}+\mathbf{u})}{\partial X^1} \right\rangle & \left\langle \frac{\partial(\mathbf{X}+\mathbf{u})}{\partial X^2}, \frac{\partial(\mathbf{X}+\mathbf{u})}{\partial X^2} \right\rangle \end{bmatrix} \quad \text{vs.} \quad \mathbf{C}_r = \begin{bmatrix} \left\langle \frac{\partial(\mathbf{x}-\mathbf{u})}{\partial x^1}, \frac{\partial(\mathbf{x}-\mathbf{u})}{\partial x^1} \right\rangle & \left\langle \frac{\partial(\mathbf{x}-\mathbf{u})}{\partial x^1}, \frac{\partial(\mathbf{x}-\mathbf{u})}{\partial x^2} \right\rangle \\ \left\langle \frac{\partial(\mathbf{x}-\mathbf{u})}{\partial x^2}, \frac{\partial(\mathbf{x}-\mathbf{u})}{\partial x^1} \right\rangle & \left\langle \frac{\partial(\mathbf{x}-\mathbf{u})}{\partial x^2}, \frac{\partial(\mathbf{x}-\mathbf{u})}{\partial x^2} \right\rangle \end{bmatrix} \\ \mathbf{C}_l &\doteq \begin{bmatrix} 1 + 2\frac{\partial U^1}{\partial X^1} & 0 + \frac{\partial U^1}{\partial X^2} + \frac{\partial U^2}{\partial X^1} \\ 0 + \frac{\partial U^2}{\partial X^1} + \frac{\partial U^1}{\partial X^2} & 1 + 2\frac{\partial U^2}{\partial X^2} \end{bmatrix} \quad \text{vs.} \quad \mathbf{C}_r \doteq \begin{bmatrix} 1 - 2\frac{\partial u^1}{\partial x^1} & 0 - \frac{\partial u^1}{\partial x^2} - \frac{\partial u^2}{\partial x^1} \\ 0 - \frac{\partial u^2}{\partial x^1} - \frac{\partial u^1}{\partial x^2} & 1 - 2\frac{\partial u^2}{\partial x^2} \end{bmatrix} \end{aligned} \quad (2.71)$$

which is based on the dropping or approximating of nonlinear terms $\frac{\partial U^\Phi}{\partial X^\Phi} \frac{\partial U^\Lambda}{\partial X^\Lambda}$ and $\frac{\partial u^\phi}{\partial x^\phi} \frac{\partial u^\lambda}{\partial x^\lambda}$, in left and right sides, respectively. Hence, using Eqs. (2.18) and (2.71) we can obtain strain tensors

$$\begin{aligned} \mathbf{E}_l &= \frac{1}{2}(\mathbf{C}_l - \mathbf{A}_l) = \frac{1}{2}(\mathbf{C}_l - \mathbf{I}) \quad \text{vs.} \quad \mathbf{E}_r = \frac{1}{2}(\mathbf{A}_r - \mathbf{C}_r) = \frac{1}{2}(\mathbf{I} - \mathbf{C}_r) \\ \mathbf{E}_l &= \begin{bmatrix} \frac{\partial U^1}{\partial X^1} & \frac{1}{2}\left(\frac{\partial U^1}{\partial X^2} + \frac{\partial U^2}{\partial X^1}\right) \\ \frac{1}{2}\left(\frac{\partial U^2}{\partial X^1} + \frac{\partial U^1}{\partial X^2}\right) & \frac{\partial U^2}{\partial X^2} \end{bmatrix} \quad \text{vs.} \quad \mathbf{E}_r = \begin{bmatrix} \frac{\partial u^1}{\partial x^1} & \frac{1}{2}\left(\frac{\partial u^1}{\partial x^2} + \frac{\partial u^2}{\partial x^1}\right) \\ \frac{1}{2}\left(\frac{\partial u^2}{\partial x^1} + \frac{\partial u^1}{\partial x^2}\right) & \frac{\partial u^2}{\partial x^2} \end{bmatrix} \end{aligned}$$

which are called *infinitesimal strain tensors*. Infinitesimal rotation tensors can be obtained by

$$\mathbf{R}_l = \begin{bmatrix} 0 & \frac{1}{2}\left(\frac{\partial U^1}{\partial X^2} - \frac{\partial U^2}{\partial X^1}\right) \\ \frac{1}{2}\left(\frac{\partial U^2}{\partial X^1} - \frac{\partial U^1}{\partial X^2}\right) & 0 \end{bmatrix} \quad \text{vs.} \quad \mathbf{R}_r = \begin{bmatrix} 0 & \frac{1}{2}\left(\frac{\partial u^1}{\partial x^2} - \frac{\partial u^2}{\partial x^1}\right) \\ \frac{1}{2}\left(\frac{\partial u^2}{\partial x^1} - \frac{\partial u^1}{\partial x^2}\right) & 0 \end{bmatrix}$$

Application of this method in geodetic and geodynamic networks can be found in Vanicek et al. [1981]; Argus et al. [1989]; Ahjos and Uski [1992]; Dermanis and Grafarend [1993]; Heck et al. [1995]; Bada et al. [1999]; Heck [1999]; Adam et al. [2002]; LaFemina et al. [2005]; Mazzotti et al. [2005]; Walpersdorf et al. [2006]; Cai and Grafarend [2007a,b] and many other papers that couldn't be included in the print.

In order to compare our proposed method and the plane strain, we consider

- i. Local Cartesian terrestrial frame (e.g., ITRF, WGS84)
- ii. Infinitesimal displacements vector

Hence, we apply the plane strain method over Southern California, through the same GPS arrays which are used in subsection 2.8.2. The principal quantities of the strain tensor (maximum shear strain rate, dilatation rate and rotation rate) are illustrated by Figs. 2.23 (a), 2.23(b) and 2.23(c), respectively, which are derived by the plane strain method. The comparison can be divided into three categories:

- i. Comparison of the maximum shear strain rate in the classical method (Figs. 2.23 (a)) with maximum shear strain rate by our proposed method (Fig. 2.18 (b)) suggests that along the ECSZ, Hector Mine, Landers and Imperial Valley, roughly in eastern parts of SAF, our method represents a high magnitude of the maximum shear-strain rate.
- ii. Comparison of the dilatation rate in the classical method (Figs. 2.23 (b)) with the dilatation rate by our proposed method (Fig. 2.19) shows additional extensions in particular areas along the eastern parts of SAF (e.g., Landers, eastern Mojave Desert and east of the southern Sierra Nevada).
- iii. Comparison of the rotation rate in the classical method (Figs. 2.23 (c)) with the rotation rate by our proposed method (Fig. 2.20 (a)) shows additional rotations in imperial valley and ESCZ.

It seems that the differences between corresponding patterns of two methods could be discussed from the two points :

- i. Modeling of the displacement problem which we solved the problem on the real surface of the Earth (see Eq. (2.23) through (2.27))
- ii. Effect of ignoring the height components of the deformation field in horizontal strain rates.

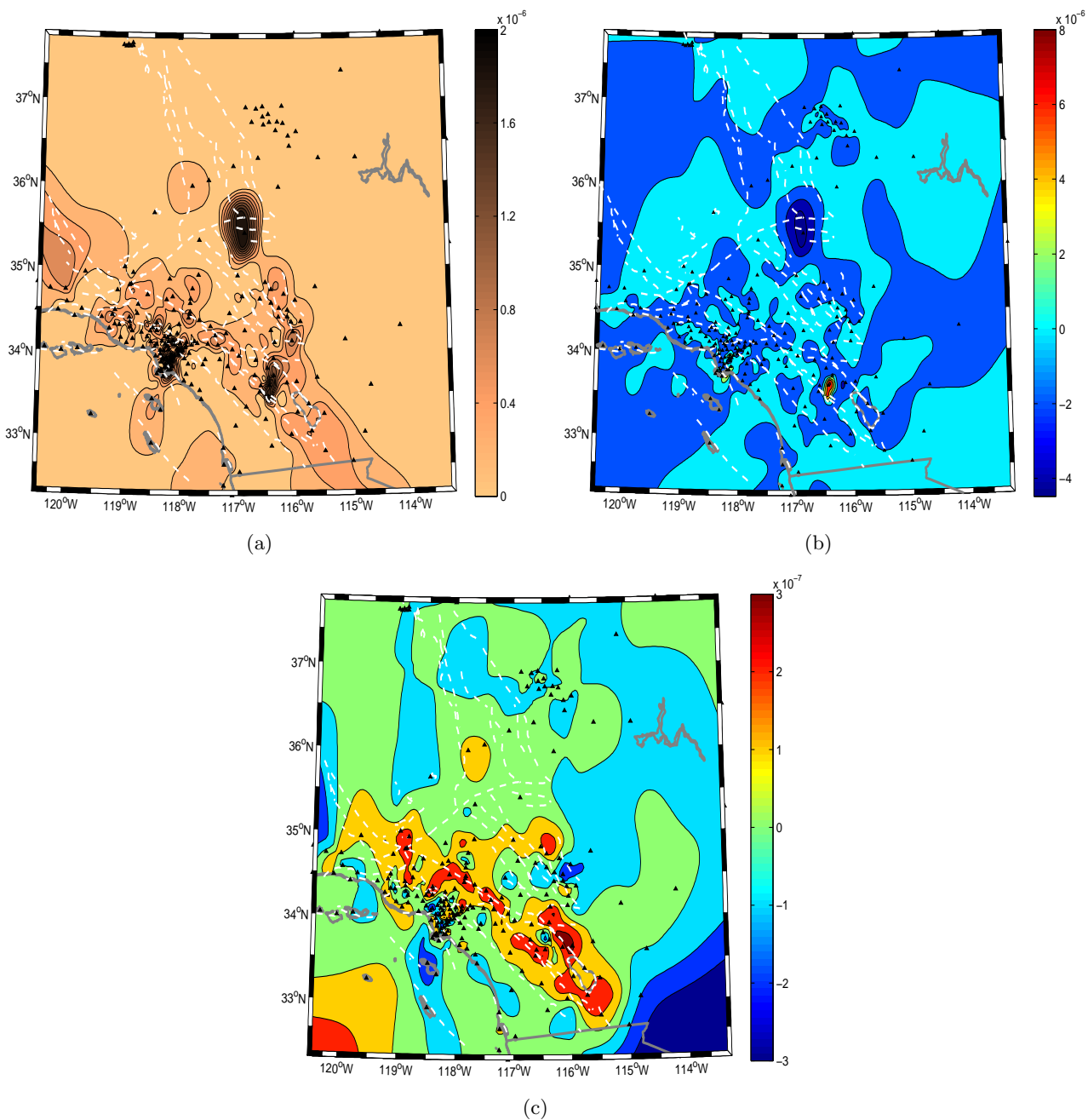


Figure 2.23: Principal quantities of strain tensor derived by 2D classical method : (a) Maximum shear strain rate in units of yr^{-1} , (b) dilatation in units of yr^{-1} , (c) rotation in units of rad.yr^{-1} over Southern California. Faults are represented by white dashed lines, coastlines are represented by bold solid lines and triangles denote the permanent GPS stations. The figure is illustrated in Albers equal-area conic projection.

Chapter 3

Stochastic Aspects

Stochastic behavior of eigenspace components (in strain tensor and TCC) in the presence of errors in measuring a random displacement field (under the normal distribution assumption of displacement field) is discussed in this chapter. The propagation of errors from the displacement vector into elements of strain tensor are formulated in section 3.1. In section 3.2 a propagation of errors from the displacement vector into elements of TCC are discussed.

In section 3.3 we deal with error propagation for eigenspace components, using dispersion matrices of tensor components (strain or TCC) which we derived in the previous two sections. However, due to the intricacy of the relations between tensor components (strain or TCC) and their eigenspace components, we proceeded via simultaneous diagonalization.

This section is followed by the linearization of the nonlinear multivariate Gauss- Markov model, which links the elements of transformed tensors (obtained by simultaneously diagonalization) with the eigenspace components. Then, we set up an observation model based on a linearized model under sampling of eigenspace synthesis. Furthermore, we establish linearized observation equations for n samples of *independent* random vectors from transformed tensor elements (under the normal distribution assumption), each with individual variance matrix. This will provide us with the second-order statistics of the eigenspace components.

In section 3.4, we estimate the covariance components between transformed tensor elements by Helmert estimator, based on prior information of variance components (given from section 3.3). Section 3.5 is devoted to presenting a numerical example with the crustal deformation field (through the continuous GPS data) in Cascadia Subduction Zone (CSZ).

In this chapter, for simplicity, we will use Lagrangian coordinates (or material coordinates) and the discussion would be the same in Eulerian coordinates.

3.1 Error Propagations for Strain Components

In the presence of errors in measuring the random displacement vectors (e.g., by GPS), we assume that \mathbf{Q}_u be a covariance matrix of random observations in which $\mathbf{Q}_u \in \mathbb{R}^{3 \times 3}$ (under the normal distribution assumption of displacement field). Therefore, the over all aim of this section is to discuss the propagation of errors from displacement vector into elements of strain tensor.

Recalling the strain tensor, whose components are dependent on the first-order partial derivatives

of the displacement vector with respect to material coordinates $\mathbf{u}_{,\Lambda}$, then dealing with dispersion matrix $D\{\mathbf{u}_{,\Lambda}\}$ makes an essential part of this section.

In the previous chapter, we could described a displacement vector \mathbf{u} in terms of linear combinations of vector space $\{\mathbf{A}_1, \mathbf{A}_2, \mathbf{A}_3\}$ or $\{\mathbf{A}^1, \mathbf{A}^2, \mathbf{A}^3\}$. Namely

$$\mathbf{u} = \tilde{U}^K \mathbf{A}_K = \tilde{U}_K \mathbf{A}^K \implies \mathbf{u}_{,\Lambda} = \frac{\partial \mathbf{u}}{\partial \Theta^\Lambda} = \frac{\partial(\tilde{U}^K \mathbf{A}_K)}{\partial \Theta^\Lambda} = \frac{\partial(\tilde{U}_K \mathbf{A}^K)}{\partial \Theta^\Lambda}, \quad \mathbf{u} \in \mathbb{R}^{1 \times 3}, \mathbf{A}^K, \mathbf{A}_K \in \mathbb{R}^{3 \times 1}$$

or, in matrix notations

$$\begin{aligned} \mathbf{u}_{,\Lambda} &= [\mathbf{A}_1 \quad \mathbf{A}_2 \quad \mathbf{A}_3] \begin{bmatrix} \tilde{U}_{,\Lambda}^1 \\ \tilde{U}_{,\Lambda}^2 \\ \tilde{U}_{,\Lambda}^3 \end{bmatrix} + [\mathbf{A}_{1,\Lambda} \quad \mathbf{A}_{2,\Lambda} \quad \mathbf{A}_{3,\Lambda}] \begin{bmatrix} \tilde{U}^1 \\ \tilde{U}^2 \\ \tilde{U}^3 \end{bmatrix} = \\ &= [\mathbf{A}^1 \quad \mathbf{A}^2 \quad \mathbf{A}^3] \begin{bmatrix} \tilde{U}_{1,\Lambda} \\ \tilde{U}_{2,\Lambda} \\ \tilde{U}_{3,\Lambda} \end{bmatrix} + [\mathbf{A}_{,\Lambda}^1 \quad \mathbf{A}_{,\Lambda}^2 \quad \mathbf{A}_{,\Lambda}^3] \begin{bmatrix} \tilde{U}_1 \\ \tilde{U}_2 \\ \tilde{U}_3 \end{bmatrix} \end{aligned}$$

Notice that, following convention, a comma indicates partial derivatives namely $\tilde{U}_{,\Lambda}^K = \frac{\partial \tilde{U}^K}{\partial \Theta^\Lambda}$, $\tilde{U}_{K,\Lambda} = \frac{\partial \tilde{U}_K}{\partial \Theta^\Lambda}$, $\mathbf{A}_{,\Lambda}^K = \frac{\partial \mathbf{A}^K}{\partial \Theta^\Lambda}$ and $\mathbf{A}_{K,\Lambda} = \frac{\partial \mathbf{A}_K}{\partial \Theta^\Lambda}$, where obtaining the first-order partial derivatives of local base vectors with respect to the curvilinear coordinates, namely $\mathbf{A}_{,\Lambda}^K$ and $\mathbf{A}_{K,\Lambda}$ are described in Appendix A. Now, dispersion matrix of $\mathbf{u}_{,\Lambda}$ is

$$\begin{aligned} D\{\mathbf{u}_{,\Lambda}\} &= [\mathbf{A}_1 \quad \mathbf{A}_2 \quad \mathbf{A}_3] \mathbf{Q}_{\tilde{U}_{,\Lambda}^K} [\mathbf{A}_1 \quad \mathbf{A}_2 \quad \mathbf{A}_3]^T + \\ &+ [\mathbf{A}_{1,\Lambda} \quad \mathbf{A}_{2,\Lambda} \quad \mathbf{A}_{3,\Lambda}] \mathbf{Q}_{\tilde{U}^K} [\mathbf{A}_{1,\Lambda} \quad \mathbf{A}_{2,\Lambda} \quad \mathbf{A}_{3,\Lambda}]^T = \mathbf{Q}_{\mathbf{u}_{,\Lambda}}, \quad D\{\mathbf{u}_{,\Lambda}\} \in \mathbb{R}^{3 \times 3} \end{aligned} \quad (3.1)$$

where

$$\tilde{U}^K = \langle \mathbf{u}, \mathbf{A}^K \rangle \implies D\{\tilde{U}^K\} = [\mathbf{A}^1 \quad \mathbf{A}^2 \quad \mathbf{A}^3] \mathbf{Q}_{\mathbf{u}} [\mathbf{A}^1 \quad \mathbf{A}^2 \quad \mathbf{A}^3]^T = \mathbf{Q}_{\tilde{U}^K}, \quad D\{\tilde{U}^K\} \in \mathbb{R}^{3 \times 3} \quad (3.2)$$

However, covariance matrix of first-order partial derivatives of contravariant elements with respect to the material coordinates $\mathbf{Q}_{\tilde{U}_{,\Lambda}^K}$ can be obtained by propagation of errors from \tilde{U}^K or \tilde{U}_K into their first-order partial derivatives (according to modeling of displacement field). More detailed discussion is presented in Appendix B.

Analogous to Eq. (3.1), we can obtain the dispersion matrix of $\mathbf{u}_{,\Lambda}$ through covariant components

$$\begin{aligned} D\{\mathbf{u}_{,\Lambda}\} &= [\mathbf{A}^1 \quad \mathbf{A}^2 \quad \mathbf{A}^3] \mathbf{Q}_{\tilde{U}_{K,\Lambda}} [\mathbf{A}^1 \quad \mathbf{A}^2 \quad \mathbf{A}^3]^T + \\ &+ [\mathbf{A}_{,\Lambda}^1 \quad \mathbf{A}_{,\Lambda}^2 \quad \mathbf{A}_{,\Lambda}^3] \mathbf{Q}_{\tilde{U}_K} [\mathbf{A}_{,\Lambda}^1 \quad \mathbf{A}_{,\Lambda}^2 \quad \mathbf{A}_{,\Lambda}^3]^T \end{aligned} \quad (3.3)$$

where

$$\tilde{U}_K = \langle \mathbf{u}, \mathbf{A}_K \rangle \Rightarrow D\{\tilde{U}_K\} = [\mathbf{A}_1 \ \mathbf{A}_2 \ \mathbf{A}_3] \mathbf{Q}_{\mathbf{u}} [\mathbf{A}_1 \ \mathbf{A}_2 \ \mathbf{A}_3]^T = \mathbf{Q}_{\tilde{U}_K}, \quad D\{\tilde{U}_K\} \in \mathbb{R}^{3 \times 3} \quad (3.4)$$

Hence, using Eq. (3.1) or (3.3), dispersion matrix of strain components can be obtained by

$$E_{\Lambda\Phi} = \frac{1}{2} (\langle \mathbf{u}_{,\Lambda}, \mathbf{u}_{,\Phi} \rangle + \langle \mathbf{u}_{,\Lambda}, \mathbf{A}_{\Phi} \rangle + \langle \mathbf{A}_{\Lambda}, \mathbf{u}_{,\Phi} \rangle)$$

$$D\{\tilde{\mathbf{p}}\} = \begin{bmatrix} \mathbf{A}_1 + \mathbf{u}_{,1} & 0 \\ \frac{1}{2}(\mathbf{A}_2 + \mathbf{u}_{,2}) & \frac{1}{2}(\mathbf{A}_1 + \mathbf{u}_{,1}) \\ 0 & \mathbf{A}_2 + \mathbf{u}_{,2} \end{bmatrix} \begin{bmatrix} \mathbf{Q}_{\mathbf{u},1} & 0 \\ 0 & \mathbf{Q}_{\mathbf{u},2} \end{bmatrix} \begin{bmatrix} \mathbf{A}_1 + \mathbf{u}_{,1} & 0 \\ \frac{1}{2}(\mathbf{A}_2 + \mathbf{u}_{,2}) & \frac{1}{2}(\mathbf{A}_1 + \mathbf{u}_{,1}) \\ 0 & \mathbf{A}_2 + \mathbf{u}_{,2} \end{bmatrix}^T = \mathbf{Q}_{\tilde{\mathbf{p}}}, \quad D\{\tilde{\mathbf{p}}\} \in \mathbb{R}^{3 \times 3} \quad (3.5)$$

where vector $\tilde{\mathbf{p}}$ denotes to the vector-half form of symmetric strain tensor

$$\tilde{\mathbf{p}} := \text{vh}(\mathbf{E}_l) = [E_{11} \ E_{12} \ E_{22}]^T \in \mathbb{R}^{3 \times 1}$$

Remark 3.1 Definition (vh-operator): Let \mathbf{E} be an arbitrary symmetric matrix of size u . The vh-operator of \mathbf{E} will contain $\frac{1}{2}u(u+1)$ distinct elements of \mathbf{E}_{ij} .

3.2 Error Propagations for TCC Components

In previous chapter, in section 2.6, the tensor of changes of curvature (TCC) was stated in terms of difference across the unit normal vectors in undeformed and deformed surfaces, namely $\mathbf{w} = \mathbf{a}_3 - \mathbf{A}_3$. On the other hand, we have observed how the unit normal vectors on surfaces (deformed and undeformed) can be constructed by cross product of tangent basis vectors. Likewise, through Eq. (2.62), we showed that tangent basis vectors on deformed surface depend on material basis vectors $\{\mathbf{A}_1, \mathbf{A}_2, \mathbf{A}_3\}$ and curvilinear components of displacement vector.

Then, at the first stage, existing errors in curvilinear components of displacement vector (see Eqs. (3.2) and (3.4)) will propagate to the tangent basis vectors on a deformed surface, then to the unit normal vectors on a deformed surface and finally will propagate to the TCC elements. First, we deal with the error propagation in tangent basis vectors (on a deformed surface) in the presence of errors in curvilinear components of displacement vector. Namely:

$$\mathbf{a}_\lambda = \ell_{,\lambda}^\alpha \mathbf{A}_\alpha + \zeta_\lambda \mathbf{A}_3 = [\mathbf{A}_1 \ \mathbf{A}_2 \ \mathbf{A}_3] \begin{bmatrix} \ell_{,\lambda}^1 & 0 & 0 \\ 0 & \ell_{,\lambda}^2 & 0 \\ 0 & 0 & \zeta_\lambda \end{bmatrix}, \quad \mathbf{A}_K \in \mathbb{R}^{3 \times 1}$$

$$D\{\mathbf{a}_\lambda\} = [\mathbf{A}_1 \ \mathbf{A}_2 \ \mathbf{A}_3] \begin{bmatrix} \sigma_{\ell_{,\lambda}^1}^2 & 0 & 0 \\ 0 & \sigma_{\ell_{,\lambda}^2}^2 & 0 \\ 0 & 0 & \sigma_{\zeta_\lambda}^2 \end{bmatrix} [\mathbf{A}_1 \ \mathbf{A}_2 \ \mathbf{A}_3]^T = \mathbf{Q}_{\mathbf{a}_\lambda}, \quad D\{\mathbf{a}_\lambda\} \in \mathbb{R}^{3 \times 3}$$

where covariance components $\sigma_{\ell_{,\lambda}^1}^2, \sigma_{\ell_{,\lambda}^2}^2, \sigma_{\zeta_\lambda}^2$ could be achieved by variance propagation of curvilinear coordinates in Eqs. (2.63) and (2.64). Hence, dispersion matrices of tangent basis vectors $\mathbf{Q}_{\mathbf{a}_1}$ and $\mathbf{Q}_{\mathbf{a}_2}$ could be propagated to unit normal vector \mathbf{a}_3 through linearization technique

$$\mathbf{a}_3 = \frac{\mathbf{a}_1 \times \mathbf{a}_2}{\|\mathbf{a}_1 \times \mathbf{a}_2\|}, \quad \mathbf{a}_k \in \mathbb{R}^{3 \times 1}$$

$$\mathbf{a}_3 \doteq \frac{\partial \mathbf{a}_3}{\partial \mathbf{a}_1} \mathbf{a}_1 + \frac{\partial \mathbf{a}_3}{\partial \mathbf{a}_2} \mathbf{a}_2 = \begin{bmatrix} \frac{\partial \mathbf{a}_3}{\partial \mathbf{a}_1} & \frac{\partial \mathbf{a}_3}{\partial \mathbf{a}_2} \end{bmatrix} \begin{bmatrix} \mathbf{a}_1 \\ \mathbf{a}_2 \end{bmatrix}$$

$$D\{\mathbf{a}_3\} = \begin{bmatrix} \frac{\partial \mathbf{a}_3}{\partial \mathbf{a}_1} & \frac{\partial \mathbf{a}_3}{\partial \mathbf{a}_2} \end{bmatrix} \begin{bmatrix} \mathbf{Q}_{\mathbf{a}_1} & 0 \\ 0 & \mathbf{Q}_{\mathbf{a}_2} \end{bmatrix} \begin{bmatrix} \frac{\partial \mathbf{a}_3}{\partial \mathbf{a}_1} & \frac{\partial \mathbf{a}_3}{\partial \mathbf{a}_2} \end{bmatrix}^T$$

Then, dispersion matrix $D\{\mathbf{a}_3\}$ can be transferred to the difference vector of unit normal vectors \mathbf{w} , through

$$\mathbf{w} = \mathbf{a}_3 - \mathbf{A}_3 \Rightarrow D\{\mathbf{w}\} = D\{\mathbf{a}_3\}, \quad D\{\mathbf{w}\} \in \mathbb{R}^{3 \times 3}$$

Now, we recall the tensor of changes of curvature (TCC), which is influenced by the first derivatives of \mathbf{w} with respect to material coordinates $\mathbf{w}_{,\Lambda}$. Hence, in order to achieve dispersion matrix of TCC components, as a first step, we should deal with the dispersion matrix $D\{\mathbf{w}_{,\Lambda}\}$. Namely, by splitting \mathbf{w} into its curvilinear coordinates we have

$$\mathbf{w} = \tilde{W}^K \mathbf{A}_K = \tilde{W}_K \mathbf{A}^K \Rightarrow \mathbf{w}_{,\Lambda} = \frac{\partial \mathbf{w}}{\partial \Theta^\Lambda} = \frac{\partial(\tilde{W}^K \mathbf{A}_K)}{\partial \Theta^\Lambda} = \frac{\partial(\tilde{W}_K \mathbf{A}^K)}{\partial \Theta^\Lambda}, \quad \mathbf{w} \in \mathbb{R}^{1 \times 3}$$

or through matrix notations

$$\begin{aligned} \mathbf{w}_{,\Lambda} &= [\mathbf{A}_1 \quad \mathbf{A}_2 \quad \mathbf{A}_3] \begin{bmatrix} \tilde{W}_{,\Lambda}^1 \\ \tilde{W}_{,\Lambda}^2 \\ \tilde{W}_{,\Lambda}^3 \end{bmatrix} + [\mathbf{A}_{1,\Lambda} \quad \mathbf{A}_{2,\Lambda} \quad \mathbf{A}_{3,\Lambda}] \begin{bmatrix} \tilde{W}^1 \\ \tilde{W}^2 \\ \tilde{W}^3 \end{bmatrix} = \\ &= [\mathbf{A}^1 \quad \mathbf{A}^2 \quad \mathbf{A}^3] \begin{bmatrix} \tilde{W}_{1,\Lambda} \\ \tilde{W}_{2,\Lambda} \\ \tilde{W}_{3,\Lambda} \end{bmatrix} + [\mathbf{A}_{,\Lambda}^1 \quad \mathbf{A}_{,\Lambda}^2 \quad \mathbf{A}_{,\Lambda}^3] \begin{bmatrix} \tilde{W}_1 \\ \tilde{W}_2 \\ \tilde{W}_3 \end{bmatrix} \end{aligned}$$

Therefore, dispersion matrix of $\mathbf{w}_{,\Lambda}$ can be obtained by

$$\begin{aligned} D\{\mathbf{w}_{,\Lambda}\} &= [\mathbf{A}_1 \quad \mathbf{A}_2 \quad \mathbf{A}_3] \mathbf{Q}_{\tilde{W}_{,\Lambda}^K} [\mathbf{A}_1 \quad \mathbf{A}_2 \quad \mathbf{A}_3]^T + \\ &+ [\mathbf{A}_{1,\Lambda} \quad \mathbf{A}_{2,\Lambda} \quad \mathbf{A}_{3,\Lambda}] \mathbf{Q}_{\tilde{W}^K} [\mathbf{A}_{1,\Lambda} \quad \mathbf{A}_{2,\Lambda} \quad \mathbf{A}_{3,\Lambda}]^T = \mathbf{Q}_{\mathbf{w}_{,\Lambda}} \end{aligned} \quad (3.6)$$

where we have

$$\tilde{W}^K = \langle \mathbf{u}, \mathbf{A}^K \rangle \Rightarrow D\{\tilde{W}^K\} = [\mathbf{A}^1 \quad \mathbf{A}^2 \quad \mathbf{A}^3] \mathbf{Q}_{\mathbf{w}} [\mathbf{A}^1 \quad \mathbf{A}^2 \quad \mathbf{A}^3]^T = \mathbf{Q}_{\tilde{W}^K}, \quad D\{\tilde{W}^K\} \in \mathbb{R}^{3 \times 3}$$

Correspondent to Eq. (3.6), we can obtain dispersion matrix of \mathbf{w}_Λ through covariant elements

$$\begin{aligned} D\{\mathbf{w}_\Lambda\} &= [\mathbf{A}^1 \ \mathbf{A}^2 \ \mathbf{A}^3] \mathbf{Q}_{\tilde{W}_{K,\Lambda}} [\mathbf{A}^1 \ \mathbf{A}^2 \ \mathbf{A}^3]^T + \\ &+ [\mathbf{A}_{,\Lambda}^1 \ \mathbf{A}_{,\Lambda}^2 \ \mathbf{A}_{,\Lambda}^3] \mathbf{Q}_{\tilde{W}_K} [\mathbf{A}_{,\Lambda}^1 \ \mathbf{A}_{,\Lambda}^2 \ \mathbf{A}_{,\Lambda}^3]^T = \mathbf{Q}_{\mathbf{w}_\Lambda} \end{aligned} \quad (3.7)$$

where

$$\tilde{W}_K = \langle \mathbf{w}, \mathbf{A}_K \rangle \Rightarrow D\{\tilde{W}_K\} = [\mathbf{A}_1 \ \mathbf{A}_2 \ \mathbf{A}_3] \mathbf{Q}_{\mathbf{w}} [\mathbf{A}_1 \ \mathbf{A}_2 \ \mathbf{A}_3]^T = \mathbf{Q}_{\tilde{W}_K}, D\{\tilde{W}_K\} \in \mathbb{R}^{3 \times 3}$$

Hence, using Eqs. (3.6) or (3.7), dispersion matrix of TCC elements can be obtained by

$$\begin{aligned} K_{\Lambda\Phi} &= - \langle \mathbf{w}_\Lambda, \mathbf{A}_\Phi \rangle - \langle \mathbf{w}_\Lambda, \mathbf{u}_\Phi \rangle - \langle \mathbf{u}_\Phi, \mathbf{A}_{3,\Lambda} \rangle \\ D\{\tilde{\mathbf{q}}\} &= \mathbf{T} \begin{bmatrix} \mathbf{Q}_{\mathbf{u},1} & 0 & 0 & 0 \\ 0 & \mathbf{Q}_{\mathbf{u},2} & 0 & 0 \\ 0 & 0 & \mathbf{Q}_{\mathbf{w},1} & 0 \\ 0 & 0 & 0 & \mathbf{Q}_{\mathbf{w},2} \end{bmatrix} \mathbf{T}^T = \mathbf{Q}_{\tilde{\mathbf{q}}}, D\{\tilde{\mathbf{q}}\} \in \mathbb{R}^{3 \times 3} \end{aligned} \quad (3.8)$$

where matrix \mathbf{T} is

$$\mathbf{T} = \begin{bmatrix} \mathbf{A}_{3,1} + \mathbf{w}_{,1} & 0 & \mathbf{A}_1 + \mathbf{u}_{,1} & 0 \\ \frac{1}{2}(\mathbf{A}_{3,2} + \mathbf{w}_{,2}) & \frac{1}{2}(\mathbf{A}_{3,2} + \mathbf{w}_{,2}) & \frac{1}{2}(\mathbf{A}_2 + \mathbf{u}_{,2}) & \frac{1}{2}(\mathbf{A}_1 + \mathbf{u}_{,1}) \\ 0 & \mathbf{A}_{3,2} + \mathbf{w}_{,2} & 0 & \mathbf{A}_2 + \mathbf{u}_{,2} \end{bmatrix}, \mathbf{T} \in \mathbb{R}^{3 \times 12} \quad (3.9)$$

Likewise, vector $\tilde{\mathbf{q}}$ indicates the vector-half form of symmetric curvature tensor

$$\tilde{\mathbf{q}} := \text{vh}(\mathbf{K}_l) = [K_{11} \ K_{12} \ K_{22}]^T \in \mathbb{R}^{3 \times 1}$$

3.3 Error Propagations for Eigenspace Components

In this section we evaluate the dispersion effect of strain- tensor elements and TCC elements, which are obtained through Eqs. (3.5) and (3.8), on their eigenspace components. Due to the intricacy of relations between eigenvalues of strain tensor (or TCC) and their eigenspace components, which are established through Eqs. (2.30)- (2.32) as well (2.68)- (2.6.3), we performed the simultaneous diagonalization of quadratic forms for pairs $\{\mathbf{E}_l, \mathbf{A}_l\}$ and $\{\mathbf{K}_l, \mathbf{A}_l\}$. Summarizing briefly :

$$\begin{aligned} &\mathbf{A}_l \quad \mathbf{E}_l \\ &\quad \downarrow \quad \downarrow \\ (\mathbf{V}_l \mathbf{M})^T \mathbf{A}_l (\mathbf{V}_l \mathbf{M}) &= \mathbf{I} \quad \mathbf{E}_l'' = (\mathbf{V}_l \mathbf{M})^T \mathbf{E}_l (\mathbf{V}_l \mathbf{M}) \end{aligned} \quad (3.10)$$

and

$$\begin{aligned} &\mathbf{A}_l \quad \mathbf{K}_l \\ &\quad \downarrow \quad \downarrow \\ (\mathbf{V}_l \mathbf{M})^T \mathbf{A}_l (\mathbf{V}_l \mathbf{M}) &= \mathbf{I} \quad \mathbf{K}_l'' = (\mathbf{V}_l \mathbf{M})^T \mathbf{K}_l (\mathbf{V}_l \mathbf{M}) \end{aligned} \quad (3.11)$$

where \mathbf{V}_l is the matrix of eigenvectors of metric, and \mathbf{M} is the positive definite matrix (see Eq. (2.4.2)). Hence, without loss of generality, using simultaneous diagonalization we mapped the eigenspectra components of $\{\mathbf{E}_l, \mathbf{A}_l\}$ and $\{\mathbf{K}_l, \mathbf{A}_l\}$ into eigenspectra of $\{\mathbf{E}_l'', \mathbf{I}\}$ and $\{\mathbf{K}_l'', \mathbf{I}\}$, respectively. Namely

$$\begin{array}{ccc}
 \text{Analysis} & \text{vs.} & \text{Synthesis} \\
 \left[\begin{array}{c} \Lambda_1 \\ \Lambda_2 \\ \Theta \end{array} \right] = \frac{1}{2} \left[\begin{array}{c} E''_{11} + E''_{22} + \sqrt{(E''_{11} - E''_{22})^2 + 4E''_{12}{}^2} \\ E''_{11} + E''_{22} - \sqrt{(E''_{11} - E''_{22})^2 + 4E''_{12}{}^2} \\ \arctan \frac{2E''_{12}}{E''_{11} - E''_{22}} \end{array} \right] & \text{vs.} & \left[\begin{array}{c} E''_{11} \\ E''_{12} \\ E''_{22} \end{array} \right] = \left[\begin{array}{c} \Lambda_1 \cos^2 \Theta + \Lambda_2 \sin^2 \Theta \\ \frac{1}{2}(\Lambda_2 - \Lambda_1) \sin 2\Theta \\ \Lambda_1 \sin^2 \Theta + \Lambda_2 \cos^2 \Theta \end{array} \right] \quad (3.12)
 \end{array}$$

and

$$\begin{array}{ccc}
 \text{Analysis} & \text{vs.} & \text{Synthesis} \\
 \left[\begin{array}{c} \Lambda'_1 \\ \Lambda'_2 \\ \Theta' \end{array} \right] = \frac{1}{2} \left[\begin{array}{c} K''_{11} + K''_{22} + \sqrt{(K''_{11} - K''_{22})^2 + 4K''_{12}{}^2} \\ K''_{11} + K''_{22} - \sqrt{(K''_{11} - K''_{22})^2 + 4K''_{12}{}^2} \\ \arctan \frac{2K''_{12}}{K''_{11} - K''_{22}} \end{array} \right] & \text{vs.} & \left[\begin{array}{c} K''_{11} \\ K''_{12} \\ K''_{22} \end{array} \right] = \left[\begin{array}{c} \Lambda'_1 \cos^2 \Theta' + \Lambda'_2 \sin^2 \Theta' \\ \frac{1}{2}(\Lambda'_2 - \Lambda'_1) \sin 2\Theta' \\ \Lambda'_1 \sin^2 \Theta' + \Lambda'_2 \cos^2 \Theta' \end{array} \right] \quad (3.13)
 \end{array}$$

where $\{\Lambda_1, \Lambda_2\}$ are eigenvalues of \mathbf{E}_l'' with related orientation parameter Θ , although $\{\Lambda'_1, \Lambda'_2\}$ are eigenvalues of \mathbf{K}_l'' with related orientation parameter Θ' .

Hence, considering the dispersion matrices of vector-half forms of \mathbf{E}_l and \mathbf{K}_l on one side (see Eqs. (3.5) and (3.8)) and transformed matrices (via simultaneously diagonalization) on the other side (see Eqs. (3.10) and (3.11)), we can obtain the dispersion matrices of elements of transformed matrices in terms of dispersion matrices of strain tensor and TCC, respectively. Namely

$$D \left\{ \left[\begin{array}{c} E''_{11} \\ E''_{12} \\ E''_{22} \end{array} \right] \right\} = \left[\begin{array}{ccc} S_{11}^2 & 2S_{11}S_{21} & S_{21}^2 \\ S_{11}S_{12} & S_{11}S_{22} + S_{12}S_{21} & S_{21}S_{22} \\ S_{12}^2 & 2S_{12}S_{22} & S_{22}^2 \end{array} \right] \mathbf{Q}_{\tilde{\mathbf{p}}} \left[\begin{array}{ccc} S_{11}^2 & 2S_{11}S_{21} & S_{21}^2 \\ S_{11}S_{12} & S_{11}S_{22} + S_{12}S_{21} & S_{21}S_{22} \\ S_{12}^2 & 2S_{12}S_{22} & S_{22}^2 \end{array} \right]^T \quad (3.14)$$

and

$$D \left\{ \left[\begin{array}{c} K''_{11} \\ K''_{12} \\ K''_{22} \end{array} \right] \right\} = \left[\begin{array}{ccc} S_{11}^2 & 2S_{11}S_{21} & S_{21}^2 \\ S_{11}S_{12} & S_{11}S_{22} + S_{12}S_{21} & S_{21}S_{22} \\ S_{12}^2 & 2S_{12}S_{22} & S_{22}^2 \end{array} \right] \mathbf{Q}_{\tilde{\mathbf{q}}} \left[\begin{array}{ccc} S_{11}^2 & 2S_{11}S_{21} & S_{21}^2 \\ S_{11}S_{12} & S_{11}S_{22} + S_{12}S_{21} & S_{21}S_{22} \\ S_{12}^2 & 2S_{12}S_{22} & S_{22}^2 \end{array} \right]^T \quad (3.15)$$

where

$$\mathbf{S} = \begin{bmatrix} S_{11} & S_{12} \\ S_{21} & S_{22} \end{bmatrix} \text{ subject to } \mathbf{S} = \mathbf{V}_l \mathbf{M}$$

Our aim was the computing of dispersion matrices of eigenvalues of strain tensor and TCC. It can be obtained by propagating dispersion matrices (3.14) and (3.15) into their eigenvalues through the right sides of Eqs.(3.12) and (3.13). However, due to the nonlinearity of equations, propagation of dispersion matrices into eigenvalues will need linearization in equations, which following subsection covers.

3.3.1 Setup of Linear Observation Model

This section is devoted to :

- i. Linearization of the nonlinear equation between elements of transformed matrix (\mathbf{E}_l'') and its eigenspace components, which has already been established by Eq. (3.12). In this case we set up an observation model based on a linearized model under the sampling eigenspace synthesis.
- ii. Establishing linearized observation equations for n samples of *independent* random vectors from transformed tensor elements (under the normal distribution assumption), each with an individual variance matrix. Then we *estimate* the eigenspace component and dispersion matrix of eigenspace component.

Let us start this section by recalling the vector-half form of symmetric matrix $\mathbf{E}_{l,i}''$ which could be represented as [Xu and Grafarend, 1996a,b]

$$\mathbf{y}_i'' := \text{vh}(\mathbf{E}_{l,i}'') = \begin{bmatrix} E_{11,i}'' \\ E_{12,i}'' \\ E_{22,i}'' \end{bmatrix} = \begin{bmatrix} \Lambda_{1,i} \cos^2 \Theta + \Lambda_{2,i} \sin^2 \Theta \\ \frac{1}{2}(\Lambda_{2,i} - \Lambda_{1,i}) \sin 2\Theta \\ \Lambda_{1,i} \sin^2 \Theta + \Lambda_{2,i} \cos^2 \Theta \end{bmatrix}, \quad \mathbf{y}_i'' \in \mathbb{R}^{3 \times 1}$$

with the first- and second moments

$$E\{\mathbf{y}_i''\} = E \left\{ \begin{bmatrix} E_{11,i}'' \\ E_{12,i}'' \\ E_{22,i}'' \end{bmatrix} \right\}, \quad D\{\mathbf{y}_i''\} = D \left\{ \begin{bmatrix} E_{11,i}'' \\ E_{12,i}'' \\ E_{22,i}'' \end{bmatrix} \right\} = \mathbf{Q}_{\mathbf{y}_i''}$$

where second moments can be obtained by Eq.(3.14).

Suppose that n samples of \mathbf{E}_l'' , namely $\mathbf{E}_{l,1}'', \mathbf{E}_{l,2}'', \dots, \mathbf{E}_{l,n}''$ have been observed, where vector-half forms of them are $\mathbf{y}_1'', \mathbf{y}_2'', \dots, \mathbf{y}_n''$. Then we can design an array of vector-half forms of $y_{1,i}'' = E_{11,i}'', y_{2,i}'' = E_{12,i}'',$ and $y_{3,i}'' = E_{22,i}''$ indexed to the number of samples. Namely by

$$\mathbf{Y}'' = [\mathbf{y}_1'', \mathbf{y}_2'', \dots, \mathbf{y}_n''] = \begin{bmatrix} y_{1,1}'' & \dots & y_{1,n}'' \\ y_{2,1}'' & \dots & y_{2,n}'' \\ y_{3,1}'' & \dots & y_{3,n}'' \end{bmatrix}, \quad \mathbf{Y}'' \in \mathbb{R}^{3 \times n} \quad (3.16)$$

with the first- and second moments

$$E\{\mathbf{Y}''\} = E\{[\mathbf{y}_1'' \ \mathbf{y}_2'' \ \dots \ \mathbf{y}_n'']\} \ , \ E\{\mathbf{Y}''\} \in \mathbb{R}^{3 \times n}$$

$$D\{\text{vec}(\mathbf{Y}'')\} = \begin{bmatrix} \mathbf{Q}_{\mathbf{y}_1''} & 0 & \dots & 0 \\ 0 & \mathbf{Q}_{\mathbf{y}_2''} & \dots & 0 \\ \vdots & \vdots & \ddots & \vdots \\ 0 & 0 & \dots & \mathbf{Q}_{\mathbf{y}_n''} \end{bmatrix} \ , \ D\{\text{vec}(\mathbf{Y}'')\} = \mathbf{Q}_{\text{vec}(\mathbf{Y}'')} \in \mathbb{R}^{3n \times 3n} \quad (3.17)$$

where $\mathbf{y}_1'' \ \mathbf{y}_2'' \ \dots \ \mathbf{y}_n''$ are considered independent 3×1 random vectors, each with the 3×3 variance matrix $\mathbf{Q}_{\mathbf{y}_i''}$.

Remark 3.2 Definition (vec-operator): In mathematics, especially in linear algebra and matrix theory, the vectorization of a matrix is a linear transformation which converts the matrix into a column vector. Specifically, the vectorization of an mn matrix \mathbf{A} , denoted by $\text{vec}(\mathbf{A})$, is the $mn \times 1$ column vector obtained by stacking the columns of the matrix \mathbf{A} on top of one another: $\text{vec}(\mathbf{A}) = [A_{11}, \dots, A_{m1}, A_{12}, \dots, A_{m2}, \dots, A_{1n}, \dots, A_{mn}]^T$. For example, for the 2×2 matrix $\mathbf{A} = \begin{bmatrix} A_{11} & A_{12} \\ A_{21} & A_{22} \end{bmatrix}$, the vectorization is $\text{vec}(\mathbf{A}) = [A_{11} \ A_{12} \ A_{21} \ A_{22}]$.

Let us consider a special nonlinear multivariate *Gauss- Markov* model for sampling the eigenspace synthesis [Cai, 2004]

$$\mathbf{Y}'' = \mathbf{F}(\xi)\mathbf{1}^T + \mathbf{V}_{\mathbf{Y}''} \quad (3.18)$$

where $\mathbf{1}$ denotes the $n \times 1$ "summation vector" consisting of ones and

$$\mathbf{F} := \begin{bmatrix} f_1 \\ f_2 \\ f_3 \end{bmatrix} = \begin{bmatrix} \Lambda_1 \cos^2 \Theta + \Lambda_2 \sin^2 \Theta \\ \frac{1}{2}(\Lambda_2 - \Lambda_1) \sin 2\Theta \\ \Lambda_1 \sin^2 \Theta + \Lambda_2 \cos^2 \Theta \end{bmatrix} = \begin{bmatrix} \xi_1 \cos^2 \xi_3 + \xi_2 \sin^2 \xi_3 \\ \frac{1}{2}(\xi_2 - \xi_1) \sin 2\xi_3 \\ \xi_1 \sin^2 \xi_3 + \xi_2 \cos^2 \xi_3 \end{bmatrix} \quad (3.19)$$

where

$$\begin{bmatrix} \xi_1 \\ \xi_2 \\ \xi_3 \end{bmatrix} := \begin{bmatrix} \Lambda_1 \\ \Lambda_2 \\ \Theta \end{bmatrix} \ , \ \begin{bmatrix} f_1 \\ f_2 \\ f_3 \end{bmatrix} := \begin{bmatrix} E''_{11} \\ E''_{12} \\ E''_{22} \end{bmatrix}$$

Moreover, parameters ξ , $E\{\mathbf{Y}''\}$ and $\mathbf{Y}'' - E\{\mathbf{Y}''\} = \mathbf{V}_{\mathbf{Y}''}$ are unknown. Hence, by the Taylor series linearization of nonlinear model Eq. (3.4), up to order one

$$\mathbf{F}(\xi) = \mathbf{F}(\xi_0) + \mathbf{J}(\xi_0)(\xi - \xi_0) + O[(\xi - \xi_0) \otimes (\xi - \xi_0)] \quad (3.20)$$

where \otimes denotes to Kronecker-Zehfuss product [Grafarend, 2004]. For the first set of observations $[y''_{1.1} \ y''_{2.1} \ y''_{3.1}]^T = [E''_{11.1} \ E''_{21.1} \ E''_{22.1}]^T$ we have

$$\xi_0 := \begin{bmatrix} \Lambda_{1.1} \\ \Lambda_{2.1} \\ \Theta_{.1} \end{bmatrix} = \frac{1}{2} \begin{bmatrix} E''_{11.1} + E''_{22.1} + \sqrt{(E''_{11.1} - E''_{22.1})^2 + 4E''_{21.1}{}^2} \\ E''_{11.1} + E''_{22.1} - \sqrt{(E''_{11.1} - E''_{22.1})^2 + 4E''_{21.1}{}^2} \\ \arctan \frac{2E''_{21.1}}{E''_{11.1} - E''_{22.1}} \end{bmatrix} \quad (3.21)$$

and the Jacobi matrix is

$$\mathbf{J}(\xi_0) = \begin{bmatrix} \frac{\partial f_1}{\partial \Lambda_1} & \frac{\partial f_1}{\partial \Lambda_2} & \frac{\partial f_1}{\partial \Theta} \\ \frac{\partial f_2}{\partial \Lambda_1} & \frac{\partial f_2}{\partial \Lambda_2} & \frac{\partial f_2}{\partial \Theta} \\ \frac{\partial f_3}{\partial \Lambda_1} & \frac{\partial f_3}{\partial \Lambda_2} & \frac{\partial f_3}{\partial \Theta} \end{bmatrix}_{\xi=\xi_0} = \begin{bmatrix} \cos^2 \Theta_{.1} & \sin^2 \Theta_{.1} & (\Lambda_{2.1} - \Lambda_{1.1}) \sin 2\Theta_{.1} \\ \frac{1}{2} \sin 2\Theta_{.1} & -\frac{1}{2} \sin 2\Theta_{.1} & -(\Lambda_{2.1} - \Lambda_{1.1}) \cos 2\Theta_{.1} \\ \sin^2 \Theta_{.1} & \cos^2 \Theta_{.1} & -(\Lambda_{2.1} - \Lambda_{1.1}) \sin 2\Theta_{.1} \end{bmatrix}$$

The above results are based on the assumption of using the Taylor series linearization, then we will apply the *Gauss-Newton* iteration scheme with an initial point ξ_0 . The term ξ_0 is determined by solving once the eigenvalue analysis through the Eq. (3.21) for the first sample. Based on Eq. (3.20) we establish a special linearized multivariate Gauss- Markov model for the eigenspace synthesis

$$\mathbf{Y}'' = \mathbf{F}(\xi_0)\mathbf{1}^T + [\mathbf{J}(\xi_0)\Delta\xi]\mathbf{1}^T + \mathbf{V}_{\mathbf{Y}''} \quad (3.22)$$

which in vectorized form is

$$\text{vec}(\mathbf{Y}'') = \text{vec}(\mathbf{Y}''_0) + \mathbf{A}\Delta\xi + \text{vec}(\mathbf{V}_{\mathbf{Y}''}) \ , \ \mathbf{A} = [\mathbf{1} \otimes \mathbf{J}(\xi_0)] \quad (3.23)$$

$$\text{vec}(\mathbf{Y}''_0) = \mathbf{1} \otimes \mathbf{F}(\xi_0) \quad (3.24)$$

First moments :

$$E\{\text{vec}(\mathbf{Y}'')\} = \mathbf{A}\Delta\xi + \text{vec}(\mathbf{Y}''_0) \ , \ \text{vec}(\mathbf{Y}'') \in \mathbb{R}^{3n \times 1}$$

Second moments :

$$D\{\text{vec}(\mathbf{Y}'')\} = \mathbf{Q}_{\text{vec}(\mathbf{Y}'')} \ , \ \text{rank } \mathbf{Q}_{\text{vec}(\mathbf{Y}'')} = 3n$$

With the assumption of observation of random tensors, we will estimate the eigenvalue components ξ of the type "Best Linear Uniformly Unbiased Estimator" (Σ - BLUUE) in the special linearized multivariate Gauss- Markov model [Grafarend, 2006]

$$\Delta\hat{\xi} = \hat{\xi} - \xi_0 = \mathbf{L}(\text{vec}(\mathbf{Y}) - \text{vec}(\mathbf{Y}'')) = (\mathbf{A}^T \mathbf{Q}_{\text{vec}(\mathbf{Y}'')}^{-1} \mathbf{A})^{-1} \mathbf{A}^T \mathbf{Q}_{\text{vec}(\mathbf{Y}'')}^{-1} (\text{vec}(\mathbf{Y}) - \text{vec}(\mathbf{Y}'')) \quad (3.25)$$

subjected to the related dispersion matrix

$$D\{\hat{\xi}\} = (\mathbf{A}^T \mathbf{Q}_{\text{vec}(\mathbf{Y}'')} \mathbf{A})^{-1} = \mathbf{Q}_{\hat{\xi}} \quad (3.26)$$

Then, estimated residual vectors and observations are:

$$\text{vec}(\hat{\mathbf{Y}}'') = \mathbf{A}(\mathbf{A}^T \mathbf{Q}_{\text{vec}(\mathbf{Y}'')}^{-1} \mathbf{A})^{-1} \mathbf{A}^T \mathbf{Q}_{\text{vec}(\mathbf{Y}'')}^{-1} \text{vec}(\mathbf{Y}'') \quad (3.27)$$

$$\text{vec}(\hat{\mathbf{V}}_{\mathbf{Y}''}) = \text{vec}(\mathbf{Y}'') - \text{vec}(\hat{\mathbf{Y}}'') = \mathbf{D}_{(\sigma)} \text{vec}(\mathbf{Y}'') \quad (3.28)$$

$$\mathbf{D}_{(\sigma)} = (\mathbf{I} - \mathbf{A}(\mathbf{A}^T \mathbf{Q}_{\text{vec}(\mathbf{Y}'')}^{-1} \mathbf{A})^{-1} \mathbf{A}^T \mathbf{Q}_{\text{vec}(\mathbf{Y}'')}^{-1}) \quad (3.29)$$

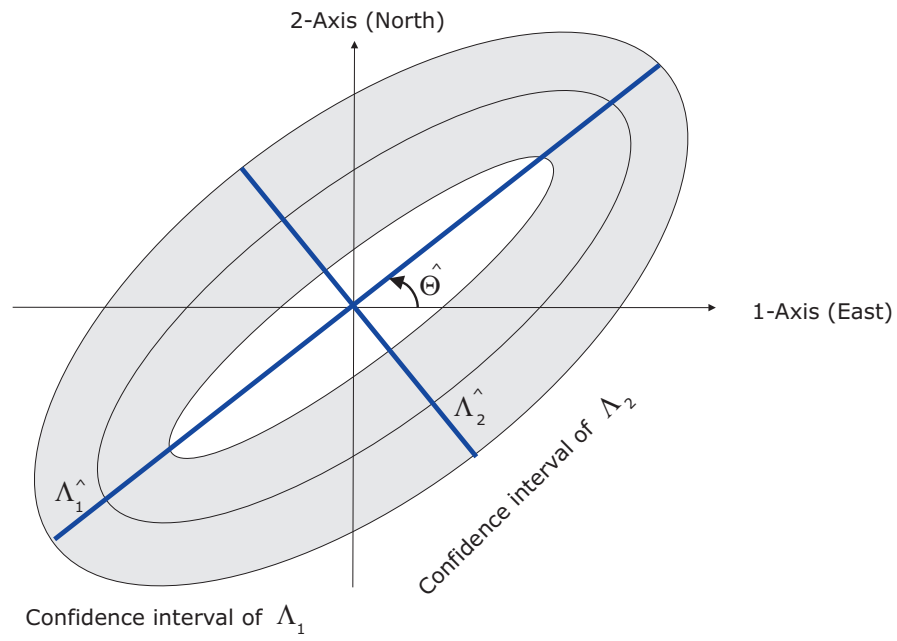
However, an estimation of eigenspace components TCC and their dispersion matrix can be performed in a similar approach, while the dispersion matrix of tensor elements can be obtained by Eq. (3.15) .

Hence, by the estimation of eigenspace components of random deformation tensors and their dispersion matrices, we are able to start the statistical validation of eigenspace components based upon the assumption of a *Gauss- Laplace* normal distribution of the observed (or derived) deformation tensor elements.

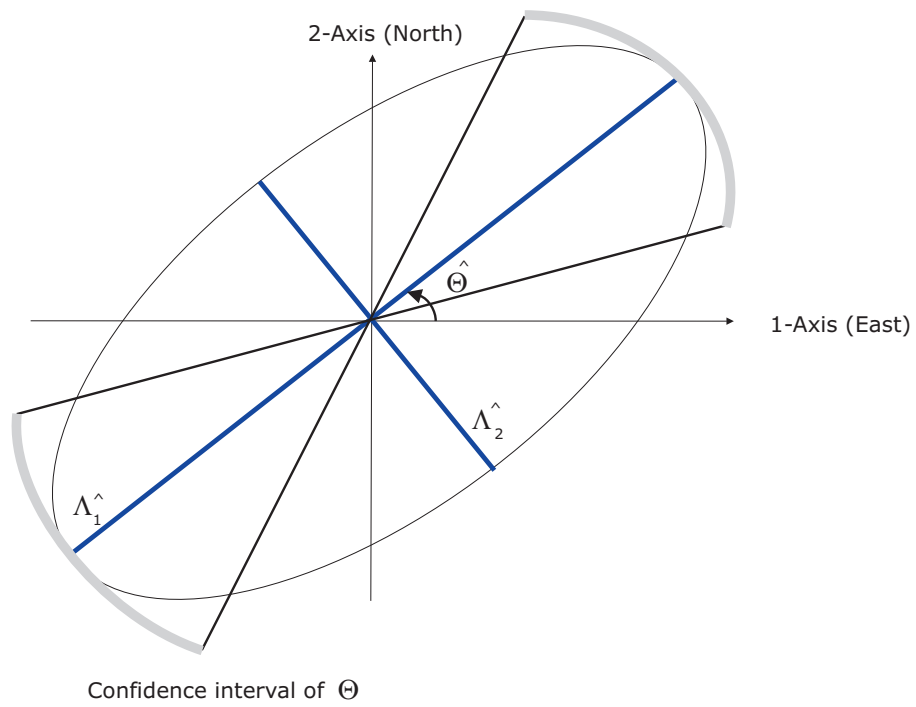
Remark 3.3 Two sets of statistical tests are performed for testing results :

- i. Multivariate test for all eigenspace components : tests for eigenspace parameter $\xi = \xi_0$ with estimated covariance matrix $\mathbf{Q}_{\hat{\xi}}$. The quadratic form $\phi = (\hat{\xi} - \xi_0)^T \mathbf{Q}_{\hat{\xi}}^{-1} (\hat{\xi} - \xi_0)$ represents an equation of ellipsoidal, centered at $\hat{\xi}$. Its distribution can be approximated by Fisher's distribution : $(\hat{\xi} - \xi_0)^T \mathbf{Q}_{\hat{\xi}}^{-1} (\hat{\xi} - \xi_0) \sim \frac{3}{n-3} F_{3,n-3}$ and hypothesis test can be performed using the tabulated F values. For example, for $H_0 : \xi = \xi_0$ vs $H_1 : \xi \neq \xi_0$ we would reject H_0 if computed ϕ exceeds $\frac{3}{n-3} F_{\alpha,3,n-3}$ at the α level of significancy [Mikhail and Ackermann, 1976, page 299].
- ii. Test for a distinct element of eigenspace components : Let us consider diagonal elements of estimated covariance matrix $Q_{\hat{\xi}}$ with $\hat{\sigma}_1^2, \hat{\sigma}_2^2, \hat{\sigma}_3^2$ as estimated variances for Λ_1, Λ_2 and Θ , respectively. Separate tests about the eigenspace components in $\xi_0 = [\Lambda_{1,1} \ \Lambda_{2,1} \ \Theta_{,1}]^T$ with associated statistics : $t_1 = \frac{\hat{\Lambda}_1 - \Lambda_{1,1}}{\hat{\sigma}_1}$, $t_2 = \frac{\hat{\Lambda}_2 - \Lambda_{2,1}}{\hat{\sigma}_2}$ and $t_3 = \frac{\hat{\Theta} - \Theta_{,1}}{\hat{\sigma}_3}$ can be performed. Under the null hypothesis, these statistics follow t -distributions with $n - 1$ degrees of freedom.

Therefore, α confidence intervals for the eigenvalues and orientation parameter of semi-major axis could be obtainable through the estimated values and suitable statistical tests (see Fig. 3.1).



(a)



(b)

Figure 3.1: (a) The α confidence intervals for the eigenvalues Λ_1 and Λ_2 . (b) The α confidence intervals for the eigen-direction Θ .

3.4 Variance-Covariance Estimation of Helmert type

The eigenspace components are typically processed using the least-squares method (e.g., which we have performed in the previous section). To obtain reliable least-squares estimates, however, both the functional model and the stochastic model must be adequately defined. In the previous section we developed a functional model between the transformed strain tensor or TCC obtained by simultaneous diagonalization (such as observations), and eigenspace components (unknowns). We used n samples of *independent* 3×1 random vectors $\mathbf{y}_1'', \mathbf{y}_2'', \dots, \mathbf{y}_n''$, each with the 3×3 variance covariance matrix $\mathbf{Q}_{\mathbf{y}_i''}$.

Hence, the covariance matrix of observations (components of transferred tensors) is partly known, and incomplete knowledge of the covariance matrix of the observations may lead to unreliable results. An appropriate statistical model is needed to arrive at a proper description of the estimator quality. Methods for estimating covariance components have been intensively investigated in the statistical and geodetic literatures (e.g., Helmert [1907]; Grafarend et al. [1980]; Hartung [1981]; Persson [1981]; Grafarend [1984]; Malley [1986]; Rao and Kleffe [1988]; Rao [1997]; Satirapod et al. [2001]). The PhD Thesis of Shaffrin [1983] gives a critical review of a state-of-the-art in (co)variance component estimation.

Let us consider the special linearized multivariate Gauss- Markov model with n measurements and three unknowns, which is established in the previous section (Eqs. (3.23)) :

$$\text{vec}(\mathbf{Y}'') = \text{vec}(\mathbf{Y}_0'') + \mathbf{A}\Delta\xi + \text{vec}(\mathbf{V}_{\mathbf{Y}''})$$

where $\text{vec}(\mathbf{Y}'') \in \mathbb{R}^{3n \times 1}$ and $\mathbf{V}_{\mathbf{Y}''} \in \mathbb{R}^{3n \times 1}$ are the vector measurements (of the random tensor) and residuals, respectively; $\mathbf{A} = [\mathbf{1} \otimes \mathbf{J}(\xi_0)] \in \mathbb{R}^{3n \times 3}$ is the design matrix; $\text{vec}(\mathbf{Y}_0'') = [\mathbf{1} \otimes \mathbf{F}(\xi_0)] \in \mathbb{R}^{3n \times 1}$ is the vectorized version of tensor values at evaluation point ξ_0 ; $\Delta\xi \in \mathbb{R}^{3n \times 1}$ is a vector of unknowns.

Partitioning the full covariance matrix of measurements into p groups of matrices by

$$D\{\text{vec}(\mathbf{Y}'')\} = \sum_{j=1}^{\bar{p}} \mathbf{Q}_{jj} \sigma_j^2 + \sum_{j=1}^{\bar{p}-1} \sum_{k=j+1}^{\bar{p}} \mathbf{Q}_{jk} \sigma_{jk} = \begin{bmatrix} \sigma_1^2 \mathbf{Q}_{11} & \sigma_{12} \mathbf{Q}_{12} & \dots & \sigma_{1\bar{p}} \mathbf{Q}_{1\bar{p}} \\ \sigma_{12} \mathbf{Q}_{12}^T & \sigma_2^2 \mathbf{Q}_{22} & \dots & \sigma_{2\bar{p}} \mathbf{Q}_{2\bar{p}} \\ \vdots & \vdots & \ddots & \vdots \\ \sigma_{1\bar{p}} \mathbf{Q}_{1\bar{p}}^T & \sigma_{2\bar{p}} \mathbf{Q}_{2\bar{p}}^T & \dots & \sigma_{\bar{p}}^2 \mathbf{Q}_{\bar{p}\bar{p}} \end{bmatrix} = \mathbf{Q}_{\text{vec}(\mathbf{Y}'')} \in \mathbb{R}^{3n \times 3n} \quad (3.30)$$

with $p = \frac{\bar{p}(\bar{p}+1)}{2}$ variance and covariance components. Here, we assumed that symmetric matrix \mathbf{Q}_{jk} is known and has order $3n \times 3n$. We can design an array consisting of matrices \mathbf{Q}_{jk} by

$$\begin{aligned} \mathbf{Q} &:= [\mathbf{Q}_{11} \quad \mathbf{Q}_{12} \quad \mathbf{Q}_{22} \quad \mathbf{Q}_{13} \quad \mathbf{Q}_{23} \quad \mathbf{Q}_{33} \quad \dots \quad \mathbf{Q}_{\bar{p}-1\bar{p}} \quad \mathbf{Q}_{\bar{p}\bar{p}}] \\ &= [\mathbf{Q}_1 \quad \mathbf{Q}_2 \quad \dots \quad \mathbf{Q}_p] \end{aligned} \quad (3.31)$$

in which $D\{\text{vec}(\mathbf{Y}'')\}$ is positive definite and its diagonal elements *priority* are given (e.g., by Eq. (3.17)). We consider that \bar{p} second moments σ_j^2 of type variance and the $\frac{\bar{p}(\bar{p}-1)}{2}$ second moments of type covariance are unknown, which are collected in the array

$$\sigma = [\sigma_1^2 \quad \sigma_{12} \quad \sigma_2^2 \quad \sigma_{13} \quad \sigma_{23} \quad \sigma_3^2 \quad \dots \quad \sigma_{\bar{p}-1\bar{p}} \quad \sigma_{\bar{p}}^2]^T \quad (3.32)$$

Then, Eq.(3.30), will be represented by

$$\mathbf{Q}_{\text{vec}(\mathbf{Y}'')} = \sum_{j=1}^p \mathbf{Q}_j \sigma_j$$

Now, let us set up an estimator of Helmert type [Helmert, 1907], based upon the idea that least squares residuals $\text{vec}(\hat{\mathbf{V}}_{\mathbf{Y}''})$ are invariant with respect to the transformation $\text{vec}(\mathbf{Y}'') \rightarrow \text{vec}(\mathbf{Y}'') + \mathbf{A}\xi$. The shifting variate is the squared norm of the least-squares residuals. Its expectation, through Eqs.(3.27), can be given as

$$\begin{aligned} E\{\text{vec}(\hat{\mathbf{V}}_{\mathbf{Y}''})^T \mathbf{Q}_{\text{vec}(\mathbf{Y}'')}^{-1} \text{vec}(\mathbf{V}_{\mathbf{Y}''})\} &= E\{\text{vec}(\mathbf{V}_{\mathbf{Y}''})^T \mathbf{D}_{(\sigma)}^T \mathbf{Q}_{\text{vec}(\mathbf{Y}'')}^{-1} \mathbf{D}_{(\sigma)} \text{vec}(\mathbf{V}_{\mathbf{Y}''})\} = \\ &= \text{tr}(\mathbf{D}_{(\sigma)}^T \mathbf{Q}_{\text{vec}(\mathbf{Y}'')}^{-1} \mathbf{D}_{(\sigma)} \mathbf{Q}_{\text{vec}(\mathbf{Y}'')}) \end{aligned}$$

Grafarend et al. [1980] used a block-structured covariance matrix: $\mathbf{Q}_{\text{vec}(\mathbf{Y}'')} = \sum_{j=1}^p \mathbf{Q}_j \sigma_j$ with the multinomial inverse of the form : $\mathbf{Q}_{\text{vec}(\mathbf{Y}'')}^{-1} = \sum_{i=1}^p \mathbf{K}_i \sigma_i$. He gave a simple example how to obtain \mathbf{K}_i 's. When the covariance matrix $D\{\text{vec}(\mathbf{Y}'')\}$ has a block-diagonal structure one can also simply obtain \mathbf{K}_i 's. Substituting these two terms in the proceeding equation yields

$$\sum_{i=1}^p E\{\text{vec}(\hat{\mathbf{V}}_{\mathbf{Y}''})^T \mathbf{K}_i \text{vec}(\hat{\mathbf{V}}_{\mathbf{Y}''})\} = \sum_{i=1}^p \sum_{j=1}^p \text{tr}(\mathbf{D}_{(\sigma)}^T \mathbf{K}_i \mathbf{D}_{(\sigma)} \sigma_j \mathbf{Q}_j)$$

From the expectation of the i^{th} term one obtains

$$E\{\text{vec}(\hat{\mathbf{V}}_{\mathbf{Y}''})^T \mathbf{K}_i \text{vec}(\hat{\mathbf{V}}_{\mathbf{Y}''})\} = \sum_{j=1}^p \text{tr}(\mathbf{D}_{(\sigma)}^T \mathbf{K}_i \mathbf{D}_{(\sigma)} \mathbf{Q}_j) \sigma_j \quad , \quad i = 1, \dots, p.$$

The proceeding equation can be written in a compact form as $E\{q\} = H\sigma$ with the $p \times p$ matrix H (Helmert matrix) and p -vector q as

$$h_{ij} = \text{tr}(\mathbf{D}_{(\sigma)}^T \mathbf{K}_i \mathbf{D}_{(\sigma)} \mathbf{Q}_j) \quad , \quad i, j = 1, \dots, p$$

$$q_i = \text{vec}(\hat{\mathbf{V}}_{\mathbf{Y}''})^T \mathbf{K}_i \text{vec}(\hat{\mathbf{V}}_{\mathbf{Y}''})$$

If H is regular, an unbiased estimator of (co)variance components reads

$$\hat{\sigma} = H^{-1}q \quad (3.33)$$

If the Helmert matrix is a regular matrix then it has the block structure and estimated variances are unbiased and invariant [Grafarend et al., 1980; Grafarend, 1984]. However, Crocetto et al. [2000] stated that since the (normal) matrix may not have full rank, the pseudo-inverse can be used to solve

the system. Recently, Xu et al. [2006] extended the estimation of variance components in linear models to that of linear inverse ill-posed problems. The most clearly stated results may be found in Qu [1989] and later in Xu et al. [2007] who found that if $r^2 \geq p$, all the variance and covariance components are estimable, where r is the number of redundant measurements and n the numbers of all measurements.

Remark 3.4 The selection of estimator and appropriate technique should be based on the desired estimator properties, namely translation invariance, unbiasedness, minimum variance, non-negativeness, computational efficiency and fluency of implementation. In some cases, not all of these properties can be retained for a particular estimator. A prevalent example can be found in Hartung [1981], where the property of unbiasedness was sacrificed for a guaranteed estimation of non-negative variances. In Persson [1981], the existence of simultaneous non-negative estimates of variance components was investigated and it was demonstrated that one reason for a non-negative minimum norm of quadratic unbiased estimators is limited knowledge of the magnitude of the variance components. Another relevant reason, probably, is that the assumed variance component model is not correct or the observation vector contains gross errors. In a realistic model with a large number of degree of freedom negative estimates seldom occur.

In general, the decisions which estimator properties to retain must be made on a case-by-case basis depending on the data and the specific application. The over-riding property that is usually sought after is computational efficiency, which arises due to the massive quantities of data that are used for the estimation of many (co)variance components. In fact, the main criticism of traditional (co)variance estimation, VCE, methods is that they involve repeated inversions of large matrices, intensive computational efforts and large storage requirements for lots of unknowns. For these reasons, one may opt for entirely different estimation procedures. In other cases, mathematical manipulations or simplifications are made to the rigorous algorithm in order to reduce the computational burden involved with inverting large dimensional matrices [Satirapod et al., 2001].

3.5 A Numerical Example

In this section, the proposed methodology (in this chapter) is illustrated using a real data set. It is performed under the normal distribution assumption of tensor measurements (strain and TCC). Moreover, we present a numerical solution of the statistical induction of eigenspace components.

The geodynamic setting of the Cascadia Subduction Zone (CSZ) is briefly reviewed in this section. In addition, we investigate the network of permanent GPS stations covering our study area, called PANGA (Pacific Northwest Geodetic Array), which carries information in the observed horizontal and vertical displacements. Hence, we illustrate the patterns of the eigenspace components associated with random deformation tensors (strain and TCC) based on both the a-priori variance component information and a posteriori variance information of tensor measurements.

3.5.1 Tectonic Setting of the Cascadia Subduction Zone

The Cascadia Subduction Zone (CSZ), located between two migrating triple junctions, deforms in response to superimposed forces of North America, Juan de Fuca, and Pacific boundary interactions which is illustrated by Fig. 3.2. It is generally accepted that a potential megathrust earthquakes would be the result of a slip on a locked portion of the subduction interface, although the size and location of the seismogenic zone is unclear [Verdonck, 2005].

This area is known to be one of the most seismically active areas in western Canada and on the northwest Pacific coast of North America. There is strong evidence supporting the claim that major megathrust earthquakes repeatedly occurred throughout history in this region [Chen, 1998]. To help assess the potential major earthquake hazard and study the tectonic mechanisms in the region, many geodetic measurements have been conducted in the past, ranging from conventional techniques to GPS. These measurements, combined with theoretical deformation models, provide the means and foundation for earthquake studies.

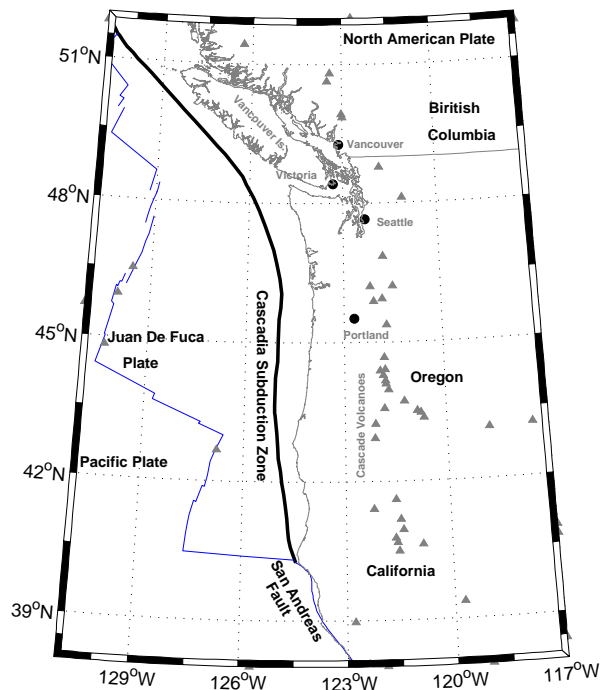


Figure 3.2: Tectonic map of the Cascadia Subduction Zone. The figure is illustrated in Albers equal-area conic projection.

Geodetic, GPS, and strain data provide evidence for active crustal strain build up throughout the region. Based on the models of crustal deformation, the potential for an earthquake with magnitude 9 event has been suggested [Hyndman, 1995]. Historically, as inferred from paleoseismicity data, major megathrust earthquakes have occurred on the Cascadia margin at irregular intervals ranging from 300 to 600 years, most recently about 300 years ago [Meghan-Miller et al., 2001].

However, although low-level seismicity is extensive in the entire region and two major ($M_w > 7$) earthquakes have been observed on central Vancouver Island during this century (1918 and 1946), there have been no megathrust earthquakes on the Cascadia margin, not even small ones, during the past 200 year written historical period [Dragert, 1987; Wang et al., 1987]. In a comparison between the Cascadia margin and other convergent margins around the world, Rogers [1988] noted that this unusual lack of seismicity might well imply a potential risk for forthcoming megathrust earthquakes. This being the case, the Cascadia margin has entered the second half of an earthquake cycle or perhaps even has approached the recurrence of the very large event.

Fig. (3.3) illustrates the seismicity map of the in the Pacific Northwest Seismic events with $M_w \geq 3$

from the *Northern California Earthquake Catalog Search* (<http://www.ncedc.org/ncedc/catalog-search.html>) during 1969 to 2006 which are scaled by magnitude.

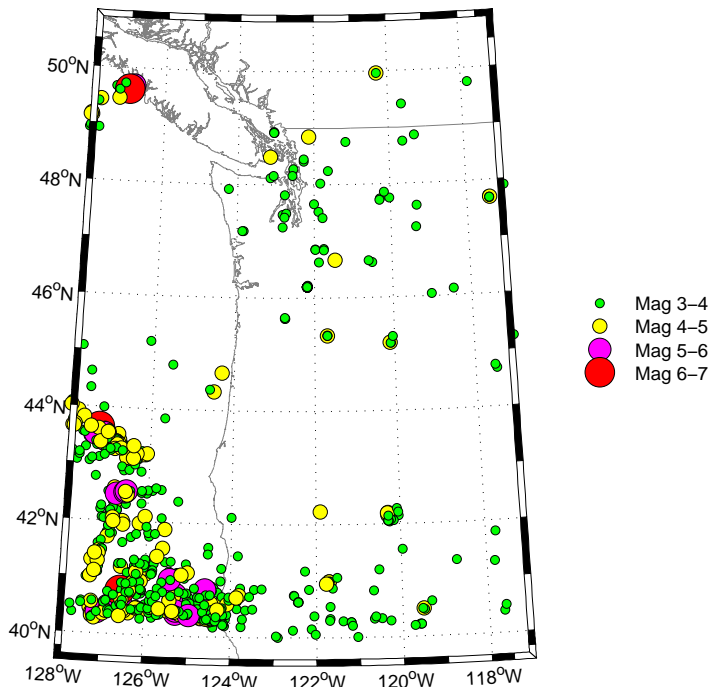


Figure 3.3: Pacific Northwest seismic events with $M \geq 3$ from the Northern California Earthquake Catalog Search (1969 to 2006) which are scaled by magnitude. The figure is illustrated in Albers equal-area conic projection.

3.5.2 GPS Arrays

GPS measurements to determine crustal strain rates were initiated in the Cascadia region (US Pacific Northwest and south-western British Columbia, Canada) more than a decade ago, with the first campaign measurements in 1986 [Kleusberg et al., 1988] and the establishment of permanent stations in 1991 [Dragert et al., 1994, 1995].

Nowadays, continuous GPS data from the Pacific Northwest Geodetic Array is processed by the geodesy laboratory (at Central Washington University Research), which serves as the data analysis facility for the Pacific Northwest Geodetic Array (PANGA). This organization has deployed an extensive network of continuous GPS sites aim to measure crustal deformation along the CSZ. Considered network includes 33 permanent GPS stations, which have nearly daily solutions through the period January 1996 to January 2006. The current network of stations along CSZ area is illustrated through Fig. (3.4).

Fig. (3.5) illustrates the horizontal velocity field along the Cascadia margin assuming a stable North American plate. Continuous GPS results in the Pacific Northwest provide a remarkably coherent view of along-strike variation in Cascadia margin deformation, which is characterized by different tectonic domains. Coastal stations in the northern and central parts of the margin are strongly entrained in the

JDF-North America convergence direction, although the northward component of station velocities increases from north to south. Inland stations show smaller motions; consistent with their structural domains from south to north while the California- southern Oregon boundary reflects a composite velocity model.

Fig. (3.6) illustrates the estimated rates of vertical deformation (i.e., after removing the seasonal variation) throughout the CSZ, which is derived from the GPS arrays. The vertical deformation rate varies significantly along the coast with the highest deformation occurring to the north. At latitude 45°N , there is little vertical deformation at either the coast or inland. The lack of the vertical deformation across central Oregon represent a transition in subduction behavior between northern and southern segments [Verdonck, 2004]. In addition, the pattern of the vertical deformation, which is derived from permanent GPS in the period of 1996-2006, is consistent with vertical crustal deformation from leveling data by [Verdonck, 2004]. There are some minor differences, which seem to be related to lack of dense networks of permanent GPS stations in that area.

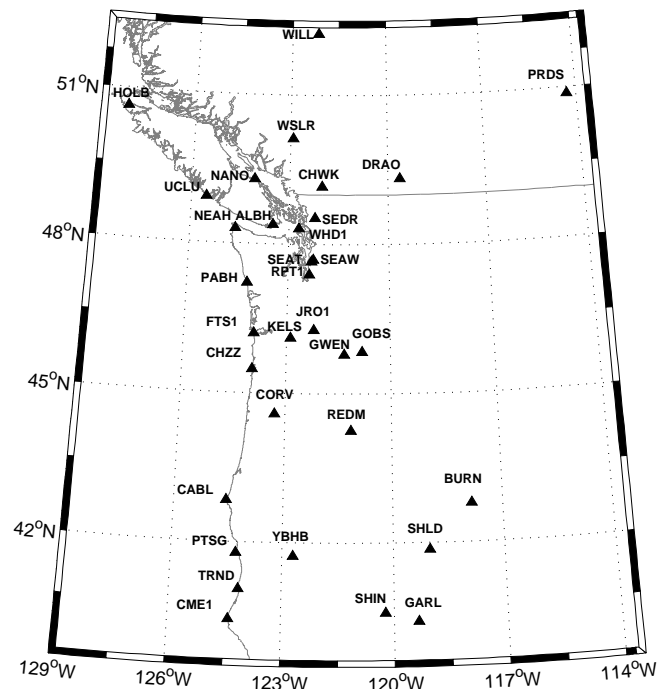


Figure 3.4: Pacific Northwest Geodetic Array (PANGA) which have nearly daily solutions through the period of 1996-2006. The figure is illustrated in Albers equal-area conic projection.

3.5.3 Data Processing Strategy

In this subsection, a central requirement is the numerical solution of statistical induction of eigenspace components, while the deterministic part of model is discussed in detail through two numerical examples in the previous section. Suppose that we have a certain number of permanent GPS stations, and each of them has observed n samples of velocities. Note that, we assume the recording of observations is performed at the same time for all the stations.

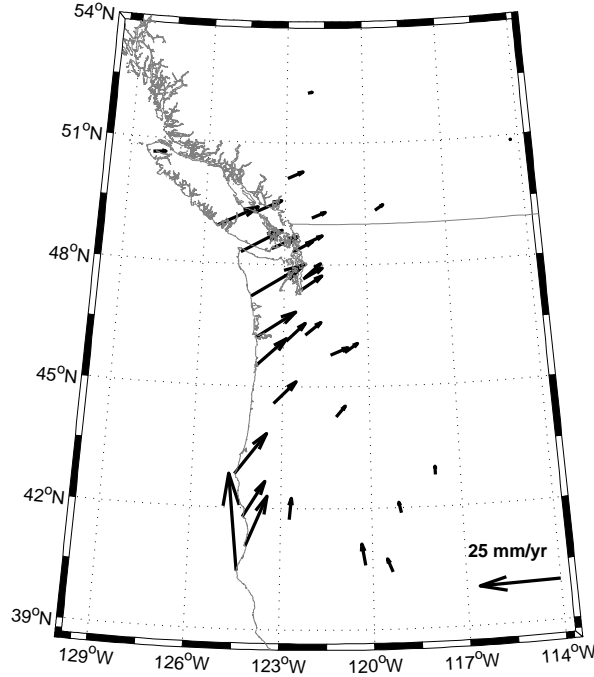


Figure 3.5: GPS-determined horizontal velocity field by Pacific Northwest Geodetic Array (PANGA). Velocity vectors plotted with respect to the station at Calgary (PRDS). The figure is illustrated in Albers equal-area conic projection.

Hence, performing the following steps to estimate the eigenspace components and their dispersion matrices (in strain tensor) for i th set of GPS velocities and their error variances (over a certain time):

- step 1.** Computing the curvilinear coordinates of the displacement vector \tilde{U}^K and \tilde{U}_K and deriving their covariance matrices $\mathbf{Q}_{\tilde{U}_K}$ or $\mathbf{Q}_{\tilde{U}^K}$, in the presence of GPS velocity errors, through Eqs. (3.2) or (3.4) for every station.
- step 2.** Using the Delaunay triangulation method for solving $\tilde{U}_{,\Lambda}^K$ or $\tilde{U}_{K,\Lambda}$ as well as finding their dispersion matrices $D\{\tilde{U}_{,\Lambda}^K\}$ or $D\{\tilde{U}_{K,\Lambda}\}$, based on the error propagation law (see Appendix B), for k th triangle (see Fig. 3.7)
- step 3.** Computing the local basis vectors based on centroid coordinates of the k th triangle and deriving the metric tensor \mathbf{A}_l , based upon the height information in the associated triangle.
- step 4.** Computing first-order partial derivatives of the displacement vector $\mathbf{u}_{,\Lambda}$ and its dispersion matrix $D\{\mathbf{u}_{,\Lambda}\}$ through Eqs. (3.1) and (3.1), for the k th triangle.
- step 5.** Obtaining strain tensor \mathbf{E}_l and the dispersion matrix of its components by Eqs.(2.22) and (3.5), for the k th triangle.
- step 6.** Simultaneous diagonalization of $\{\mathbf{E}_l, \mathbf{A}_l\}$ according to Eq. (3.10), deriving the vector-half form of the transformed strain tensor $\mathbf{y}_i'' = [\mathbf{E}_{i,1}'' \ \mathbf{E}_{i,2}'' \ \mathbf{E}_{i,3}'']^T$ and its dispersion matrix through Eq. (3.14) for the k th triangle.

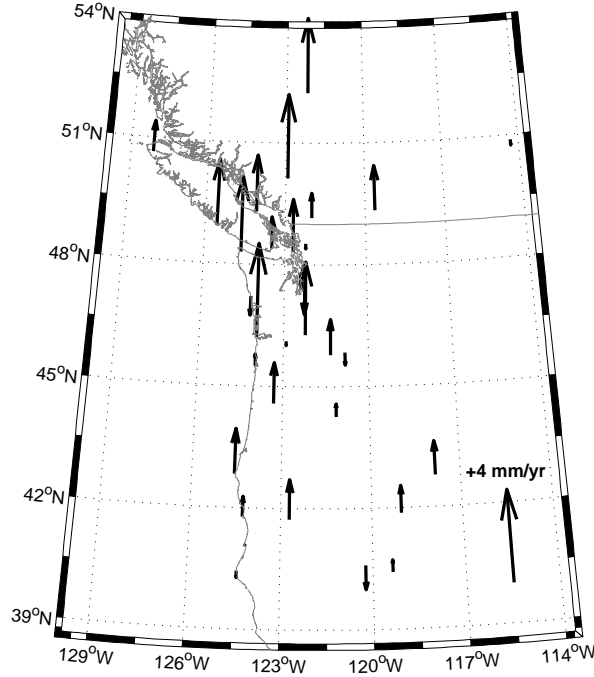


Figure 3.6: GPS-determined vertical velocity field by Pacific Northwest Geodetic Array (PANGA). Velocity vectors plotted with respect to the station at Calgary (PRDS). The figure is illustrated in Albers equal-area conic projection.

- step 7.** Repetition of the algorithm from Step 1 until the step 6, for the whole set of measurements n in the k th triangle.
- step 8.** Setup of an observation model based on the linearized multivariate Gauss- Markov model for eigenspace synthesis (see Eq. (3.23)), namely a system of $3 \times n$ equations and three unknowns (eigenspace components).
- step 9.** Estimation of eigenspace components and their dispersion matrices by Eqs. (3.25) and (3.26) for the k th triangle. This step is performed based upon n samples of *independent* 3×1 random vectors $\mathbf{y}_1'', \mathbf{y}_2'', \dots, \mathbf{y}_n''$, each with the 3×3 variance covariance matrix $\mathbf{Q}_{\mathbf{y}_i''}$.
- step 10.** Estimation of the covariance matrix for n set of measurements $\mathbf{y}_1'', \mathbf{y}_2'', \dots, \mathbf{y}_n''$ and repeating the estimation of eigenspace components and their dispersion matrix for the k th triangle.

The above algorithm can be applied to the estimation of eigenspace components of TCC and their dispersions. In this case we should deal with the difference vector of unit normal vectors \mathbf{w} and its dispersion matrix (see section 3.2).

Remark 3.5 As we mentioned in previous chapter, for the proposed method of deformation analysis, we should construct the real surface of the Earth. Similar the previous chapter, it could be performed through the combination of geoid height $N(\Lambda, \Phi)$ and orthometric height $\tilde{H}(\Lambda, \Phi)$, namely $H(\Lambda, \Phi) = \tilde{H}(\Lambda, \Phi) + N(\Lambda, \Phi)$. Hence, using a geoidal height model and orthometric height model, we could

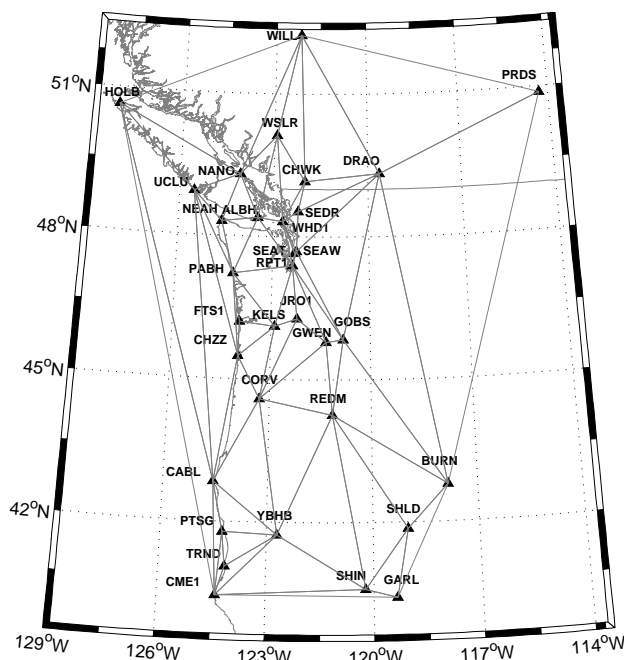


Figure 3.7: Optimal Delaunay triangulations over the Pacific Northwest Geodetic Array (PANGA). The figure is illustrated in Albers equal-area conic projection.

computed ellipsoidal height which closely fit the Earth's surface. These computations are performed by:

- i. Obtaining orthometric height, through the *Centre for Topographic Information* over the western Canada, which can be freely downloaded (<http://www.cits.rncan.gc.ca>). As a higher-resolution product, we made use of a resolution of approximately 20 meters (1:50 000 based on a collection of ground or reflective surface elevations.).
- ii. Obtaining geoidal height $N(\Lambda, \Phi)$, through the *Canadian Gravimetric Geoid 2005 (CGG05)*, which is freely available (<http://www.geod.nrcan.gc.ca/>). The Canadian Gravimetric Geoid 2005 (CGG05) is based on GRACE data up to degree 90 and supplemented with terrestrial information for the higher frequencies. A GPS-leveling comparison indicates a standard deviation of 10.2 cm for CGG05 [Huang and Véronneau, 2005].

3.5.4 Results

The numerical results of the above algorithm for $k = 1, 2, \dots, 58$ triangles over CSZ area are performed for the strain tensor and TCC which are shown in the following parts:

Estimated eigenspace components of strain tensor based on a-priori variance component information of transformed strain tensor

The Pattern of eigenspace components, namely eigenvalues and eigendirections, of the surface strain-rate tensor and their 95% confidence intervals, in unit of 10^{-7} yr^{-1} is illustrated in Fig. 3.8. *Extensions*

are represented by solid lines (red color) and *contractions* are illustrated by dashed lines (blue color). Tab. 3.1 also shows numerical results of estimated eigenspace components for the strain tensor (based on a-priori variance component information).

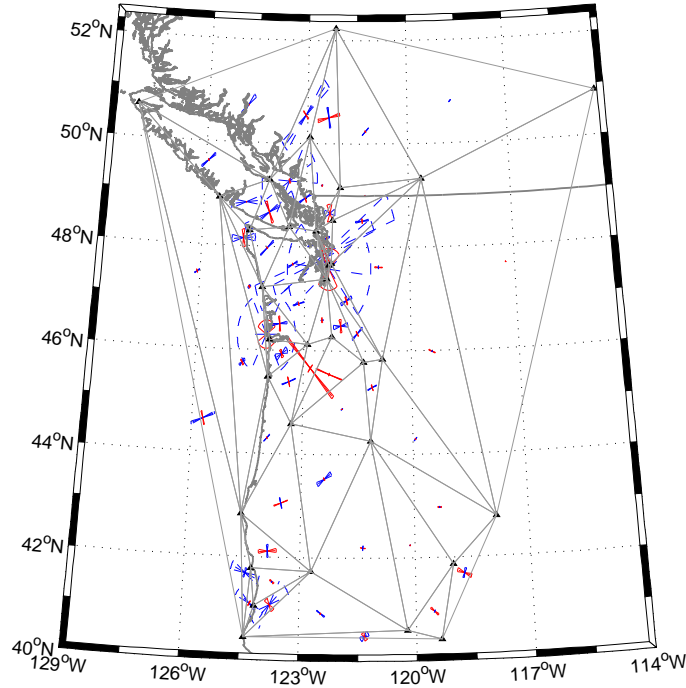


Figure 3.8: Pattern of eigenspace components of the surface strain-rate tensor and their 95% confidence intervals, in unit of 10^{-7} yr^{-1} . Extensions are represented by solid lines (red color) and contractions are illustrated by dashed lines (blue color) and triangles denote the permanent GPS stations. The figure is illustrated in Albers equal-area conic projection.

The highest contraction regions are in the forearc nearly parallel to the plate convergence. In other words, contraction rates are highest in networks close to the CSZ deformation front, namely: on the northern California coast, north of Cascadia also Vancouver Island, Seattle and decrease with distance from it becoming indistinguishable to zero at the most distant networks in the east of Oregon. An interesting feature of the pattern is a peak of high values around regions in the vicinity of JDF plate with North American plate in northern California. According to our model, perhaps both horizontal and vertical deformations of these regions are responsible for the high values of strain rate in these regions. The pattern of the surface strain rate confirms that most of areas are under contraction except regions in the west of Oregon which are under the extension. Perhaps additional deformations are responsible for these anomalies, such as post-eruption volcanic deformation [Murray and Lisowski, 2000].

The larger errors, namely 95% confidence intervals of eigenvalues and eigendirections of the surface strain rate is detected obviously in Seattle and west of Portland. That in return results from the variety of surface strain- rate observations in nearly daily solutions through the period of 1996-2006. These effects also reflect that the deformation patterns in those triangulations were not stable during the period of 1996-2006. By comparing the surface strain-rate pattern in Fig. 3.8 with seismicity maps (see Fig. 3.3), it can be concluded that in general our estimation of eigenspace components of surface

strain-rate tensors are consistent with the tectonic setting.

Estimated eigenspace components of TCC based on a-priori variance component information of transformed TCC

A pattern of eigenspace components namely eigenvalues and eigendirections, of TCC and their 95% confidence intervals is illustrated by the Fig. (3.9).

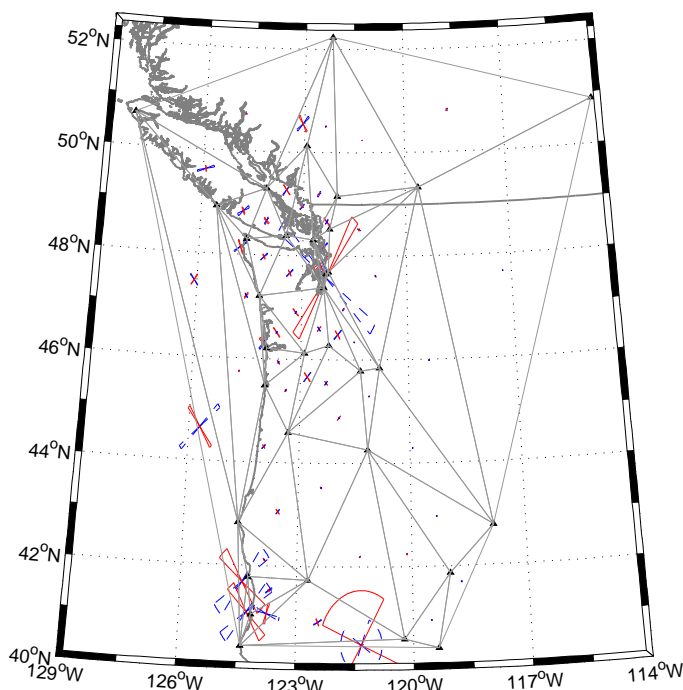


Figure 3.9: Pattern of eigenspace components of TCC and their 95% confidence intervals, in unit of $10^{-7} \text{ m}^{-1} \cdot \text{yr}^{-1}$. Positive eigenvalues are represented by solid lines (red color) and negative eigenvalues are represented by dashed lines (blue color). Triangles denote the permanent GPS stations. The figure is illustrated in Albers equal-area conic projection.

The estimated confidence intervals of eigenvalues and eigendirections of TCC over Pacific Northwest region indicates that deformation is spread over the whole region along the CSZ from the north of the California to the north of Vancouver Island, but along the coasts has highlighted values. The pattern indicates that, in general, Inland stations have insignificant deformations. However, the rates appear to vary significantly along the coast with the highest deformation occurring in the northern California and southern Oregon boundary, which is the most significant zone of seismicity in this region.

Estimated eigenspace components of strain tensor based on estimated covariance matrix of transformed strain tensor (via simultaneous diagonalization)

The estimated eigenspace components of strain tensor based on estimation of covariance matrix of transformed strain tensor (via simultaneous diagonalization) are illustrated in Fig. 3.10. Also, numerical values of them are presented in Tab. 3.3. A comparison of Figs. 3.10 and 3.8 shows that, in general

Table 3.1: Estimated eigenvalues and eigendirections of the strain tensor in 95% confidence intervals based on a-priori variance component information. The eigenvalues and related accuracies are given in units 10^{-8} yr^{-1} and orientation parameter and its standard deviation is given in degree.

N	Triangles	$\hat{\Lambda}_1$	$\hat{\sigma}_{\Lambda_1}$	$\hat{\Lambda}_2$	$\hat{\sigma}_{\Lambda_2}$	$\hat{\Theta}$	$\hat{\sigma}_{\Theta}$
1	nano-will-holb	-7.95	0.91	0.64	0.57	43.59	4.76
2	uclu-nano-holb	-20.11	1.41	0.97	0.78	33.02	3.03
3	pabh-uclu-chzz	-1.30	1.27	0.69	1.13	41.24	20.63
4	wslr-nano-will	-76.77	5.44	3.99	3.38	44.30	3.85
5	wslr-chwk-will	29.27	1.76	-18.93	0.75	11.26	2.95
6	cabl-cme1-holb	-32.14	2.69	1.08	1.67	19.33	2.35
7	cabl-uclu-holb	-8.31	0.52	1.97	0.79	28.34	3.52
8	cabl-uclu-chzz	-5.55	1.79	2.51	1.95	39.60	8.78
9	shin-shld-garl	9.94	0.69	-1.15	0.69	-33.14	5.82
10	shin-cme1-garl	-6.33	2.44	0.64	4.08	33.46	14.32
11	shin-ybhb-cme1	-9.82	0.79	1.03	0.55	-30.99	3.49
12	neah-uclu-nano	-39.50	2.07	0.47	2.73	5.72	6.03
13	neah-pabh-uclu	-27.52	3.13	9.42	4.00	3.64	6.44
14	albh-wslr-nano	-75.38	3.23	1.57	1.46	28.79	15.62
15	albh-neah-nano	-70.20	2.44	18.19	2.41	26.64	3.73
16	albh-neah-pabh	-20.23	1.07	0.08	1.14	38.12	2.70
17	redm-shin-shld	-0.97	0.19	0.51	0.27	22.62	6.75
18	redm-shin-ybhb	6.03	0.43	-3.63	0.44	-6.53	2.27
19	fts1-pabh-chzz	-38.98	15.52	1.62	5.58	1.29	29.87
20	burn-shld-garl	15.15	1.80	-4.87	2.24	-19.37	6.64
21	burn-redm-shld	4.30	0.28	-0.77	0.40	-1.67	8.84
22	burn-redm-gobs	-3.96	0.52	0.41	0.55	42.79	3.07
23	drao-will-prds	-3.05	0.10	-0.43	0.09	38.96	1.31
24	drao-chwk-will	-11.67	0.24	1.28	0.26	37.99	0.81
25	drao-burn-prds	1.46	0.07	0.19	0.09	-15.05	2.61
26	drao-burn-gobs	8.43	-0.41	-0.42	0.26	-19.41	3.22
27	ptsg-cabl-cme1	-33.84	1.90	-4.49	29.53	-22.35	6.78
28	ptsg-cabl-ybhb	20.82	1.02	-8.98	1.71	3.43	4.62
29	whd1-wslr-chwk	-1.00	0.46	0.20	0.76	11.68	17.29
30	whd1-albh-wslr	-16.74	1.37	4.88	2.00	26.21	2.76
31	burn-redm-gobs	-10.93	0.91	5.03	0.65	21.29	2.36
32	trnd-ybhb-cme1	-41.02	5.79	1.92	6.08	41.78	10.23
33	trnd-ptsg-cme1	-16.87	1.91	4.81	2.75	-34.74	5.92
34	trnd-ptsg-ybhb	5.29	0.34	-0.70	0.52	-32.56	8.32
35	seaw-drao-gobs	9.80	0.39	-2.48	0.38	-2.06	2.99
36	corv-gwen-redm	-1.78	0.41	0.32	0.25	30.86	9.32
37	corv-cabl-chzz	-9.42	0.48	0.73	0.53	41.03	1.73
38	corv-cabl-ybhb	17.81	0.67	-9.78	0.61	17.04	1.20
39	corv-redm-ybhb	-17.24	1.82	0.57	1.47	30.65	6.32
40	sedr-whd1-chwk	-3.27	6.04	0.90	8.22	5.26	12.88
41	sedr-seaw-whd1	-5.08	1.68	0.15	1.25	20.58	7.38
42	sedr-drao-chwk	-0.54	0.31	0.41	0.11	21.17	18.02
43	sedr-seaw-drao	-17.51	0.53	3.26	0.90	6.04	2.39
44	jro1-corv-gwen	36.07	0.58	1.68	0.60	-16.58	0.74
45	rpt1-whd1-albh	-6.15	0.61	0.71	0.69	11.93	3.93
46	rpt1-albh-pabh	-12.22	1.15	1.11	0.64	23.57	3.15
47	rpt1-jro1-gwen	-14.47	2.73	8.83	2.05	8.03	6.40
48	rpt1-gwen-gobs	-12.54	2.62	0.58	2.64	38.99	3.65
49	rpt1-seaw-gobs	-12.04	2.10	4.39	1.90	25.88	5.52
50	kels-corv-chzz	-17.90	0.77	8.72	0.67	17.65	1.16
51	kels-jro1-corv	79.79	2.08	4.64	2.34	-41.37	1.11
52	kels-fts1-chzz	-14.93	1.08	5.31	1.55	27.16	11.07
53	kels-rpt1-jro1	-2.24	0.66	1.75	1.54	6.62	9.48
54	kels-fts1-pabh	-17.23	1.52	11.54	1.59	6.84	3.29
55	kels-rpt1-pabh	-13.90	0.77	1.00	1.31	13.16	2.13
56	seat-seaw-whd1	-18.92	6.02	5.10	5.05	25.43	3.72
57	seat-rpt1-whd1	-13.99	6.84	8.71	6.22	25.10	2.44
58	seat-rpt1-seaw	-113.44	7.92	21.22	6.17	-5.37	20.55

Table 3.2: Estimated eigenvalues and eigendirections of TCC in 95% confidence intervals based on a-priori variance component information. The eigenvalues and related accuracies are given in units 10^{-8} yr^{-1} and orientation parameter and its standard deviation is given in degree.

N	Triangles	$\hat{\Lambda}'_1$	$\hat{\sigma}_{\Lambda'_1}$	$\hat{\Lambda}'_2$	$\hat{\sigma}_{\Lambda'_2}$	$\hat{\Theta}'$	$\hat{\sigma}_{\Theta}'$
1	nano-will-holb	-19.27	0.60	4.01	0.64	34.09	1.62
2	uclu-nano-holb	-25.59	1.34	3.18	0.86	45.29	2.14
3	pabh-uclu-chzz	-1.42	0.58	0.22	0.30	15.41	0.89
4	wslr-nano-will	-96.03	10.59	59.17	8.93	5.19	2.49
5	wslr-chwk-will	17.79	0.09	-6.13	0.24	-2.01	0.22
6	cabl-cme1-holb	-49.43	0.67	0.86	0.58	6.00	1.13
7	cabl-uclu-holb	-19.44	0.40	1.46	0.35	45.01	0.85
8	cabl-uclu-chzz	-8.57	0.58	0.98	0.44	44.87	1.83
9	shin-shld-garl	0.47	0.16	-0.23	0.16	-31.13	1.35
10	shin-cme1-garl	-3.58	0.01	0.03	0.50	-29.00	24.36
11	shin-ybhb-cme1	-2.49	0.15	0.17	0.05	-2.18	1.10
12	neah-uclu-nano	3.78	0.03	-0.56	0.04	-10.62	0.65
13	neah-pabh-uclu	-5.00	0.37	3.78	0.10	15.16	0.40
14	albh-wslr-nano	2.17	0.00	-0.59	0.01	-5.76	1.76
15	albh-neah-nano	5.69	0.46	-0.27	0.03	-21.06	2.11
16	albh-neah-pabh	5.31	0.19	-0.17	0.68	-23.73	2.52
17	redm-shin-shld	-2.37	0.12	1.12	0.08	0.12	0.33
18	redm-shin-ybhb	0.14	0.08	-0.13	0.27	-42.53	2.69
19	fts1-pabh-chzz	-48.98	7.85	9.98	5.95	24.67	2.32
20	burn-shld-garl	27.64	0.39	-0.52	0.31	-44.36	0.24
21	burn-redm-shld	4.92	0.27	-0.12	0.24	-44.34	1.05
22	burn-redm-gobs	-1.93	0.17	0.87	0.04	20.77	1.78
23	drao-will-prds	-21.29	0.03	-0.74	0.03	0.32	0.16
24	drao-chwk-will	-3.19	0.11	0.43	0.26	37.36	2.08
25	drao-burn-prds	2.41	0.02	0.08	0.02	-6.76	0.92
26	drao-burn-gobs	6.89	0.20	-0.98	0.16	-19.07	2.35
27	ptsg-cabl-cme1	-48.55	8.14	-4.14	22.52	-4.89	1.00
28	ptsg-cabl-ybhb	19.52	0.35	-9.96	0.28	3.27	2.34
29	whd1-wslr-chwk	-3.86	0.37	0.06	0.17	40.00	4.49
30	whd1-albh-wslr	-6.34	3.19	5.77	3.40	29.72	0.47
31	burn-redm-gobs	-9.39	0.43	3.89	0.46	25.72	1.52
32	trnd-ybhb-cme1	-48.78	0.82	0.81	0.76	35.00	0.14
33	trnd-ptsg-cme1	-28.08	6.71	-13.03	5.09	-20.78	1.44
34	trnd-ptsg-ybhb	6.86	0.29	-0.37	0.32	-41.07	2.64
35	seaw-drao-gobs	7.66	0.76	-6.58	0.07	12.63	2.13
36	corv-gwen-redm	-4.05	0.38	0.55	0.23	33.93	1.71
37	corv-cabl-chzz	-9.61	0.21	0.92	0.29	40.27	1.06
38	corv-cabl-ybhb	11.75	0.41	-4.22	0.22	23.63	1.02
39	corv-redm-ybhb	-0.53	0.54	0.13	0.29	37.06	1.67
40	sedr-whd1-chwk	-32.08	1.53	2.88	1.53	30.00	2.51
41	sedr-seaw-whd1	-11.32	0.29	1.66	0.08	30.01	2.34
42	sedr-drao-chwk	-1.85	0.11	0.07	0.04	32.00	2.95
43	sedr-seaw-drao	-5.62	0.45	5.60	0.26	10.11	1.52
44	jro1-corv-gwen	4.70	0.36	1.16	0.93	-2.43	1.00
45	rpt1-whd1-albh	-0.15	0.43	0.05	0.11	40.00	1.32
46	rpt1-albh-pabh	-5.74	0.08	0.35	0.18	46.61	1.94
47	rpt1-jro1-gwen	-17.39	0.31	9.77	1.04	26.15	3.91
48	rpt1-gwen-gobs	-3.35	0.88	0.62	2.63	20.00	1.51
49	rpt1-seaw-gobs	-19.98	1.10	16.03	2.24	13.60	1.83
50	kels-corv-chzz	-23.42	0.70	6.05	0.34	27.73	1.47
51	kels-jro1-corv	27.31	2.35	14.42	0.63	-4.15	1.15
52	kels-fts1-chzz	-23.76	0.78	0.30	0.61	15.00	3.51
53	kels-rpt1-jro1	-20.07	0.36	5.07	0.77	31.89	1.73
54	kels-fts1-pabh	-1.77	0.88	1.17	1.20	20.00	1.31
55	kels-rpt1-pabh	-18.91	1.30	4.75	0.12	20.02	1.78
56	seat-seaw-whd1	-100.90	6.77	4.23	4.68	25.02	1.16
57	seat-rpt1-whd1	-1.92	2.17	0.75	2.00	25.72	1.79
58	seat-rpt1-seaw	-113.44	7.12	21.22	6.17	-11.10	2.05

after estimating the covariance matrix of transformed strain tensor (via simultaneous diagonalization) variances of eigenspace components become smaller.

In general, estimating the covariance matrix of observations (transformed strain tensor), should lead us to minimum variance, but in some triangles it did not occur. To discuss the effect of unspecific results, let $\mathbf{Q}_{\text{vec}(\mathbf{Y}'')}$ be the correct covariance matrix of observations (transformed strain tensor) and $\mathbf{Q}'_{\text{vec}(\mathbf{Y}'')}$ be an incorrect one. If the least-squares estimation of ξ is done with the $\mathbf{Q}'_{\text{vec}(\mathbf{Y}'')}$, then $\hat{\xi} = (\mathbf{A}^T \mathbf{Q}'_{\text{vec}(\mathbf{Y}'')}^{-1} \mathbf{A})^{-1} \mathbf{A}^T \mathbf{Q}'_{\text{vec}(\mathbf{Y}'')}^{-1} \text{vec} \mathbf{Y}$ is still an unbiased estimator of ξ and

$$\hat{\xi} = (\mathbf{A}^T \mathbf{Q}'_{\text{vec}(\mathbf{Y}'')}^{-1} \mathbf{A})^{-1} \mathbf{A}^T \mathbf{Q}'_{\text{vec}(\mathbf{Y}'')}^{-1} \mathbf{Q}_{\text{vec}(\mathbf{Y}'')}^{-1} \mathbf{Q}'_{\text{vec}(\mathbf{Y}'')}^{-1} \mathbf{A} (\mathbf{A}^T \mathbf{Q}'_{\text{vec}(\mathbf{Y}'')}^{-1} \mathbf{A})^{-1}$$

is the correct covariance matrix of estimator $\hat{\xi}$. Therefore, if one uses $\mathbf{Q}'_{\hat{\xi}} = (\mathbf{A}^T \mathbf{Q}'_{\text{vec}(\mathbf{Y}'')}^{-1} \mathbf{A})^{-1}$ as the matrix of estimator $\hat{\xi}$ one will have an incorrect precision of $\hat{\xi}$ description which can be too optimistic if $\mathbf{Q}_{\hat{\xi}} \geq \mathbf{Q}'_{\hat{\xi}}$, but also too pessimistic if $\mathbf{Q}_{\hat{\xi}} \leq \mathbf{Q}'_{\hat{\xi}}$. For a more detailed discussion see Amiri-Simkooei [2007, page 135].

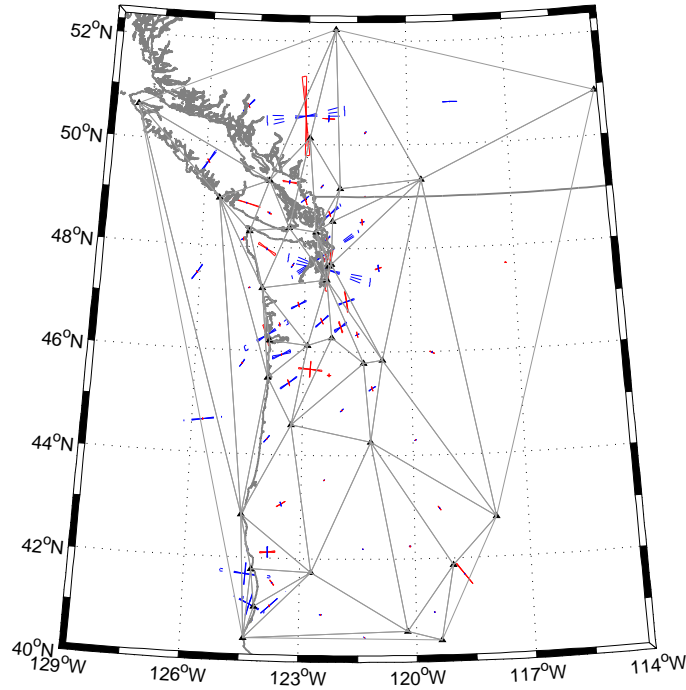


Figure 3.10: Pattern of eigenspace components of the surface strain-rate tensor and their 95% confidence intervals, in unit of 10^{-7} yr^{-1} based on estimated covariance matrix of transformed strain tensor (via simultaneous diagonalization). Extensions are represented by solid lines (red color) and contractions are illustrated by dashed lines (blue color). Triangles denote the permanent GPS stations. The figure is illustrated in Albers equal-area conic projection.

Estimated eigenspace components of TCC based on estimated covariance matrix of transformed TCC (via simultaneous diagonalization)

In the same manner we perform the illustration of eigenspace components of TCC and their 95% confidence intervals, based on estimation of covariance matrix of transformed TCC (via simultaneous

Table 3.3: Estimated eigenvalues and eigendirections of strain tensor in 95% confidence intervals based on estimated covariance matrix of transformed strain tensor (via simultaneous diagonalization). The eigenvalues and related accuracies are given in units 10^{-8} yr^{-1} and orientation parameter and its standard deviation is given in degree.

N	Triangles	$\hat{\Lambda}_1$	$\hat{\sigma}_{\Lambda_1}$	$\hat{\Lambda}_2$	$\hat{\sigma}_{\Lambda_2}$	$\hat{\Theta}$	$\hat{\sigma}_{\Theta}$
1	nano-will-holb	-3.62	0.82	0.64	0.82	-24.10	1.85
2	uclu-nano-holb	-7.06	2.42	0.62	2.92	11.67	1.91
3	pabh-uclu-chzz	14.82	2.78	-9.22	2.32	41.41	6.31
4	wslr-nano-will	-2.20	5.87	1.61	6.24	37.51	3.34
5	wslr-chwk-will	4.56	1.55	-4.05	0.96	43.43	6.97
6	cabl-cme1-holb	-26.29	15.71	17.17	13.29	40.52	1.99
7	cabl-uclu-holb	-4.96	3.29	4.32	2.93	-41.98	1.79
8	cabl-uclu-chzz	-4.39	0.29	2.44	0.62	36.45	3.27
9	shin-shld-garl	4.98	0.27	-3.42	0.58	-45.03	3.70
10	shin-cme1-garl	-18.32	27.37	3.56	0.00	17.86	25.36
11	shin-ybhb-cme1	-16.37	2.18	4.75	3.14	26.92	2.45
12	neah-uclu-nano	-6.52	3.17	15.81	2.77	28.21	4.97
13	neah-pabh-uclu	-4.94	4.11	0.86	4.33	28.07	2.06
14	albh-wslr-nano	-2.13	4.38	2.49	2.78	43.36	2.11
15	albh-neah-nano	-9.88	2.42	6.83	3.58	52.22	6.57
16	albh-neah-pabh	-10.01	2.18	5.36	1.98	34.36	1.98
17	redm-shin-shld	-2.31	0.31	2.17	0.50	37.14	2.68
18	redm-shin-ybhb	-1.77	0.38	1.46	0.56	35.25	2.55
19	fts1-pabh-chzz	6.91	4.25	-5.31	6.45	-41.72	4.14
20	burn-shld-garl	0.86	0.75	-0.24	0.48	-40.11	3.85
21	burn-redm-shld	1.25	0.27	-0.36	0.25	-45.64	2.67
22	burn-redm-gobs	1.36	0.24	-0.83	0.24	41.68	1.96
23	drao-will-prds	-1.62	0.26	1.76	0.27	38.78	1.25
24	drao-chwk-will	0.38	0.37	0.07	0.31	-37.31	4.72
25	drao-burn-prds	1.33	0.09	-0.84	0.24	-45.81	1.84
26	drao-burn-gobs	1.03	0.17	-0.21	0.18	-36.34	5.11
27	ptsg-cabl-cme1	-68.03	33.70	57.24	25.60	44.19	5.05
28	ptsg-cabl-ybhb	6.04	1.57	-5.72	1.37	-40.20	5.13
29	whd1-wslr-chwk	-5.44	1.88	4.52	0.90	45.50	10.68
30	whd1-albh-wslr	-1.57	1.83	1.25	0.46	38.09	3.21
31	burn-redm-gobs	1.06	0.75	-0.61	0.83	40.03	8.26
32	trnd-ybhb-cme1	-23.14	9.47	0.91	10.37	-16.96	3.39
33	trnd-ptsg-cme1	-44.45	41.66	33.82	29.09	40.72	4.35
34	trnd-ptsg-ybhb	-10.60	3.03	3.10	1.78	28.23	4.35
35	seaw-drao-gobs	2.14	0.70	-1.28	0.36	-43.00	1.82
36	corv-gwen-redm	4.17	0.61	-4.12	0.56	45.03	1.47
37	corv-cabl-chzz	-8.37	2.64	7.05	1.70	40.92	3.22
38	corv-cabl-ybhb	-8.62	1.35	7.58	1.53	43.96	1.90
39	corv-redm-ybhb	4.18	0.41	-4.58	0.69	-40.60	3.02
40	sedr-whd1-chwk	12.79	4.25	-7.22	2.56	-41.60	3.56
41	sedr-seaw-whd1	-8.17	3.06	5.53	5.21	35.38	3.23
42	sedr-drao-chwk	-0.42	0.94	0.30	0.44	-22.29	11.95
43	sedr-seaw-drao	-2.37	0.82	0.69	0.81	-18.13	1.79
44	jro1-corv-gwen	4.48	0.78	-4.45	0.78	-44.34	1.06
45	rpt1-whd1-albh	-1.26	1.16	1.16	0.90	38.85	2.49
46	rpt1-albh-pabh	-11.27	1.92	5.77	1.82	35.39	1.90
47	rpt1-jro1-gwen	-5.53	2.60	5.46	2.97	39.92	1.87
48	rpt1-gwen-gobs	2.23	0.82	-0.39	1.05	-29.64	12.58
49	rpt1-seaw-gobs	-7.84	2.45	5.15	1.22	42.38	6.69
50	kels-corv-chzz	6.91	0.53	-6.65	1.36	41.08	3.37
51	kels-jro1-corv	-2.52	1.79	2.00	1.67	43.54	1.16
52	kels-fts1-chzz	9.24	1.64	-7.01	1.49	-45.69	3.67
53	kels-rpt1-jro1	2.76	1.77	-2.47	1.65	44.54	2.66
54	kels-fts1-pabh	8.58	1.88	-7.15	1.59	-43.00	1.83
55	kels-rpt1-pabh	8.83	1.61	-6.72	1.69	-41.45	1.85
56	seat-seaw-whd1	4.06	13.37	-1.17	12.25	31.24	3.72
57	seat-rpt1-whd1	-11.28	3.99	16.09	3.61	40.23	4.31
58	seat-rpt1-seaw	-16.67	39.50	8.47	35.32	-36.27	2.32

diagonalization) by Fig. 3.11. Also, numerical values of them are presented in Tab. 3.4. Comparing Figs. 3.11 and 3.9 shows the estimated covariance components have influence on the confidence intervals of eigenspace components.

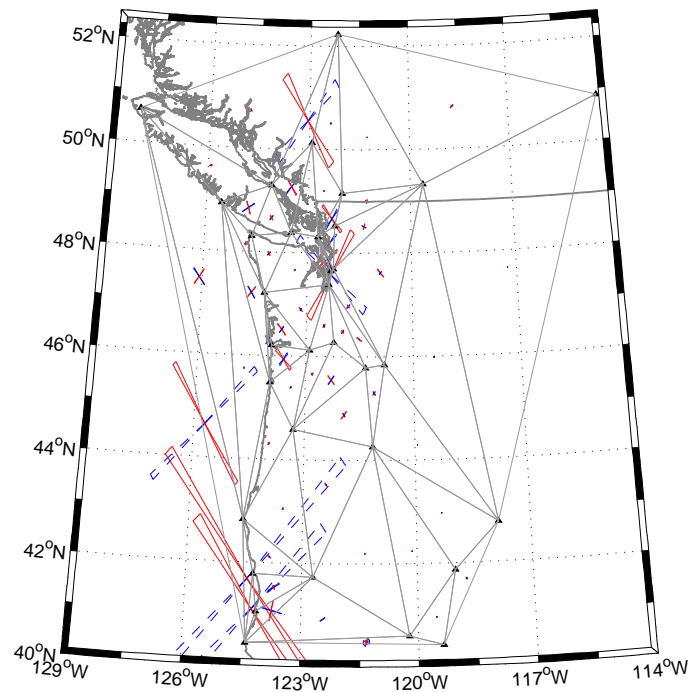


Figure 3.11: Pattern of eigenspace components of the TCC and their 95% confidence intervals, in unit of 10^{-7} yr^{-1} based on estimated covariance matrix of transformed TCC (via simultaneous diagonalization). Positive eigenvalues are represented by solid lines (red color) and negative eigenvalues are represented by dashed lines (blue color). Triangles denote the permanent GPS stations. The figure is illustrated in Albers equal-area conic projection.

Table 3.4: Estimated eigenvalues and eigendirections of TCC in 95% confidence intervals based on estimated covariance matrix of transformed TCC (via simultaneous diagonalization). The eigenvalues and related accuracies are given in units 10^{-8} yr^{-1} and orientation parameter and its standard deviation is given in degree.

N	Triangles	$\hat{\Lambda}'_1$	$\hat{\sigma}_{\Lambda'_1}$	$\hat{\Lambda}'_2$	$\hat{\sigma}_{\Lambda'_2}$	$\hat{\Theta}'$	$\hat{\sigma}_{\Theta}'$
1	nano-will-holb	-2.25	0.64	0.70	0.06	-23.68	1.44
2	uclu-nano-holb	-8.24	0.59	0.62	0.03	13.76	3.04
3	pabh-uclu-chzz	11.95	3.26	-9.07	0.31	41.40	0.17
4	wslr-nano-will	-2.16	0.37	1.98	0.42	40.02	0.05
5	wslr-chwk-will	4.36	0.28	-4.08	0.20	44.47	0.64
6	cabl-cme1-holb	-26.64	6.47	17.46	6.38	39.30	9.02
7	cabl-uclu-holb	-4.90	0.43	4.39	4.18	-42.50	0.14
8	cabl-uclu-chzz	-4.15	0.29	2.69	0.62	38.33	3.27
9	shin-shld-garl	4.89	0.27	-3.61	0.58	-42.73	3.70
10	shin-cme1-garl	-18.15	1.91	3.59	0.25	24.13	1.52
11	shin-ybhb-cme1	-16.56	0.86	4.16	0.13	27.00	6.06
12	neah-uclu-nano	-6.23	6.26	1.56	6.26	25.39	18.96
13	neah-pabh-uclu	-4.95	1.01	0.99	0.81	23.29	1.18
14	albh-wslr-nano	-2.14	13.84	2.05	15.04	41.27	0.71
15	albh-neah-nano	-9.61	0.48	6.78	0.86	39.63	0.71
16	albh-neah-pabh	-10.56	6.55	5.25	6.54	35.09	28.64
17	redm-shin-shld	-2.51	0.29	2.24	0.10	40.23	2.14
18	redm-shin-ybhb	-1.55	0.24	1.39	0.22	39.00	4.24
19	fts1-pabh-chzz	6.90	6.17	-5.59	0.61	-42.23	0.62
20	burn-shld-garl	0.87	0.06	-0.21	0.06	-43.42	14.45
21	burn-redm-shld	1.23	0.06	-0.39	0.24	-40.27	2.19
22	burn-redm-gobs	1.32	0.06	-0.84	0.05	44.02	0.80
23	drao-will-prds	-1.17	0.09	1.01	0.11	35.41	2.06
24	drao-chwk-will	0.40	0.03	0.07	0.26	-39.73	37.14
25	drao-burn-prds	1.62	0.13	-0.84	0.15	-42.87	3.30
26	drao-burn-gobs	1.09	0.06	-0.27	0.05	-39.47	0.57
27	ptsg-cabl-cme1	-66.73	1.63	56.05	1.65	42.84	0.92
28	ptsg-cabl-ybhb	6.96	1.57	-5.07	1.37	-41.29	5.13
29	whd1-wslr-chwk	-5.51	0.50	4.95	0.50	42.37	7.48
30	whd1-albh-wslr	-1.51	0.08	1.25	0.02	37.85	0.97
31	burn-redm-gobs	1.05	1.11	-0.64	1.18	43.11	0.25
32	trnd-ybhb-cme1	-27.52	37.99	1.00	29.39	-11.84	2.37
33	trnd-ptsg-cme1	-47.39	5.69	35.40	5.41	41.19	0.22
34	trnd-ptsg-ybhb	-11.31	0.54	3.35	4.43	28.36	1.83
35	seaw-drao-gobs	2.13	0.11	-1.13	0.83	-40.85	2.67
36	corv-gwen-redm	4.16	1.15	-4.12	0.03	43.45	0.15
37	corv-cabl-chzz	-8.01	0.42	7.38	0.49	43.53	6.70
38	corv-cabl-ybhb	-8.04	0.42	7.93	0.42	44.23	2.88
39	corv-redm-ybhb	4.09	0.70	-3.35	0.66	-43.89	0.08
40	sedr-whd1-chwk	11.10	8.06	-8.92	7.91	-42.61	0.06
41	sedr-seaw-whd1	-8.16	18.36	6.42	18.42	40.70	25.22
42	sedr-drao-chwk	-0.43	0.01	0.32	0.11	-17.23	1.80
43	sedr-seaw-drao	-2.59	1.46	0.63	1.40	-20.68	0.23
44	jro1-corv-gwen	4.95	0.53	-4.45	0.62	-44.66	0.04
45	rpt1-whd1-albh	-1.53	0.05	1.15	0.05	36.47	0.09
46	rpt1-albh-pabh	-10.37	0.09	5.27	0.24	35.08	1.73
47	rpt1-jro1-gwen	-5.53	0.04	5.50	0.57	44.23	0.52
48	rpt1-gwen-gobs	2.35	0.07	-0.39	0.40	-28.97	1.51
49	rpt1-seaw-gobs	-7.32	2.41	5.66	0.02	40.24	1.47
50	kels-corv-chzz	6.93	0.09	-6.77	0.11	44.73	2.04
51	kels-jro1-corv	-2.59	2.14	1.96	2.15	37.84	1.17
52	kels-fts1-chzz	8.84	6.40	-7.44	0.07	-43.00	4.39
53	kels-rpt1-jro1	2.67	4.10	-2.49	4.11	42.89	10.24
54	kels-fts1-pabh	8.90	1.93	-7.91	1.63	-43.70	1.37
55	kels-rpt1-pabh	8.79	0.89	-7.20	0.83	-42.72	6.15
56	seat-seaw-whd1	4.04	0.63	-1.21	6.69	31.88	2.61
57	seat-rpt1-whd1	-13.28	0.92	10.44	9.29	41.00	4.20
58	seat-rpt1-seaw	-15.00	2.35	8.31	0.24	-35.91	0.04

Chapter 4

Concluding Remarks

4.1 Discussion

Intrinsic deformation analysis with aspects of deterministic and stochastic models has been shown to be a reliable and powerful tool for detecting deformation patterns. On the basis of the presented theory and the numerical results obtained with simulated and real data-set, the following conclusions can be drawn:

- i. The local basis vectors of deformed surface are formulated in terms of the local basis vectors of undeformed surface and curvilinear components of the displacement vector. This will provide a representation to intrinsic geometry of a deformed surface with deriving information about the displacement field.
- ii. According to differential geometry, Gaussian and mean curvatures are invariants under the transformation of coordinate systems. Hence, intrinsic geometric properties of the deformed surface can be described in terms of changing mean and Gaussian curvatures. They can propose a shape classification of a deformed surface based upon signs of mean and Gaussian curvatures which are new tools for studying the Earth's deformation.
- iii. Employing simultaneous diagonalization to pairs of strain and metric tensors or pairs of tensor of change of curvature (TCC) with associated metrics leads to establishing a mapping between eigenspace components and transformed tensors (suitable for statistical inference of eigenspace components).
- iv. Comparison of the proposed method with plane strain, shows capabilities of this method in areas with high variations in vertical components (height components). The differences between corresponding patterns of two methods could be discussed from the modeling of the displacement problem which we referred to the real surface of the Earth as well as the effect of ignoring the height components of the deformation field in horizontal strain rates.
- v. In the presence of errors in measuring a random displacement field (under the normal distribution assumption of displacement field), stochastic behaviors of eigenspace components of strain tensor and TCC are discussed. We divided the context into two parts : In the first, we considered independent random vectors of repeated tensor measurements. In the second step we considered correlations between repeated measurements and we estimated a covariance matrix of measurements.

Stochastic behaviors of eigenspace components with repeated measurements are applied by a numerical example with the crustal deformation field (through the continuous GPS data) in Cascadia Subduction Zone (CSZ). It is performed based on a-priori given variance component information (which we derived based on propagation of variances from GPS velocity to tensor elements) and a posteriori (co)variance information (through a estimated covariance matrix) of tensor measurements. Comparing the results showed that, in general after estimating the covariance matrix of observations (transformed tensors via simultaneous diagonalization) variances of eigenspace components become smaller. However, in some areas it did not occur. They can be related to incorrect descriptions of initial accuracies, either too optimistic or too pessimistic.

4.2 Outlook

Mathematically, the FEM is used for finding an approximate solution of partial differential equations (PDE). It is a good choice for solving partial differential equations over scattered domains. For instance, in simulating the deformation field of crust, it is more important to have reliable predictions over the areas which we have dense networks of GPS stations than over less dense areas, a demand that is achievable using the FEM. The optimal finite element meshes can be generated by Delaunay triangulation over the test area. However, in some cases, the biggest disadvantage of this method is producing a subdivision made of triangles with elongated shapes that leads to inaccuracies in numerical interpolation. An undesirable feature of these types of implementation, can be verified by using other methods of interpolations and modelings. An example could be the use of smooth surface splines on deformation field instead of using FEM.

Further efforts should be undertaken to establishment of stress-strain relations in Earth surface deformation analysis based on the theoretical foundation provided here. Such verification points can be used in dealing with seismic activities, while seismic sources are governed by the stress tensor field.

Bibliography

- Adam, F., Dede, K., Heck, B., Kutterer, H., Mayer, M., Seitz, K., and Szucs, L. (2002). GPS deformation measurements in the geodynamic test network Soskut. *Periodica Polytechnica, Ser. Civ.*, 46(2):169–177.
- Ahjos, T. and Uski, M. (1992). Earthquakes in Northern Europe in 1375-1989. *Tectonophysics*, 207(1-2):1–23.
- Altiner, Y. (1996). *Geometrische modellierung innerer und äußerer deformationen der Erdoberfläche*. Number 462 in Reihe C. Deutsche Geodätische Kommission, Bayerischen Akademie Wissenschaften.
- Altiner, Y. (1999). *Analytical Surface Deformation Theory: for Detection of the Earth's Crust Movements*. Springer, Berlin.
- Amiri-Simkooei, A. R. (2007). *Least-Squares Variance Component Estimation: Theory and GPS Applications*. PhD thesis, Technische Universiteit Delft.
- Aravind, P. K. (1988). Geometrical interpretation of the simultaneous diagonalization of two quadratic forms. *Am. J. Phys.*, 57(4):309–311.
- Argus, D. F., Gordon, R. G., Demets, C., and Stein, S. (1989). Closure of the Africa-Eurasia-North America plate motion circuit and tectonics of the Gloria fault. *J. Geophys. Res.*, 94(B5):5585–5602.
- Bada, G., Horvath, F., Gerner, P., and Fejes, I. (1999). Review of the present-day geodynamics of the Pannonian basin: progress and problems. *J. Geodyn.*, 27(4):501–527.
- Bennett, R. A., Rodi, W., and Reilinger, R. E. (1996). Global positioning system constraints on fault slip rates in Southern California and northern Baja, Mexico. *J. Geophys. Res.*, 101(B10):21943–21960.
- Bursa, M. and Pec, K. (1993). *Gravity field and dynamics of the earth*. Springer-Verlag, Berlin.
- Cai, J. (2004). *Statistical Inference of the Eigenspace Components of a Symmetric Random Deformation Tensor*. PhD thesis, Institute of Geodesy, Universität Stuttgart, Germany.
- Cai, J. and Grafarend, E. W. (2007a). Statistical analysis of geodetic deformation (strain rate) derived from the space geodetic measurements of BIFROST project in Fennoscandia. *J. Geodyn.*, 43(2):214–238.
- Cai, J. and Grafarend, E. W. (2007b). Statistical analysis of the eigenspace components of the two-dimensional, symmetric rank-two strain rate tensor derived from the space geodetic measurements (ITRF92-ITRF2000 data sets) in central Mediterranean and Western Europe. *Geophys. J. Int.*, 168(2):449–472.
- Chen, X. (1998). Continuous GPS monitoring of crustal deformation with the Western Canada Deformation Array, 1992-1995. Master's thesis, University of New Brunswick, <http://www.scientificcommons.org/8897140>.
- Chovitz, B. H. (1979). A general theory of map projections. *Bollettino di Geodesia e Scienze Affini*, 3(38):457–479.

- Crocetto, N., Gatti, M., and Russo, P. (2000). Simplified formulae for the BIQUE estimation of variance components in disjunctive observation groups. *J. Geod.*, 74(6):447–457.
- Demets, C., Gordon, R., Stein, S., and Argus, D. (1987). A revised estimate of Pacific-North America motion and implications for western North America plate boundary zone tectonics. *Geophys. Res. Lett.*, 14:911–914.
- Dermanis, A. and Grafarend, E. W. (1993). The finite element approach to the geodetic computation of two- and three-dimensional deformation parameters: A study of frame invariance and parameter estimability. In *Proceedings of the international conference on cartography*, Maracaibo (Venezuela).
- Dermanis, A. and Livieratos, E. (1983). Dilatation, shear, rotation and energy analysis of map projections. *Bollettino di Geodesia e Scienze Affini*, 1(42):53–68.
- Donnellan, A., Hager, B. H., King, R. W., and Herring, T. A. (1993). Geodetic measurement of deformation in the Ventura Basin region, Southern California. *J. Geophys. Res.*, 98(B12):21727–21739.
- Dragert, H. (1987). The fall (and rise) of central Vancouver Island: 1930-1985. *Can. J. Earth Sci.*, 24:689–697.
- Dragert, H., Chen, X., and Kouba, J. (1995). GPS monitoring of crustal strain in southwest British Columbia with the Western Canada Deformation Array. *Geomatica*, 49:301–313.
- Dragert, H., Hyndman, R. D., Rogers, G. C., and Wang, K. (1994). Current deformation and the width of the seismogenic zone of the northern Cascadia subduction thrust. *Journal of Geophys. Res.*, 99:653–668.
- Eisele, J. A. and Mason, R. M. (1970). *Applied Matrix and Tensor Analysis*. New York, Wiley-Interscience.
- Ernst, L. J. (1981). *A geometrically nonlinear finite element shell theory*. PhD thesis, Department of Mechanical Engineering, Technische Universiteit Delft.
- Grafarend, E. (1984). Variance-covariance-component estimation of Helmert type in the Gauß-Helmert model. *Z.f. V.*, 109:34–44.
- Grafarend, E., Kleusberg, A., and Schaffrin, B. (1980). An introduction to the variance-covariance-component estimation of Helmert type. *Z.V.F.*, 105:161–180.
- Grafarend, E. W. (1995). The optimal universal transverse mercator projection. *Manuscr. Geodaet.*, 20(6):421–468.
- Grafarend, E. W. (2004). Tensor algebra, linear algebra, multilinear algebra. Technical Report 2004.1, Institute of Geodesy, Universität Stuttgart, Germany.
- Grafarend, E. W. (2006). *Linear and nonlinear models:fixed effects, random effects, and mixed models*. Walter de Gruyter.
- Grafarend, E. W. and Engels, J. (1992). A global representation of ellipsoidal heights - geoidal undulations or topographic heights - in terms of orthonormal functions, part 1: "amplitude-modified" spherical harmonic functions. *Manuscr. Geodaet.*, 17(1):52–58.

- Grafarend, E. W. and Krumm, F. W. (2006). *Map Projections, Cartographic Information Systems*. Springer, Berlin.
- Grafarend, E. W. and Voosoghi, B. (2003). Intrinsic deformation analysis of the earth's surface based on displacement fields derived from space geodetic measurements. case studies: present-day deformation patterns of Europe and of the Mediterranean area (ITRF data sets). *J. Geod.*, 77(5-6):303–326.
- Gray, A. (1997). *Modern Differential Geometry of Curves and Surfaces with Mathematica*. CRC Press.
- Hartung, J. (1981). Nonnegative minimum biased invariant estimation in variance component models. *Ann. Statist.*, 9(2):278–292.
- Heck, B. (1999). Erfassung neotektonischer Deformationen im Bereich des Oberrheingrabens. In *SAPOS-Symposium: SAPOS 2000 - Ihr Standpunkt*, pages 106–110, Berlin.
- Heck, B., Illner, M., and Jäger, R. (1995). Deformationsanalyse zum Testnetz Karlsruhe auf der Basis der terrestrischen Nullmessung und aktueller GPS-Kampagnen. Geodätisches Institut der Universität Karlsruhe (Hrsg.): Festschrift für Heinz Draheim zum 80. Geburtstag, Eugen Kuntz zum 70. Geburtstag, Hermann Mälzer zum 70. Geburtstag.
- Helmert, F. (1907). *Die Ausgleichsrechnung nach der Methode der kleinsten Quadrate*. Reprinted with a note by H. Hohenner, Teubner, Leipzig, 2nd edition.
- Hojovec, V., Jokl, L., and Kascaronpar, J. (1981). Relation between the extreme angular and areal distortion in cartographic representation. *Stud. Geophys. Geod.*, 25(2):132–151.
- Hontani, H. and Deguchi, K. (1997). Multi-scale detection of characteristic figure structures using principal curvatures of image gray-level profile. In *SCALE-SPACE '97: Proceedings of the First International Conference on Scale-Space Theory in Computer Vision*, pages 315–318, London, UK. Springer-Verlag.
- Huang, J. and Véronneau, M. (2005). Determination of the Canadian Gravimetric Geoid 2005 (CGG05) using GRACE and Terrestrial Gravity Data. *AGU Fall Meeting Abstracts*.
- Hyndman, R. (1995). Great earthquakes in the Pacific Northwest. *Sci. Am.*, (273):50–57.
- Johnson, H. O., Agnew, D. C., and Wyatt, F. K. (1994). Present-day crustal deformation in Southern California. *J. Geophys. Res.*, 99(B12):2395123974.
- Kleusberg, A., Georgiadou, Y., and Dragert, H. (1988). Establishment of crustal deformation networks using GPS: A case study. *CISM Journal ACSGC*, 42:341–351.
- Koenderink, J. and Lisowski, A. (1992). Surface shape and curvature scales. *Image and vision comput.*, 10(8).
- LaFemina, P. C., Dixon, T. H., Malservisi, R., Arnadóttir, T., Sturkell, E., Sigmundsson, F., and Einarsson, P. (2005). Geodetic GPS measurements in south iceland : Strain accumulation and partitioning in a propagating ridge system. *J. Geophys. Res.*, 110(B11405).
- Malley, J. D. (1986). *Optimal Unbiased Estimation of Variance Components*. Springer Verlag.

- Massonnet, D., Holzer, T., and Vadon, H. (1997). Land subsidence caused by the East Mesa geothermal field, California, observed using SAR interferometry. *Geophys. Res. Lett.*, 24(8):901904.
- Mazzotti, S. T., James, S., Henton, J., and Adams, J. (2005). GPS crustal strain, postglacial rebound, and seismic hazard in eastern North America : The Saint Lawrence valley example. *J. Geophys. Res.*, 110(B11301).
- Meghan-Miller, M., Johnson, D. J., Rubin, C. M., Dragert, H., Wang, K., Qamar, A., and Goldfinger, C. (2001). GPS-determination of along-strike variation in Cascadia margin kinematics: Implications for relative plate motion, subduction zone coupling, and permanent deformation. *Tectonics*, 20(2):161–176.
- Mikhail, E. M. and Ackermann, F. (1976). *Observations and Least Squares*. Univ Pr of Amer, New York.
- Minster, C., Thorne, K., and Wheeler, J. (1973). *Gravitation*. W.H. Freeman, New York.
- Murray, M. H. and Lisowski, M. (2000). Strain accumulation along the Cascadia subduction zone. *Geophys Res. Lett.*, 27:3631–3634.
- Namson, J. and Davis, T. (1998). Structural transect of the Western Transverse Range, California: Implications for lithospheric kinematics and seismic risk evaluation. *Geology*, 16(8):675–679.
- Nikolaidis, R. (2002). *Observation of Geodetic and Seismic Deformation with the Global Positioning System*. PhD thesis, University of California, San Diego.
- Persson, C. G. (1981). On the estimation of variance components in linear models and related problems -with special reference to geodetic applications. Technical report, Royal Institute of Technology, Division of Geodesy, Stockholm.
- Pietraszkiewicz, W. (1977). Introduction to the non-linear theory of shells. Technical Report 10, Mitteilungen aus dem institut fuer Mechanik, Ruhr-Universität Bochum, Germany.
- Pietraszkiewicz, W. and Szwabowicz, M. (2007). Determination of the midsurface of a deformed shell from prescribed fields of surface strains and bendings. *Int. J. Solids Struct.*, 44(18-19):61636172.
- Politz, F. F., Wicks, C., and Thatcher, W. (2001). Mantle flow beneath a continental strike-slip fault; postseismic deformation after the 1999 Hector Mine earthquake. *Science*, 293(5536):1814 – 1818.
- Prakash, N. (1981). *Differential geometry*. Tata McGraw-Hill publishing Co. Ltd., New Delhi.
- Qu, Z. (1989). Estimation of variance and covariance components. *Bull. Geod.*, 63(2):139–148.
- Rao, C. and Kleffe, J. (1988). *Estimation of Variance Components and Applications*. North-Holland, Amsterdam.
- Rao, P. S. R. S. (1997). *Variance Components Estimation: Mixed Models, Methodologies and Applications*. Chapman and Hall, London.
- Rogers, G. C. (1988). An assessment of the megathrust earthquakes potential of the Cascadia subduction zone. *Canadian Journal of Earth Science*, 25:844–852.

- Sansour, C., Wriggers, P., and Sansour, J. (1997). Nonlinear dynamics of shells: Theory, finite element formulation, and integration schemes. *Nonlinear Dynamics*, 13(3):279–305(27).
- Satirapod, C., Wang, J., and Rizos, C. (2001). A new stochastic modelling procedure for precise static GPS positioning. *Z.f. V.*, 126(6):365–373.
- Savage, J. C., Lisowski, M., and Prescott, W. H. (1990). An apparent shear zone trending north-northwest across the Mojave Desert into Owens Valley, eastern California. *Geophys. Res. Lett.*, 17(12):2113–2116.
- Savage, J. C., Svarc, J. L., and Prescott, W. H. (2003). Near-field postseismic deformation associated with the 1992 Landers and 1999 Hector Mine, California, earthquakes. *J. Geophys. Res.*, 108(B9):2432.
- Shaffrin, B. (1983). *Varianz-Kovarianz-Komponenten-Schätzung bei der Ausgleichung heterogener Wiederholungsmessungen*. PhD thesis, Universität Bonn.
- Shen, Z. K., Jackson, D. D., and Ge, B. (1996). Crustal deformation across and beyond the Los Angeles basin from geodetic measurements. *J. Geophys. Res.*, 101(B12):27957–27980.
- Shen-Tu, B. M., Holt, W. E., and Haines, A. J. (1999). Deformation kinematics in the western United States determined from Quaternary fault slip rates and recent geodetic data. *J. Geophys. Res.*, 104(B12):28927–28955.
- Snay, R. A., Cline, W., Philipp, C. R., Jackson, D. D., Feng, Y., and Shen, Z. K. (1996). Crustal velocity field near the big bend of California’s San Andreas fault. *J. Geophys. Res.*, 101(B2):3173–3185.
- Stein, E. (1980). Variational functionals in the geometrical nonlinear theory of thin shells and finite-element-discretizations with applications to stability problems. In *Theory of Shells, Proceedings of the 3rd IUTAM Symp. on Shell Theory, Tbilisi 1978*, pages 509–535. North-Holland, Amsterdam-NewYork.
- Stein, R. S., King, G. C. P., and Lin, J. (1994). Stress triggering of the 1994 $m=6.7$ Northridge, California, earthquake by its predecessors. *Science*, 265(5177):1432 – 1435.
- Thomas, A. P. and Rockwell, T. K. (1996). A 300- to 500-year history of slip on the Imperial Fault near the U.S. -Mexico border: Missing slip at the Imperial fault bottleneck. *J. Geophys. Res.*, 101:5987–5997.
- Tissot, A. (1881). *Mmoire sur la representation des surfaces et les projections des cartes gographiques*. Gauthier-Villars, Paris.
- Vanicek, P., Thapa, K., and Schneider, D. (1981). The use of strain to identify incompatible observations and constraints in horizontal geodetic networks. *Manuscr. Geodaet.*, 6(3):257–281.
- Verdonck, D. (2004). Vertical crustal deformation in Cascadia from historical levelling. In *Denver Annual Meeting(Nov. 710, 2004)*.
- Verdonck, D. (2005). An inverse dislocation model of surface deformation in western Washington. *Tectonophysics*, 395(3-4):179–191.

- Visconti, A. (1992). *Introductory differential geometry for physicists*. World Scientific Publishing Co. Pte.Ltd., Singapore.
- Voosoghi, B. (2000). *Intrinsic deformation analysis of the Earth surface based on 3-dimensional displacement fields derived from space geodetic measurements*. PhD thesis, Institute of Geodesy, Universität Stuttgart, Germany.
- Wald, D., Heatson, T., and Hudnut, K. (1996). The slip history of the 1994 Northridge, California, earthquakes determined from strong ground motion, teleseismic, GPS, and leveling data. *Bull. Seismol. Soc. Am.*, 86(1B):S49–S70.
- Walpersdorf, A., Hatzfeld, D., Nankali, H., Tavakoli, F., Nilforoushan, F., Tatar, M., Vernant, P., Chry, J., and Masson, F. (2006). Difference in the GPS deformation pattern of North and Central Zagros (Iran). *Geophys. J. Int.*, 167(3):1077–1088.
- Wang, K., Dragert, H., and Melosh, H. J. (1987). Finite element study of uplift and strain across Vancouver Island. *Canadian Journal of Earth Science*, 31:1510–1522.
- Ward, S. T. (1998a). On the consistency of earthquake moment rates, geological fault data, and space geodetic strain: the United States. *Geophys. J. Int.*, 134(1):172–186.
- Ward, S. T. (1998b). On the consistency of earthquake moment release and space geodetic strain rates: Europe. *Geophys. J. Int.*, 135(3):1011–1018.
- Wdowinski, S., Sudman, Y., and Bock, Y. (2001). Geodetic detection of active faults in Southern California. *Geophys. Res. Lett.*, 28(12):2321–2324.
- Weinberg, S. (1972). *Gravitation and Cosmology: Principles and Applications of the General Theory of Relativity*. New York: Wiley.
- Xu, P. and Grafarend, E. W. (1996a). Probability distribution of eigenspectra and eigendirections of a two-dimensional, symmetric rank two random tensor. *J. Geod.*, 70(7):419–430.
- Xu, P. and Grafarend, E. W. (1996b). Statistics and geometry of the eigenspectra of three-dimensional second-rank symmetric random tensor. *Geophys. J. Int.*, 127(3):744–756.
- Xu, P., Shen, Y., Fukuda, Y., and Liu, Y. (2006). Variance component estimation in linear inverse ill-posed models. *J. Geod.*, 80(2):69–81.
- Xu, P., Yumei, L., Shen, Y., and Fukuda, Y. (2007). Estimability analysis of variance covariance components. *J. Geod.*, 81(2):593–602.

List of Abbreviations

FEM Finite Element Method

FFF First Fundamental Form

SFF Second Fundamental Form

TCC Tensor of Changes of Curvature

TCM Tensor of Changes of Metric

List of Symbols

Deterministic Aspects

M_l^2	left surface
M_r^2	right surface
$\{\Theta^1, \Theta^2\}$	curvilinear coordinates in left surface
$\{\theta^1, \theta^2\}$	curvilinear coordinates in right surface
\mathbf{X}	position vector on left surface
\mathbf{x}	position vector on right surface
$\{\mathbf{J}_1, \mathbf{J}_2, \mathbf{J}_3 \mid O\}$	orthogonal fixed frame in left surface
$\{\mathbf{j}_1, \mathbf{j}_2, \mathbf{j}_3 \mid o\}$	orthogonal fixed frame in right surface
\mathbf{A}_K	local base vectors on left surface
\mathbf{a}_k	local base vectors on right surface
$A_{\Lambda\Phi}$	left metric tensor
$a_{\lambda\phi}$	right metric tensor
\mathbf{A}_l	matrix form of left metric tensor
\mathbf{A}_r	matrix form of right metric tensor
$I(\Theta^1, \Theta^2)$	first fundamental form on left surface
$I(\theta^1, \theta^2)$	first fundamental form on right surface
\mathbf{J}_l	matrix form of left deformation gradient
\mathbf{J}_r	matrix form of right deformation gradient
$C_{\Lambda\Phi}$	Cauchy's deformation tensor or left Cauchy-Green deformation tensor
$c_{\lambda\phi}$	Green's deformation tensor or right Cauchy-Green deformation tensor
\mathbf{C}_l	matrix form of left Cauchy-Green deformation tensor
\mathbf{C}_r	matrix form of right Cauchy-Green deformation tensor
$E_{\Lambda\Phi}$	left strain tensor
$e_{\lambda\phi}$	right strain tensor
\mathbf{E}_l	matrix form of left strain tensor
\mathbf{E}_r	matrix form of right strain tensor
\mathbf{u}	displacement vector
\tilde{U}_K	covariant elements of displacement vector referred to left surface
\tilde{U}^K	contravariant elements of \mathbf{u} referred to left surface
\tilde{u}_k	covariant elements of \mathbf{u} referred to right surface
\tilde{u}^k	contravariant elements of \mathbf{u} referred to right surface

$\mathbf{u}_{,\Lambda}$	first-order partial derivatives of \mathbf{u} w.r.t left curvilinear coordinates
$\mathbf{u}_{,\lambda}$	first-order partial derivatives of \mathbf{u} w.r.t right curvilinear coordinates
$H(\Lambda, \Phi)$	ellipsoidal height (before deformation) as a function of left curvilinear coordinates
$h(\lambda, \phi)$	ellipsoidal height (after deformation) as a function of right curvilinear coordinates
$\Lambda_1, \Lambda_2, \Psi$	eigenspace components of left pair of matrices $\{\mathbf{E}_l, \mathbf{A}_l\}$
$\lambda_1, \lambda_2, \psi$	eigenspace components of right pair of matrices $\{\mathbf{E}_r, \mathbf{A}_r\}$
Δ	dilatation referred to left curvilinear coordinates
δ	dilatation referred to right curvilinear coordinates
Υ	maximum shear strain referred to left curvilinear coordinates
v	maximum shear strain referred to right curvilinear coordinates
Γ	rotation around the normal referred to left curvilinear coordinates
γ	rotation around the normal referred to right curvilinear coordinates
$R_{\Lambda\Phi}$	left rotation tensor
$r_{\lambda\phi}$	right rotation tensor
\mathbf{R}_l	matrix form of left rotation tensor
\mathbf{R}_r	matrix form of right rotation tensor
\mathbf{E}_l''	left strain tensor after simultaneous diagonalization (transformed strain tensor)
\mathbf{K}_l''	left TCC after simultaneous diagonalization (transformed TCC)
$\Lambda_1, \Lambda_2, \Theta$	eigenspace components of transformed strain tensor (via simultaneous diagonalization)
$\Lambda'_1, \Lambda'_2, \Theta'$	eigenspace components of transformed TCC (via simultaneous diagonalization)
$\Pi(\Theta^1, \Theta^2)$	second fundamental form on left surface
$\Pi(\theta^1, \theta^2)$	second fundamental form on right surface
$B_{\Lambda\Phi}$	left curvature tensor
$b_{\lambda\phi}$	right curvature tensor
\mathbf{B}_l	matrix form of left curvature tensor
\mathbf{B}_r	matrix form of right curvature tensor
$K_{\Lambda\Phi}$	left TCC
$k_{\lambda\phi}$	right TCC
\mathbf{K}_l	matrix form of left TCC
\mathbf{K}_r	matrix form of right TCC
\mathbf{w}	difference vector of unit normal vectors
\tilde{W}_K	covariant elements of \mathbf{w} referred to left surface
\tilde{W}^K	contravariant elements of \mathbf{w} referred to left surface
\tilde{w}_k	covariant elements of \mathbf{w} referred to right surface
\tilde{w}^k	contravariant elements of \mathbf{w} referred to right surface
$\Lambda'_1, \Lambda'_2, \Psi'$	eigenspace components of left pair of matrices $\{\mathbf{K}_l, \mathbf{A}_l\}$
$\lambda'_1, \lambda'_2, \psi'$	eigenspace components of right pair of matrices $\{\mathbf{K}_r, \mathbf{A}_r\}$
$\{\overset{\alpha}{\lambda}_\gamma\}$	Christoffel symbols of the second kind

Stochastic Aspects

vec	vector operator
vh	vector-half operator
$E\{\cdot\}$	expectation operator
$D\{\cdot\}$	dispersion operator
\mathbf{Q}	cofactor matrix
$\mathbf{1}$	denotes the $n \times 1$ summation vector consisting of ones
\otimes	denotes to Kronecker-Zehfuss product
n	number of epochs in tensor measurements
σ	array of covariance components $\sigma = [\sigma_1^2, \sigma_{12}, \dots, \sigma_{3n}^2]^T \in \mathbb{R}^{\frac{3n(3n+1)}{2}}$
\mathbf{y}_i''	vector-half form of i th transformed strain tensor ($\mathbf{E}_{l,i}''$)
\mathbf{Y}''	an array of vector-half forms $[\mathbf{y}_1'', \mathbf{y}_2'', \dots, \mathbf{y}_n'']$
$\mathbf{E}_{l,i}''$	i th sample of \mathbf{E}_l''
H	Helmert matrix

Appendix A

Partial Derivatives of Local Basis Vectors

We assume a surface \mathbb{M}^2 of class $C^m (m \geq 2)$ which is governed by vector $\mathbf{X} = \mathbf{X}(\Theta^1, \Theta^1)$. Then base vectors \mathbf{A}_K are functions of class C^1 and have continuous derivatives $\mathbf{A}_{K,\Lambda}$. The base vectors are linearly independent, then we can write

$$\mathbf{A}_{\Phi,\Lambda} = \left\{ \begin{array}{c} \Psi \\ \Phi\Lambda \end{array} \right\} \mathbf{A}_\Psi + \alpha_{\Phi\Lambda} \mathbf{A}_3 \quad (\text{A.1})$$

$$\mathbf{A}_{3,\Lambda} = \beta_\Lambda^\Psi \mathbf{A}_\Psi + \gamma_\Lambda \mathbf{A}_3 \quad (\text{A.2})$$

where coefficients $\left\{ \begin{array}{c} \Psi \\ \Phi\Lambda \end{array} \right\}$, γ_Λ , $\alpha_{\Phi\Lambda}$, β_Λ^Ψ are to be determined. Since \mathbf{A}_3 is of unit length, $\mathbf{A}_{3,\Lambda}$ is orthogonal to \mathbf{A}_3 . From Eq. (A.2) we clearly have

$$\langle \mathbf{A}_{3,\Lambda}, \mathbf{A}_3 \rangle = \beta_\Lambda^\Psi \langle \mathbf{A}_\Psi, \mathbf{A}_3 \rangle + \gamma_\Lambda \langle \mathbf{A}_3, \mathbf{A}_3 \rangle = 0$$

Hence $\gamma_\Lambda = 0$. It can be easily verified from Eq. (A.2) that

$$-B_{\Omega\Lambda} = \langle \mathbf{A}_\Omega, \mathbf{A}_{3,\Lambda} \rangle = \beta_\Lambda^\Psi \langle \mathbf{A}_\Omega, \mathbf{A}_\Psi \rangle \implies \beta_\Lambda^\Psi = -B_{\Omega\Lambda} A^{\Omega\Psi} \quad (\text{A.3})$$

Therefore, Eq. (A.2) will be obtained through

$$\mathbf{A}_{3,\Lambda} = -B_{\Omega\Lambda} A^{\Omega\Psi} \mathbf{A}_\Psi = -B_\Lambda^\Psi \mathbf{A}_\Psi \quad (\text{A.4})$$

Eq. (A.4) is called *Weingarten* equation which expresses that the first derivatives of the unit normal vector depend on both the first and second fundamental coefficients.

Consequently, taking a scalar product of both sides of the Eq. (A.1) with the vector \mathbf{A}_3 , we can derive coefficients $\alpha_{\Phi\Lambda}$. Namely

$$B_{\Phi\Lambda} = \langle \mathbf{A}_{\Phi,\Lambda}, \mathbf{A}_3 \rangle = \alpha_{\Phi\Lambda}$$

Hence, Eq. (A.1) will be denoted by

$$\mathbf{A}_{\Phi,\Lambda} = \left\{ \begin{array}{c} \Psi \\ \Phi\Lambda \end{array} \right\} \mathbf{A}_\Psi + B_{\Phi\Lambda} \mathbf{A}_3 \quad (\text{A.5})$$

Eq. (A.5) is called the *Gauss* equation. It remains to determine the coefficients $\left\{ \begin{smallmatrix} \Psi \\ \Phi\Lambda \end{smallmatrix} \right\}$. Hence, from Eq. (A.5) we have

$$\langle \mathbf{A}_{\Phi,\Lambda}, \mathbf{A}_{\Omega} \rangle = \left\{ \begin{smallmatrix} \Psi \\ \Phi\Lambda \end{smallmatrix} \right\} \langle \mathbf{A}_{\Psi}, \mathbf{A}_{\Omega} \rangle + B_{\Phi\Lambda} \langle \mathbf{A}_3, \mathbf{A}_{\Omega} \rangle \quad (\text{A.6})$$

Using the Eq. (A.6) and the fact that vectors \mathbf{A}_3 and \mathbf{A}_{Ω} are orthogonal to each other, we obtain

$$\left\{ \begin{smallmatrix} \Psi \\ \Phi\Lambda \end{smallmatrix} \right\} = A^{\Psi\Omega} \langle \mathbf{A}_{\Phi,\Lambda}, \mathbf{A}_{\Omega} \rangle = \frac{1}{2} A^{\Psi\Omega} (A_{\Omega\Lambda,\Phi} + A_{\Phi\Omega,\Lambda} - A_{\Phi\Lambda,\Omega}) \quad (\text{A.7})$$

The coefficients $\left\{ \begin{smallmatrix} \Psi \\ \Phi\Lambda \end{smallmatrix} \right\}$ are so-called *Christoffel* symbols of the second kind. We can see in Eq. (A.7) that the $\left\{ \begin{smallmatrix} \Psi \\ \Phi\Lambda \end{smallmatrix} \right\}$ depend only upon the FFF coefficients and their derivatives. It can be verified that $\left\{ \begin{smallmatrix} 1 \\ 21 \end{smallmatrix} \right\} = \left\{ \begin{smallmatrix} 1 \\ 12 \end{smallmatrix} \right\}$ and $\left\{ \begin{smallmatrix} 2 \\ 12 \end{smallmatrix} \right\} = \left\{ \begin{smallmatrix} 2 \\ 21 \end{smallmatrix} \right\}$, then $\left\{ \begin{smallmatrix} \Psi \\ \Phi\Lambda \end{smallmatrix} \right\} = \left\{ \begin{smallmatrix} \Psi \\ \Lambda\Phi \end{smallmatrix} \right\}$. The Christoffel symbols may be used for performing practical calculations in differential geometry (e.g., solving the geodesic equations).

Appendix B

2D Finite Element Method

A method for solving an equation by approximating continuous quantities as a set of quantities at discrete points (on the surface), often regularly spaced into a so-called grid or mesh. The optimal finite element meshes can be generated by Delaunay triangulation over the data set. The algorithm creates triangles by drawing lines between data points. The original points are connected in such a way that no triangle edges are intersected by other triangles. The result is a patchwork of triangular faces over the extent of the grid. This method is an exact interpolator. Each triangle defines a plane over the grid nodes lying within the triangle, with the tilt and elevation of the triangle determined by the three original data points defining the triangle. All grid nodes within a given triangle are defined by the triangular surface. Because the original data are used to define the triangles, the data are honored very closely.

In deformation analysis we use the Delaunay triangulation (in finite element scope) for approximating discrete displacement field. The sparse points(e.g., GPS stations) could be connected with a Delaunay triangulation within each triangle reconstructed by interpolation. Then in every triangle (element), we have linear interpolation of velocity field with respect to the local coordinates $\{L, B\}$. Let us assume that a triangle is constructed by three vertices (coordinates) : $\{L_K, B_K\}$ where $K \in \{1, 2, 3\}$. Then for every triangle we consider a centroid (as a reference point $\{L_0, B_0\}$), from which

$$\begin{aligned} U(L_1, B_1) &= U(L_0, B_0) + \frac{\partial U}{\partial L}(L_1 - L_0) + \frac{\partial U}{\partial B}(B_1 - B_0) \\ U(L_2, B_2) &= U(L_0, B_0) + \frac{\partial U}{\partial L}(L_2 - L_0) + \frac{\partial U}{\partial B}(B_2 - B_0) \\ U(L_3, B_3) &= U(L_0, B_0) + \frac{\partial U}{\partial L}(L_3 - L_0) + \frac{\partial U}{\partial B}(B_3 - B_0) \end{aligned} \tag{B.1}$$

then

$$X = \begin{bmatrix} U(L_0, B_0) \\ \frac{\partial U}{\partial L} \\ \frac{\partial U}{\partial B} \end{bmatrix} = \begin{bmatrix} 1 & L_1 - L_0 & B_1 - B_0 \\ 1 & L_2 - L_0 & B_2 - B_0 \\ 1 & L_3 - L_0 & B_3 - B_0 \end{bmatrix}^{-1} \begin{bmatrix} U(L_1, B_1) \\ U(L_2, B_2) \\ U(L_3, B_3) \end{bmatrix} \tag{B.2}$$

In the presence of errors in the measurements, we assume that \mathbf{Q}_U be a covariance matrix of measurements, then the covariance matrix of unknown coefficients can be obtained by

$$D\{X\} = \begin{bmatrix} 1 & L_1 - L_0 & B_1 - B_0 \\ 1 & L_2 - L_0 & B_2 - B_0 \\ 1 & L_3 - L_0 & B_3 - B_0 \end{bmatrix}^{-1} \mathbf{Q}_U \left(\begin{bmatrix} 1 & L_1 - L_0 & B_1 - B_0 \\ 1 & L_2 - L_0 & B_2 - B_0 \\ 1 & L_3 - L_0 & B_3 - B_0 \end{bmatrix}^{-1} \right)^T \quad (\text{B.3})$$

CURRICULUM VITAE

Address

Institute of Geodesy
Geschwister-Scholl-Str. 24D
D-70174 Stuttgart
Tel.: +49 (0) 711 / 685 8 - 3390
Fax: +49 (0) 711 / 685 8 - 3285
Email: moghtased@gis.uni-stuttgart.de

Personal Details

Date of birth: 21.09.1973
Place of birth: Zanzan, Iran
Marital status: Married

Education and Qualifications

1993-1996 Bachelor of Science (B.Sc.), in Engineering Surveying, in Isfahan University, Iran

1997-1999 Master of Science (M.Sc.), in Engineering Geodesy, in Tehran University, Iran

2003-2007 PhD candidate at the institute of Geodesy - Faculty of Aerospace Engineering and Geodesy of Stuttgart University, Germany